Reply by the authors to Referee #1's comments on
"Quantifying methane emissions from Queensland's coal seam gas producing Surat Basin using inventory data and an efficient regional Bayesian inversion" (#acp-2020-337)

Anonymous Referee #1 (RC1)

We are grateful to the Referee for taking the time to read our manuscript and making a number of valuable comments. In the following, we provide our responses to these comments (the Referee's comments are shown in blue). The locations of the changes made refer to those in the non-tracked version of the revised manuscript.

This paper employs a dataset of quasi-continuous measurements over an 18-month period from two monitoring stations in the middle of a region characterized by a mix of largely anthropogenic methane sources to optimize gridded methane emission inventory estimates. It aims to scale inventory emission estimates for individual grid boxes with a focus on the coal seam gas (CSG) industry. Given the current lack of atmospheric data to inform CSG methane emissions in Australia and elsewhere, this paper is a useful addition to the literature to help researchers improve their methods to quantify emissions from this source. The analysis is very detailed, the paper is well written, and the tables and figures are well presented.

Response: Thank you for your comments.

However, I have two major comments/questions that may be important for the bottom-line implications of the study:

1. The background methane mole fraction estimation (Supplementary S3) requires some more discussion. As Figure 3 shows, both monitoring stations are surrounded by known methane sources that are being quantified here. The monitoring stations do not measure the background air entering the spatial domain for which the emissions are being quantified here (hence background estimation). Filtering peaks during the early afternoon may exclude the largest point sources, but not necessarily the area sources that are clearly shown to exist in Figure 3. Does this estimation method create a high bias for the background levels, and in extension a low bias for the posterior emissions (especially from distributed sources like CSG wells)? Could this explain why all inverse setups produce smaller posterior total emissions than the prior despite the acknowledgment in the paper that the inventory may miss some sources (so the inventory itself may be underestimated)? Note that the opposite is true when looking only at the CSG sub-domain, which is situated largely between both monitoring stations (thus the sources in the CSG sub-domain affect estimated background values to a lesser extent), which appears to underscore this conundrum. It is also noteworthy that such underestimation may be masked also in the q-q plots comparing observed and modeled concentrations because a potentially underestimated prior and overestimated background would compensate each other.

Response: The reviewer has a valid point. Specification of background in a regional model is tricky. Ideally, this requires methane measurements at many locations around the perimeter of the study domain or modelling methane at much larger scale (preferably global), with all sources, sinks and chemical processes accounted for, which could then provide concentration boundary conditions needed for the regional modelling. Notwithstanding the difficulty in carrying out such a major computational task, there are modelling difficulties and uncertainties associated with emissions, representation of processes, model resolution issues etc. There could be other ways to calculate

background too, such as satellite data and model-data assimilation. Nevertheless, we believe that for the hourly-averaged, ground-level background concentrations needed in regional modelling study like ours, in-situ observations near the ground are still a better means to derive the background provided there are sufficient number of monitors sited at favourable locations than using a larger scale model.

In our case, we are limited by only two monitors (i.e. Ironbark and Burncluith) within a relatively large study domain. This reflects the operational and budget constraints of this project and is likely typical of many others. We calculated the hourly background using a methodology described in the Supplement S3 that utilised methane concentration measurements from the two monitors. It assumes that under vigorous atmospheric mixing conditions in the daytime, the measured concentrations within study domain represent methane levels both within and outside the domain boundaries, so that the measured concentrations can be taken to represent the background under such conditions. Figure 4 in the paper shows how the derived background defines the baseline for the methane measurements, which we have treated as the real background.

Because the background concentration is calculated from the measurements within the source region under study, there is a possibility that it represents an upper limit on the magnitude of the background, meaning that the real background is potentially lower than what we have used (as alluded to by the referee).

To examine the sensitivity of the emission inference to the background methane, we have done an additional inversion using an alternate background time series and this is described in detail in the new Supplement S5. The alternate background was constructed using our original background methane and marine baseline methane measurements from the Cape Grim Baseline Air Pollution Station (https://capegrim.csiro.au), located on the north-west tip of Tasmania (40.7ºS, 144.7ºE) (see the Supplement S5). The measurements from the Station were filtered for the marine baseline air (in southern mid latitudes), and the baseline methane thus represents concentration levels without the direct influence of the continental sources. As shown in Figure 1 below, the alternate background falls between the Surat Basin background as used in our study and the Cape Grim baseline (i.e. between the two bounds), and is, on average, lower than the previously used Surat background by 2.8 ppb. (On average, the Cape Grim marine baseline was 8.4 ppb lower than the original Surat background used).

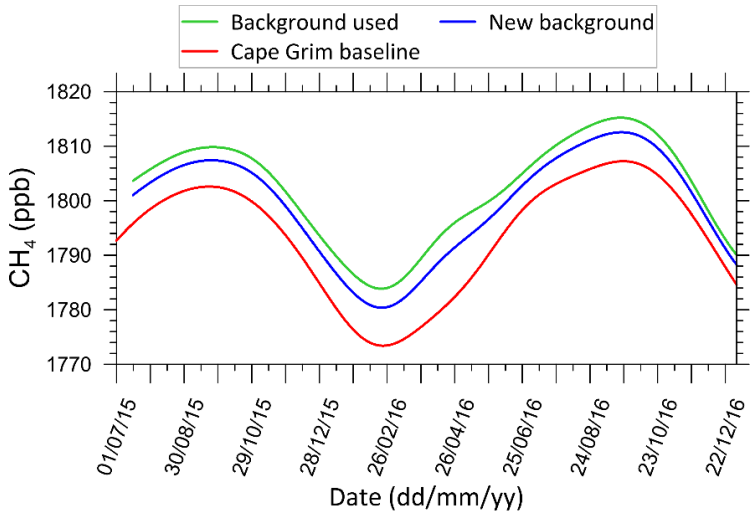

Figure 1. The average hourly background CH_4 concentration (ppbv) time series (green line) as used in the present paper. The hourly-averaged Cape Grim baseline methane is shown as a red line. Blue line is the alternate background.

The inversion results in Table 1 below show that compared to the inferred emissions obtained using the original background methane the alternate background gives total emissions that are 6.8% higher, while the increase is smaller at 3.9% in the CSG subdomain and larger at 8.5% in the non-CSG region. The overall increase is expected because the increase in the measured concentrations by 2.8 ppb as a result of the use of the alternate background needs to be accounted for by the inversion by enhancing the amount of inferred emissions.

We also find that the amount of increase in the inferred emissions with the alternate background is almost uniformly spread through the study domain relative to the total emission, and that there are no significant spatial distributional shifts in the inferred emissions with the two background choices. This means that if these enhanced emissions are used in a forward model simulation, they would lift the modelled concentrations throughout the region by a very similar amount (likely by 2.8 ppb).

Table 1: Inferred emissions ($\times 10^6$ kg yr^{-1}) obtained using the original methane background variation used in the paper (Case 3c in the paper, with the bottom-up inventory as a Gaussian prior with 3% uncertainty relative to the mean) and those obtained using the alternate methane background variation. The values in the parentheses are % change over the original inferred emissions.

Methane background	Total	CSG subdomain	Non-CSG subdomain
Original background (as used in the paper)	165.8	63.6	102.2
Alternate background	177.0 (+6.8%)	66.1 (+3.9%)	110.9 (+8.5%)

The above analysis demonstrates that there is an increase in the amount of inferred emissions with the alternate background and that this increase is smaller in the CSG subdomain relative to the original inferred emission.

Changes in manuscript: The new Supplement S5 given with full details of the above calculation, and the results are also summarised in Section 7.5 of the revised paper.

2. How are the higher-end modelled methane concentrations (but low occurrence, potentially not due to the infrequent emission, but rather due to their being point sources with fewer opportunities to be sampled) weighted against the overall average methane (but high occurrence) in the inversion model framework? Is this objectively weighted in the model (and if so, how), or is it a model design choice?

Response: In our inversions, the hourly-averaged methane measurements obtained during July 2015–December 2016 are combined in one Bayesian calculation to derive time invariant top-down emissions on an 11 × 11 source grid within the domain. Our inverse model framework is, in principle, able to discriminate between a source with a high emission rate but with infrequent impact at a sampling point and a source with a low emission rate but with frequent impact at the sampling point. This is because the concentration observations at the sampling point would reflect representative signals from these two types of sources, and this information when used in the source-receptor relationship would optimise the source emission rates accordingly such that they

best describe the concentration observations. In practice, however, the success in discriminating sources depends on the quality and quantity of available concentration observations, their spatial coverage, and on the number of source parameters that need to be quantified. This is where the specification of the prior plays a very important role because the information available (through concentration observations) may not be adequate to estimate the source parameters properly. This is demonstrated in our study.

Therefore, essentially, the only source weighting in our inverse framework is through the specification of the prior, and there is no other source weighting included/needed in the model apart from what is implicit through the Bayesian approach.

Changes in manuscript: We do not think that there is any change needed in the paper and hope that the above clarification is satisfactory.

Below is a list of detailed comments that may help clarify arguments and language, and correct potential errors.

Main article:

1. Ln 39: For balance, there's an ongoing discussion about the contrasting evidence (contemporary local measurements vs. ice-core 14C data) regarding the magnitude of the fraction of natural geologic seepage: https://www.elementascience.org/articles/10.1525/elementa.383/

Response: We have included two references to the bottom-up global estimates of natural geologic seepage.

Changes in manuscript:

We have modified the original wording to:

"However, a study using measurements of carbon-14 in methane recently showed that nearly all methane from fossil sources is anthropogenic, contrasting with the bottom-up estimates of significant natural geologic seepage (Etiope et al., 2019; Etiope and Schwietze, 2019), and that fossil fuel methane emissions may be underestimated by up to 40% (Hmiel et al., 2020)."

References:

Etiope, G, Ciotoli, G, Schwietzke, S and Schoell, M. 2019. Gridded maps of geological methane emissions and their isotopic signature. Earth Syst Sci Data 11: 1–22. DOI: 10.5194/essd-11-1-2019

Etiope, G. and Schwietzke, S., 2019. Global geological methane emissions: an update of top-down and bottom-up estimates. Elem Sci Anth, 7(1), p.47. DOI: http://doi.org/10.1525/elementa.383

2. Ln 58: "independent": I suggest "atmospherically based" instead since inverse estimates are by definition not completely independent of the prior/inventory.

Response: Point taken.

Changes in manuscript: Modification made.

3. Ln 71: Through this or any top-down approach? Would be valuable to mention if other top-down approaches have been used in Australia in the past.

Response: Point taken.

Changes in manuscript: We have added the following text:

"To our knowledge, this study is the first in Australia to quantify regional scale CH_4 emissions through a top-down approach employing transport modelling and concentration measurements, although studies at other spatial scales with broadly similar approaches have been reported, e.g. by Luhar et al. (2014) and Feitz et al. (2018) for single point sources at local scale and by Wang and Bentley (2002) at continental scale with Australian methane emissions divided into eight source regions."

References:

Luhar et al. (2014) and Feitz et al. (2018) already cited in the paper.

Wang, Y. P., and S. T. Bentley, S. T.: Development of a spatially explicit inventory of methane emissions from Australia and its verification using atmospheric concentration data, Atmospheric Environment, 36, 4965–4975, https://doi.org/10.1016/S1352-2310(02)00589-7, 2002.

4. Ln 158: Would re-phrase that the two operators account for 1.5% of CSG production activity in the region, not emissions (which would be difficult to establish with any accuracy).

Response: Point taken.

Changes in manuscript: The sentence is changed to "…but it was established that these two operators, with a total of 256 wells, only accounted for about 1.5% of the CSG activities that may be related to emissions."

5. Ln 189ff: Spatial resolution of 2.5º × 2.5º means (roughly) 250 x 250 km2. How, then, is it possible to apply it at 5 x 5 km2? Regarding the meaning of the 6 hour availability of met re-analyses, does it means that the temporal resolution is 6 hours?

Response: There is some misunderstanding here. The spatial resolution of 2.5º × 2.5º corresponds to the synoptic-scale fields of the horizontal wind components, temperature and moisture that are required as input boundary conditions for the outermost domain of TAPM. These fields given at 6-hourly intervals were sourced from the U.S. NCEP (National Centers for Environmental Prediction) reanalysis database. The TAPM model outputs hourly-averaged fields of meteorology and concentration at a specified horizontal resolution, which in the present application was 5 km × 5km.

Changes in manuscript: The above has been made clearer in the 2nd last paragraph of Section 4.1 of the revised paper (lines 212-220). Some more details of the model are given in the 2nd paragraph of this Section (lines 193-204).

6. Ln 291: I assume you're referring to the bottom-up emission inventory?

Response: Yes. Thanks for pointing that out. Correction made.

Changes in manuscript: As above.

7. Ln 666: Arguably Figure 14b cannot be used to support the trend in the CSG activity data. According to Ln 609, only 4% of the sub-domain emissions are due to CSG wells (and unclear whether the same processing facilities would emit more given more throughput), so any increase in well count may hardly be detectable by the monitoring stations. Thus, the insight here seems to be not that measurements aren't supporting the CSG increase, but that the existing monitoring setup is likely unable to detect.

Response: We have modified the text to improve clarity. A curve for the number of wells is also included in Figure 16 (Figure 19 in the revised paper).

Changes in manuscript: The paragraph revised as follows (lines 810-818):

"However, Figure 19 (*which is old Figure 16*) also shows that there is a downward trend in the amount of flared/vented gas. Considering, based on the bottom-up inventory in Section 3, that venting (from processing) is the biggest contributor (88%) followed by flaring (8%) (from both processing and production) to the total CSG methane emissions, it is plausible that despite the increase in the CSG development in the area the CSG-related methane emissions have not increased, and that they may have even gone down. The temporal variation of the inferred emissions in Figure 17b (*which is old Figure 14b*) for the CSG dominated area also does not indicate any consistent increase in emissions from 2015 to 2016. Thus, the 33% higher top-down emission estimate from the CSG area compared to the inventory estimate cannot be explained in terms of the growth in the CSG production from 2015 to 2016 and is possibly related to underestimated or missing emissions in the inventory. This also implies that the emissions from CSG may be more closely related to practices in the industry than to the amount of CSG produced."

Supplementary:

1. Ln 99: Emissions of methane due to incomplete combustion of CSG

Response: Change made.

Changes in manuscript: As above.

2. Ln 100ff: Why are methane GWPs used for methane emissions from incomplete combustion, fugitives, and coal extraction? It sounds like the underlying EFs are given in CO2e, which seems illogical.

Response: The calculation methods used to estimate methane emissions from CSG activities are consistent with the Australian National Greenhouse and Energy Reporting (NGER) program. We now attach the Katestone report "*Surat Basin Methane Inventory 2015 – Summary Report*" in the Supplement S6 of the paper, which explains in full detail how these emissions were calculated.

Changes in manuscript: As above.

Reply by the authors to Referee #2's comments on
"Quantifying methane emissions from Queensland's coal seam gas producing Surat Basin using inventory data and an efficient regional Bayesian inversion" (#acp-2020-337)

Anonymous Referee #2 (RC2)

We are grateful to the Referee for taking the time to read our manuscript and making a number of valuable comments. In the following, we provide a response to these comments (the Referee's comments are shown in blue). The locations of the changes made refer to those in the non-tracked version of the revised manuscript.

The manuscript presented by Luhar and co-workers presents an analysis of methane emissions from a region in Queensland, Australia, that contains a mix of different source processes of which coal seam gas production is the one mostly targeted and discussed in the study. Overall the study used valid and up to date methods. The manuscript is well structured and easy to follow. Quantifying uncertain methane emissions on the regional scale by in-situ observations and atmospheric inversion techniques is an important task supporting emission reductions and as such the study deserves publication. However, the authors should include some additional discussion of how their results may be used in the future by gas companies and/or authorities. I recommend the manuscript for publication after a number of minor issues (as listed below) are addressed/clarified by the authors.

Response: Thank you for your comments.

Changes in manuscript: Regarding some additional discussion of how the results may be used in the future by gas companies and/or authorities, we have included the following text at the end in Conclusions (lines 904-913):

"The methods developed in this study could be used to improve the monitoring and management of greenhouse gas and other air emissions from the onshore gas industry, including that in the Surat Basin. They provide independent information to industry and communities living in gas development regions on one of the main environmental impacts potentially arising from onshore gas developments. Improved quantification of methane emissions on the regional scale is an important step in emissions reductions from the onshore gas sector and possibly other industries. The present top-down method is particularly suited to distributed emissions with potentially unknown locations across a large geological gas reservoir and gas production infrastructure. If monitoring is deployed before gas exploration and production begins then a baseline would be established from which emissions from the industry might be detected. Ongoing top-down quantification, with monitoring stations located close to where emissions appear and with source-specific information from tracers could provide the information necessary to validate emissions from the gas industry to support greenhouse gas inventories."

Minor comments

Page 1, Line 2: Why is the term 'efficient' used in the title? What is efficient about this inversion approach? Further explain or omit from title.

Response: We have decided to omit the term 'efficient' from the title. The reason for its use was the application of the MCMC sampling method and the backward plume approach which make

computations very efficient. However, we admit that this is not the first time these approaches have been used in inverse modelling in general.

Changes in manuscript: 'efficient' omitted in the title.

P2, L58: Given the involved uncertainties in transport and inverse modeling, 'verification' may be a too strong term. Validation is often the preferred terminology.

Response: Point taken. 'Verification' replaced by 'validation'.

Changes in manuscript: As above.

Figure 1: A zoom into the study region including the location of the observational sites would be useful. This would also help to understand any orographic features of the domain.

Response: Point taken. We include an orographic map (Figure 1b) and also a Google Earth map showing the surface characteristics (Figure 1c) of the study domain. The Ironbark and Burncluith monitoring sites and the three biggest towns in the area are also shown.

Changes in manuscript: As above.

P4, L90: Were the inlets mounted on small towers or on rooftops? Please briefly mention even if described elsewhere.

Response: Inlets were mounted on masts.

Changes in manuscript: At line 103, we say '…with inlets placed on masts at a height of 10 m'.

Bottom-up inventory: Which emission processes were separated for the agricultural sources? Enteric fermentation, manure handling, etc.? The information in the supplement is very brief and I was not able to obtain the cited report by Katestone. Since this is the dominating emission source in the area, it would be good to give a few more details and also to briefly discuss the uncertainties in these estimates.

Response: We have now included the full Katestone report "*Surat Basin Methane Inventory 2015 – Summary Report*" in the Supplement S6 (it was prepared for us, i.e. CSIRO, by Katestone). It provides a comprehensive detail as to how the bottom-up inventory was constructed (largely by Lisa Smith of Katestone, who is a co-author on the present paper), including agricultural sources and uncertainties.

Changes in manuscript: As above.

P6, L145: What was the number of cattle in the feedlots? How do the emission factors per livestock unit compare between feedlots and free range? How were emissions from animal waste treated in the two cases?

Response: We now give the Katestone report in the Supplement S6 which provides this information.

Changes in manuscript: As above.

P7, L164f: What is this rough estimate based on? It seems to be rather large considering that the main source is cattle and per livestock emission factors are more certain than 50 %. Is the livestock number that uncertain?

Response: Yes, this was a very rough estimate, and we do not have any solid justification for it. Therefore, we have decided to delete it and modify the paragraph. The Katestone report that we now provide in the Supplement S6 provides more information about the bottom-up emissions.

Changes in manuscript: We have deleted this sentence.

Figure 3: What is the reasoning about showing these specific towns? Is there any larger population in the area?

Response: These are only given as reference points. We think that not all town locations are necessary. We now only present the locations of the three biggest towns, i.e. Dalby, Roma and Chinchilla (population 12700, 6850 and 6600, respectively), in the region.

Changes in manuscript: The above is stated in the Figure 1 and Figure 3 captions.

Section 4.3: The analysis in the supplement is quite useful. How does the wind rose comparison look for the filtered observation data. Does it improve? What is the mean bias for the filtered data? Next to wind speeds, mixing layer heights are critical when doing regional scale transport modeling and emission inversions. How is the mixing layer height treated in TAPM? Is there any way of comparing mixing layer heights for the target area and period or are their previous evaluations available for the model?

Response: In the Supplement S4, we now present a wind rose comparison for the filtered data (Figure S4) and provide the corresponding model performance statistics for meteorology (Table S1). With the filtering, the mean wind speed is predicted slightly worse, but the wind components are predicted better, which implies that there is an improvement in the estimation of wind direction with filtering.

The mean bias for the unfiltered and filtered data is now reported in Table S1.

Regarding mixing height, because TAPM is a fully prognostic, coupled meteorological and dispersion model, the predicted three-dimensional meteorological and turbulence fields are used directly by the dispersion component to predict concentrations. Therefore, there is no explicit use of mixing height as a parameter and the atmospheric mixing is taken care of by the predicted turbulence fields. Some of the model parameters that represent turbulence (and hence mixing) include friction velocity (mechanical turbulence) and surface heat flux (buoyancy-generated turbulence) have previously been evaluated in some of the studies cited (e.g. Luhar and Hurley, 2003; Hurley and Luhar, 2009; Luhar and Hurley, 2012; and Luhar et al., 2014)

In the Supplement S4, the link https://scholar.google.com.au/scholar?oi=bibs&hl=en&cites=13876071272134760358 to TAPM citation database provides additional references for TAPM application and evaluation.

Changes in manuscript: The Supplement S4 is modified with new Figure S4 and Table S1 included.

We provide some additional information about the meteorological component of the model in Section 4.1, which also details how turbulence is calculated (lines 193-204).

Modified paragraph:

"The model has previously been applied to a variety of flow, turbulence and dispersion problems at various scales, such as those reported by Luhar and Hurley (2003), Luhar et al. (2008), Hurley and Luhar (2009), Luhar and Hurley (2012), Luhar et al. (2014), Matthaios et al. (2017), and Luhar et al. (2020), which include model evaluation studies."

P12, L249f: Another important source of uncertainty is that of representativeness of the point measurement for the model grid cell (5x5 km). What are the observations compared to? Simulated values interpolated to the location of observation or grid cell containing the observation site? Are there any important sources in the closer vicinity of the sites (<10 km)?

Response: The hourly-averaged model predictions on the innermost grid domain were extracted at the lowest model level (10 m) at the grid point nearest to each of the monitoring sites for comparison with the observations. This is now stated in the text.

We agree that the model's representation of point measurements by grid-cell averaged values is another source of uncertainty, and it is now stated in the text.

The location of the two measurement stations was based on criteria given in Section 2, first paragraph, to "optimise the size and frequency of detection of methane emissions from the broader CSG source region without being unduly impacted by individual sources in the proximity of the measurement sites". (Other practical considerations are noted in the reference (Day et al., 2015), namely access, power, security, landowner assistance and possible future developments that would impact the site.) The sites were selected to avoid potential large, sustained methane sources within 10-20 km or even small sources within about a kilometre of the measurement inlet. Surveys of maps and by vehicle involving mobile methane monitoring of the area around the site identified few such sources. Small sources that were closer to the inlets (mainly Burncluith) were identified and their signals filtered from the data as described in Section 2. As a result, we expect that the hourly-averaged filtered data (Section 2) are as representative as possible of the atmospheric methane concentration across the 5 × 5 km grid cell containing the observation site, and can be directly compared to the model simulations.

Changes in manuscript: As above is summarise in the first para of Section 4.4, and it is mentioned that this is another possible source of differences between the observations and model predictions.

P13, L282: Not immediately clear what top 5 % refers to. How do these top 5 % simulated events compare to the observations? Are these also the highest observed concentrations?

Response: These are the highest 5% of the modelled concentrations, i.e. all the values above the 95th percentile. The idea here was to determine the dominant source types that contribute to highest modelled concentrations. A comparison of the modelled and observed concentrations has already been made in Figures 5 and 6, and it is clear that the highest concentrations are generally underestimated by the model at both sites (more so at Ironbark).

Changes in manuscript: The sentence is modified to '… the highest 5% of the modelled hourly-averaged methane concentrations (i.e. all the concentrations above the 95th percentile)'.

P19, L405ff: So if I understand this correctly, the source receptor relationship for a time t is constructed from output of c* at different times according to the value of tr at individual grid

points. First, I am wondering if this could be illustrated for an example case where one would show the field c* for a given time and then the reconstructed source receptor relationship for the same time. Second, it seems that there will remain some form of smearing out of the transport history in time. How much does this conflict with filtering data by time of day instead of using the complete data set. Also what was the rational of using hourly data in this case instead of working with longer aggregation times for which the effect should be smaller?

Response: The Referee is correct. We now explain it a bit better in the text and also present an illustrative example case in new Figure 7 that shows the field c^* for a given time and the reconstructed source receptor relationship for the same time (lines 440-461).

Occasionally, there may be some remains of smeared out transport history in time, but generally the intensity and the frequency of this is very small.

We do not think our method of reconstructing the hourly source-receptor relationship would conflict with the filtering of the data. This relationship is continuous with time, and its value at a particular hour would match the data points at that hour.

The rationale of using the hourly-averaged data rather (for which the effect of transport history would be smaller) was to maximise on the available information to constrain the inversions better. We could use longer averages, but that would have reduced the number of concentration data. Also, the wind direction variation inherent in the hourly data aids in better 'triangulation' of sources; the degree of this variation is progressively reduced as the averaging times are made longer. However, one could use longer aggregation times to see what difference that makes, but we have not attempted that. (Lines 493-497).

Changes in manuscript: As above, and new Figure 7 (a, b, c).

P20, L436: What about the sub-grid variability of these sources? Is it kept for the transport simulation and a factor for the larger grid boxes optimised or is the emission flux constant within the large grid boxes. What about the different source categories? Are they treated separately as was done for the forward simulation? Not clear from this description, later on it becomes clear that only total emissions are optimised.

Response: For the purposes of inferring emission rates using the inverse modelling, 11 × 11 source grid points are considered within the study domain. No sub-grid variability of these emission rates is considered. Given the limitation as to the type and amount of concentration observations we have for inversion, the inverse methodology used does not distinguish between different source categories. This is mainly because the concentration of methane alone was monitored and not tracers specific to methane source types. Therefore, there are no separate sources categories in the inferred emissions, unlike what was done for the forward simulation - only total emissions are optimised.

Changes in manuscript: This is clarified in the text (lines 500-507).

P21, L460: Does high probability mean small uncertainty of the posterior? That would be surprising when starting from larger prior uncertainties.

Response: The sentence is not correct and has been deleted.

Changes in manuscript: As above.

P21, L461: Above, it was speculated that the uncertainty of the bottom-up approach was 50 %. Here it is suggested that 0.5 % should be used in an inversion. That seems to be a contradiction. Please elaborate on the small sigma_p. Also, is sigma_p the uncertainty of the total emissions in the inversion grid or that of individual grid cells?

Response: We are not confident about the previously speculated uncertainty of 50% in the bottom-up approach, and have, therefore, deleted the sentence.

Following this comment and another comment below by the Referee, we revised Section 6 on inversion using the 'synthetic' concentration data considerably, with new model runs using an increased prior uncertainty (5% and 10%) and only considering times when the valid (or filtered) observations were actually available. This is more realistic, and the results now provide a better guidance to inversion using the real data.

sigma_p is the uncertainty (standard deviation) in the prior of the individual source and is specified as % relative to the prior mean value (there are 11 × 11 sources considered for the emission inference).

Changes in manuscript: Section 6 revised, with clarification in the text.

Section 6.1: Usually, one would add random or auto-correlated noise to the synthetic observations as a test up to which degree of uncertainty the inversion can obtain useful information. Was this not done here at all?

Response: We did not add any random or auto-correlated noise to the synthetic observations. But we performed new synthetic runs with the same 3.5 ppb uncertainty in the synthetic concentrations as that in the concentration observations for real inversions.

Changes in manuscript: The synthetic inversion Section 6 modified (lines 514-586) with modified and new plots (Figures 9–11).

Page 21, L464: How would the results change if only the synthetic observations were used at times when valid (filtered) observations were actually available? The latter was a considerably larger number of observations, so it is not clear how the results presented in this section can be propagated to the inversion with the more limited data set.

Response: This is a valid point. Following the Referee comment, we have revised the section on "Inversion using the 'synthetic' concentration data" considerably. We now present inversion results by using the synthetic observations only for times when the valid (or filtered) observations were actually available. The uncertainty in the synthetic concentrations is now taken to be the same (i.e. 3.5 ppb) as that in the concentration observations for real inversions. This now provides a better propagation of the results presented in this section to the next section on inversion using the real observations.

Changes in manuscript: The synthetic inversion Section 6 modified (lines 514-586) with modified and new plots (Figures 9–11).

Section 6.2: Next to the posterior emissions it would be good to show simulated time series (synthetic obs, prior, posterior) and some performance stats in order to get a feeling for the inversion performance. This is done later on with additional forward simulations, but it should also

be done with the concentrations directly obtained from the source receptor relationships and the coarse resolution emission setup as used in the inversion. Something to add to the supplement.

Response: Good point, but because this is a case of synthetic time series, we thought that rather than presenting the simulated time series it would be better to actually compare the inferred emissions with the bottom-up inventory emissions that were used to simulate the 'synthetic' concentrations (which in turn were used in the inversion). We have done this exercise and presented the results in Section 6.2 along with some performance statistics (i.e. linear least-squares fits and correlation coefficient). These new results also lead to a better linkage of this section on synthetic inversion to the next section on real inversion.

Changes in manuscript: As above (lines 535–586). New figures 10 and 11. Modified Figure 9.

P22, L491: I don't like the terminology "no prior". There is a prior! Why not call the case "uniform" prior, which would describe the used PDF.

Response: We now call it non-informative uniform prior in the text.

Changes in manuscript: As above.

Section 7.1.3: Again it would be useful to see simulation performance for the three uncertainty levels.

Response: Simulation performance for the three uncertainty levels is now given in new Table 1. We thought it was more appropriate to give it in Section 7.2 on validation than in Section 7.1.3.

Changes in manuscript: As above.

P23, L535: So if the best estimate results from using a Gaussian prior distribution, I wonder why an MCMC approach was used at all. Wouldn't it be much more efficient to use the analytical solution of the Bayesian theorem for Gaussian PDFs in this case?

Response: The Referee is correct with the Gaussian prior distribution. However, our idea was to formulate our inverse modelling tool with MCMC so that it is more generally applicable than just for the Gaussian PDFs—something that could be useful for future applications that we may consider.

Changes in manuscript: None.

Figure 11b: Why not show the relative posterior uncertainty? Couldn't this be more directly compared to sigma_p?

Response: Point taken. The plot has been replaced by the relative (%) posterior uncertainty and the corresponding text modified accordingly.

Changes in manuscript: As above.

P25, L551: Not clear which grid point this is referring to. Why is it relevant?

Response: This is grid point (11, 4), which corresponds to a relatively strong coal mine source in the bottom-up inventory (Figure 3d).

Changes in manuscript: Change made in the text.

P26, L577: Give information on which case 3 inversion is used here (sigma_p=?).

Response: This is Case 3 with 3% prior uncertainty relative to the mean.

Changes in manuscript: Change made in the text.

P28, L611ff: This argument could also be supported by comparing the emissions from the non-CSG sub-domain. Do they differ significantly between bottom-up and posterior? If so, what are the possible reasons?

Response: Emissions from the non-CSG subdomain are now compared (lines 739-742), new plot 17c and Table 2 and the discussion.

Changes in manuscript: As above.

P29, L629: Which sigma_p level?

Response: This is Case 3 with 3% prior uncertainty relative to the mean.

Changes in manuscript: Change made in the text.

Figure 14: Include uncertainties. That would allow judging of how well 3-monthly emissions are constraint and if there is a real difference with time. Other studies have shown seasonality in agricultural emissions. Could this be a possibility here as well? Or does it have to do with a seasonality in the source receptor relationships?

Response: Uncertainties are now included. There is also an additional plot (Figure 17c) for the 3-monthly variation of the inferred emissions for the non-CSG area (which is dominated by grazing cattle emissions as per the bottom-up inventory). In this plot, we also present a 3-monthly climatological average (1992 – current 2020) of rainfall at the Dalby airport, located next to the town of Dalby, within the study domain. There is a good correlation (r = 0.79) between the non-CSG area methane emissions and the rainfall, suggesting that the 3-monthly emission variation could possibly be explained in terms of the seasonality in agricultural and wetland emissions influenced by rainfall.

Another potential contributor to the temporal variability in the inferred emissions is the seasonality of the winds in the area which influence the source-receptor relationships. We have not explored this possibility here.

Changes in manuscript: As above. Figure 17c included. Lines 772-783.

Technical comments

P1,L21: 'identical TO' ...

Response: Correction made.

Figure 5: Add explanation of dashed line to figure caption.

Response: Point taken.

Changes in manuscript: We say '…and the dashed line is the 1:1 line (i.e. perfect agreement)'.

Figure 8: It seems to be more logical to start with the bottom-up emissions on the left (8a) and show the posterior on the right (8b).

Response: Point taken.

Changes in manuscript: The plots have been swapped and the figure caption and text modified accordingly.

Quantifying methane emissions from Queensland's coal seam gas producing Surat Basin using inventory data and a~~n efficient~~ regional Bayesian inversion

Ashok K. Luhar[1], David M. Etheridge[1], Zoë M. Loh[1], Julie Noonan[1], Darren Spencer[1], Lisa Smith[2], and Cindy Ong[3]

[1]CSIRO Oceans and Atmosphere, Aspendale, Victoria 3195, Australia
[2]Katestone Environmental Pty. Ltd., Milton, QLD 4064, Australia
[3]CSIRO Energy, Kensington, WA 6152, Australia

Correspondence to: Ashok Luhar (Ashok.Luhar@csiro.au)

Abstract. Methane (CH_4) is a potent greenhouse gas and a key precursor of tropospheric ozone, itself a powerful greenhouse gas and air pollutant. Methane emissions across Queensland's Surat Basin, Australia, result from a mix of activities, including the production and processing of coal seam gas (CSG). We measured methane concentrations over 1.5 years from two monitoring stations established 80 km apart on either side of the main CSG belt located within a study area of 350 × 350 km^2. Coupling bottom-up inventory and inverse modelling approaches, we quantify methane emissions from this area. The inventory suggests that the total emission is 173.2 × 10^6 kg CH_4 yr^{-1}, with grazing cattle contributing about half of that, cattle feedlots ~ 25%, and CSG Processing ~ 8%. Using the inventory emissions in a forward regional transport model indicates that the above sources are significant contributors to methane at both monitors. However, the model underestimates approximately the highest 15% of the observed methane concentrations, suggesting underestimated or missing emissions. An efficient regional Bayesian inverse model is developed, incorporating an hourly source-receptor relationship based on a backward-in-time configuration of the forward regional transport model, a posterior sampling scheme, and the hourly methane observations and a derived methane background. The inferred emissions obtained from one of the inverse model setups that uses a Gaussian prior whose averages are identical to the gridded bottom-up inventory emissions across the domain with an uncertainty of 3% of the averages best describes the observed methane. Having only two stations is not adequate at sampling distant source areas of the study domain, and this necessitates a small prior uncertainty. This inverse setup yields a total emission of 165.8 × 10^6 kg CH_4 yr^{-1}, slightly smaller than ~~that is very similar to~~ the ~~total~~ inventory total~~emission~~. However, in a subdomain covering the CSG development areas, the inferred emissions are 63.6 × 10^6 kg CH_4 yr^{-1}, ~33% larger than those from the inventory. We also infer seasonal variation of methane emissions within the full study domain, and CSG and non-CSG subdomains~~areas~~.

1 Introduction

Methane (CH_4) is a potent greenhouse gas~~It is the second most important anthropogenic greenhouse gas after CO_2 in terms of radiative forcing.~~ with a global warming potential 84 times greater than carbon dioxide (CO_2) over a 20-year period and 28 times greater over a 100-year period (IPCC, 2014). It is emitted by both anthropogenic activities (e.g. such as coal mining and the raising of cattle) and natural sources (e.g. wetlands). ~~Methane (CH_4) is a major greenhouse gas, with a global warming potential 28 times greater than carbon dioxide (CO_2) (over a 100-year period; IPCC, 2013).~~ In terms of anthropogenic radiative forcing, methane is the second most important greenhouse gas after CO_2. Globally averaged surface CH_4 concentrations have increased by almost 160% since pre-industrial times, from a level of 722 ppb to 1859 ppb in 2018 (WMO, 2018), and this increase has been largely due to changes in anthropogenic methane (e.g., IPCC, 2014~~3~~). Compared to CO_2, the atmospheric lifetime of methane is much~~relatively~~ shorter (~ 10 years), which means that ~~the~~ near-term warming of the climate ~~climate impact of methane~~ could diminish ~~rapidly~~ following mitigation actions that reduce methane~~its~~ emissions. Being chemically reactive, methane also plays an important role as a precursor to tropospheric ozone, itself a greenhouse gas and an air pollutant affecting human health and plant productivity. Thus, understanding and quantifying methane emissions at various scales is crucial to studying changes in atmospheric radiative forcing and air quality.

Globally, a top-down estimate over the period 2000-2017~~2~~ suggests that agriculture and waste contribute to about 5~~6~~7% of the total anthropogenic methane emissions, followed by fossil fuel production and use~~s~~ (gas, oil, coal mining and industry) at 3~~5~~2% (Saunois et al., 2020~~16~~). However, a study using measurements of carbon-14 in methane recently showed that nearly all methane from fossil sources is anthropogenic, contrasting with the bottom-up estimates of significant natural geologic seepage (Etiope et al., 2019; Etiope and Schwietze, 2019), and that fossil fuel methane emissions may be underestimated by up to 40% (Hmiel et al., 2020). ~~However, a study using measurements of carbon-14 in methane recently showed that nearly all methane from fossil sources is anthropogenic, and that fossil fuel methane emissions may be underestimated by up to 40% (Hmiel et al., 2020).~~ Significant CH_4 emissions from conventional and unconventional gas fields have been reported in the scientific literature (e.g., Brandt et al., 2014; Schneising et al., 2014; Alvarez et al., 2018).

In the Australian state of Queensland, since the mid-2000s there has been a rapid growth of the production of coal seam gas (CSG), which is virtually pure methane (Towler et al., 2016; DNRM, 2017). CSG, also known as coalbed methane, is classed as an unconventional natural gas, typically extracted from coal seams at depths of 200–1000 m. As of 2015-16, 96% of the gas production in Queensland was CSG, with most of it coming from the Surat Basin (78%, 21187 Mm^3) and the rest (18%, 4958 Mm^3) from the Bowen Basin (DNRM, 2017). With the sharp rise of CSG production, methane emissions from the Surat Basin are a focus~~, for example, through~~ of Australia's CSIRO Gas Industry Social and Environmental Research Alliance (GISERA) (https://gisera.csiro.au) research in Air Quality and Greenhouse Gas. The Surat Basin is predominantly rural, and methane sources other than CSG include agriculture and coal mining. CSG activities that lead to potential methane emissions include CSG wells, pumps, pipelines, vents, pneumatic controls, and produced water bodies (~~see~~ Day et al., 2013).

The objective of the present paper is to quantify methane emissions from a region of 350 × 350 km^2 of Queensland's side of the Surat Basin (Figure 1, covering the area 148° 17' 43.4"–151° 49' 30.5" E, 25° 3' 48.8"–28° 5' 3.7" S) that encompasses the main CSG production and processing areas using a ~~both bottom-up and~~ top-down technique~~s~~ assisted by a bottom-up emission inventory. The latter~~former~~ involves deriving emissions through a compilation of sources and activity data and application of emission factors. We conducted concurrent in-situ atmospheric monitoring of methane during July 2015 – December 2016 at two locations, namely Ironbark and Burncluith, 80 km from each other. The two stations were setup such that they were on either side of the broad present and projected CSG work area in the Surat Basin. The measured~~se~~ concentration~~s data~~ allow for an ~~independent~~ atmospherically based validation~~verification~~ of the bottom-up inventory ~~emissions~~ by using it~~the latter~~ in a forward mesoscale meteorological and transport model and comparing the predicted methane concentrations with the measurements at the two sites~~data~~.

The~~A~~ main~~greater~~ focus in the paper is on the formulation of an efficient top-down, or inverse, modelling methodology for regional scale (~ 100–1000 km), and its application to quantify CH_4 emissions in the Surat Basin. It combines a Bayesian inference approach, an hourly-averaged high-resolution backward-in-time construction of the forward mesoscale meteorological and transport model, and a posterior probability density function (PDF) sampling scheme. A method to correct for time-lag effects in the backward plume methodology is presented. The 1.5 years long hourly methane measurements from the two stations are combined in a Bayesian calculation to derive a top-down emission distribution. Methane background calculation and filtering methodologies are devised. Various Bayesian priors and their uncertainties, including the use of the bottom-up emissions to act as a prior, are tested. The inferred top-down CH_4 emissions are examined alongside the bottom-up inventory emissions for the whole study domain as well as ~~a~~ subdomains containing the CSG and non-CSG activities. We also compare the performance of the top-down emissions by comparing the modelled methane concentrations obtained using them in forward modelling with the observed concentrations. To our knowledge~~As far as we know~~, this study~~work~~ is the first in Australia to quantify regional scale CH_4 emissions through a top-down approach employing transport modelling and concentration measurements~~this top-down approach.~~, although studies at other spatial scales with broadly similar approaches have been reported, e.g. by Luhar et al. (2014) and Feitz et al. (2018) for single point sources at local scale and by Wang and Bentley (2002) at continental scale with Australian methane emissions divided into eight source regions.

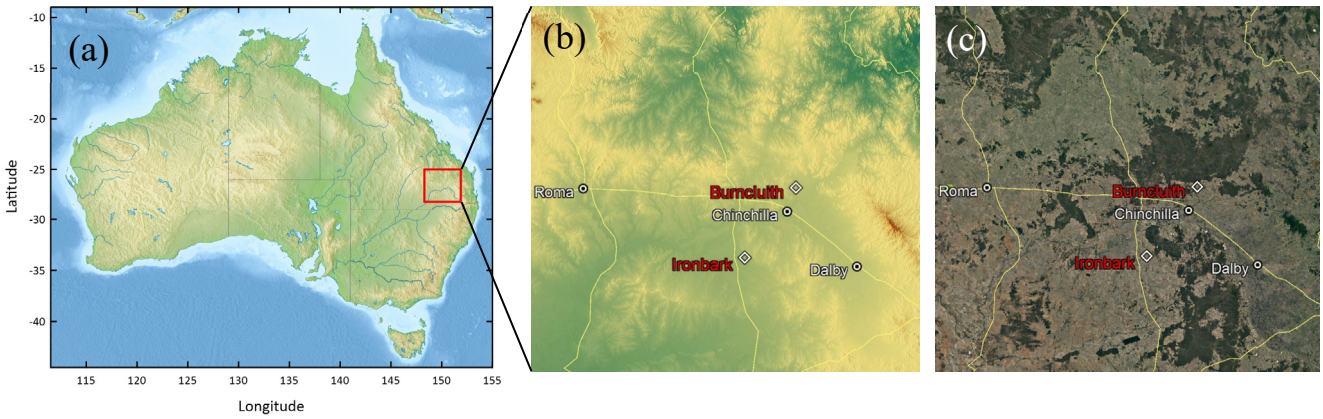

Figure 1. (a) Map of Australia, showing the 350 × 350 km² study domain (red square) of Queensland's part of the Surat Basin. The base relief map is from https://www.mapsland.com/oceania/australia/large-relief-map-of-australia (used under Creative Commons Attribution-ShareAlike 3.0 Licence); (b) orography of the study domain, with terrain elevation ranging approximately between 100 m (green) and 1140 m (red) above sea level; (c) a Google Earth map of the study domain showing the surface characteristics. The Ironbark and Burncluith monitoring sites, and the three biggest towns of Dalby, Roma and Chinchilla (population ~ 12700, 6850 and 6600, respectively) in the area are also shown.

2 Monitoring and data filtering

We set up two monitoring stations, ~~namely~~ Ironbark (150° 14' 37.6" E, 27° 8' 6.6" S; 226.806 km east, 6995.596 km north MGA (Map Grid Australia), Zone 56) and Burncluith (150° 42' 5.4" E, 26° 34' 2.4" S; 271.051 km east, 7059.430 km north MGA, Zone 56), located about 80 km apart on two sides of the main coal seam gas belt of the Surat Basin (Figure 1b). The selection of the site locations was largely~~partly~~ based on a meteorological and dispersion modelling study (Day et al., 2015; Etheridge et al., 2016) that suggested that with the prevailing winds from the north-east and south-west quadrants, long-term continuous monitoring of greenhouse gas concentrations at these two locations would optimise the size and frequency of detection of methane emissions from the broader CSG source region without being unduly impacted by individual sources in the proximity of the measurement sites. There were other practical considerations, ~~such as access, power, security, and land cover and topography.~~namely access, power, security, land owner assistance and possible future developments that would impact the site.

Continuous high frequency (~ 0.3 Hz) measurements of the concentrations of CH_4, CO_2 and water vapour (and also carbon monoxide (CO) at Burncluith) were made at the two sites for about three years with an overlapping period of 1.5 years (July 2015 to December 2016) using Picarro cavity ring down spectrometers (model G2301 at Ironbark, and G2401 at Burncluith) with inlets placed on masts at a height of 10 m. The installations are described by Etheridge et al. (2016). Measured concentrations (strictly speaking, mole fractions in dry air, also volumetric mixing ratios) from each site can be exactly intercompared due to identical calibrations and measurement methodologies. The additional CO measurements at Burncluith are useful in detecting combustion sources of CO_2 and CH_4. Measurement accuracy was better than ± 0.1 ppm for CO_2 and ±

1 ppb for CH_4 (Etheridge et al., 2014). Concurrent meteorological observations included winds measured at 5.8 m AGL (above ground level) at Ironbark and at 7.6 m AGL at Burncluith using sonic anemometers.

The Burncluith station was located on a private farm and there were 30–40 cattle in the paddocks next to it. Occasionally, under suitable meteorological conditions with the cattle upwind of the inlet, the emissions from the local cattle caused one or many sharp peaks in the observed methane signal, typical of a nearby point source. We developed a method which removes these sharp, transient peaks but does not alter the underlying signals from the numerous, region-wide feedlots, grazing cattle or other sources. This filtering method is described in the Supplement S1.1 and, for consistency, was also applied to the data from Ironbark, although local cattle are less in number and further away at this site.

Frequently, high methane concentrations at the two sites were observed at night under light wind stable conditions, particularly at Burncluith. ~~In spite of~~Despite being of much practical interest, however, light winds are difficult to represent in a mesoscale meteorological and transport model. The causes for that include inadequate physical understanding of light-wind processes, flow properties being very sensitive to local topography, and model resolution constraints (Luhar and Hurley, 2012). As a practical measure, we filtered out the nighttime sampling hours for light wind conditions, and this method is described in the Supplement S1.2.

Methane emissions due to biomass burning are not part of the bottom-up inventory that we consider in the present modelling due to their being sporadic and highly unpredictable. Enhanced levels of CH_4 and CO were detected at Burncluith in the course of forest fires in the northern sector of Burncluith and wood-heater operations from the property located in the proximity of the monitoring station. The observed CO was used to filter out these occasional biomass burning events from the measured concentration time series, ~~which is~~ an approach similar to that used by Jeong et al. (2012). Details of the CO filter are given in the Supplement S1.3.

The number of data hours after the filtering was 6432 for Ironbark and 4149 for Burncluith (cf. the original, valid number of data points of 10938 and 12660, respectively). Unless stated otherwise, the filtered CH_4 data were used for our analysis and modelling.

3 Bottom-up emission inventory

Activity data for the year 2015 were used to develop a bottom-up emission inventory for methane for the Surat Basin. The emission inventory covered a domain of 345 × 345 km^2 with a spatial resolution of 1 × 1 km^2. Standard methodologies were generally adopted with data from various State and Federal Government Departments (e.g. (National Pollutant Inventory (NPI), National Greenhouse and Energy Reporting (NGER), and National Resource Management (NRM)). The bottom-up inventory included the following fourteen emission sectors: (1) feedlots, (2) grazing cattle, (3) piggeries, (4) poultry farms, (5) power stations, (6) coal mining, (7) CSG processing, (8) CSG production, (9) domestic woodheating, (10) vehicular traffic, (11) land-fills, (12) sewage treatment plants, (13) river seepage, and (14) geological seepage. The first four can be grouped as agricultural

activities. The inventory excluded CH_4 emissions from burning of biomass, land clearing, termites, ground-water wells (that were registered), wetlands, or fuel consumption and any material handling related to mining activities. Additional details pertaining to the bottom-up inventory compilation are briefly given in the Supplement S2, with a full report given in the Supplement S5.

Figure 2 presents the bottom-up inventory emissions attributed to the various sectors in the Surat Basin, with the total emissions being 173.2×10^6 kg CH_4 yr^{-1}. Grazing cattle has the largest contribution, followed by cattle feedlots and CSG processing. We use this emission inventory for our study duration, July 2015–December 2016, with the assumption that any emission changes from the year 2015 to 2016 were insignificant. It is also assumed that all emissions are invariant with time. Although diurnal and seasonal variations for some emissions, viz. wood-heating, traffic, and power plant, are available in the raw data used in the inventory, contributions from these emissions are amongst the smallest and, therefore, we averaged these emissions over the full year for the purpose of computational efficiency in the modelling conducted here.

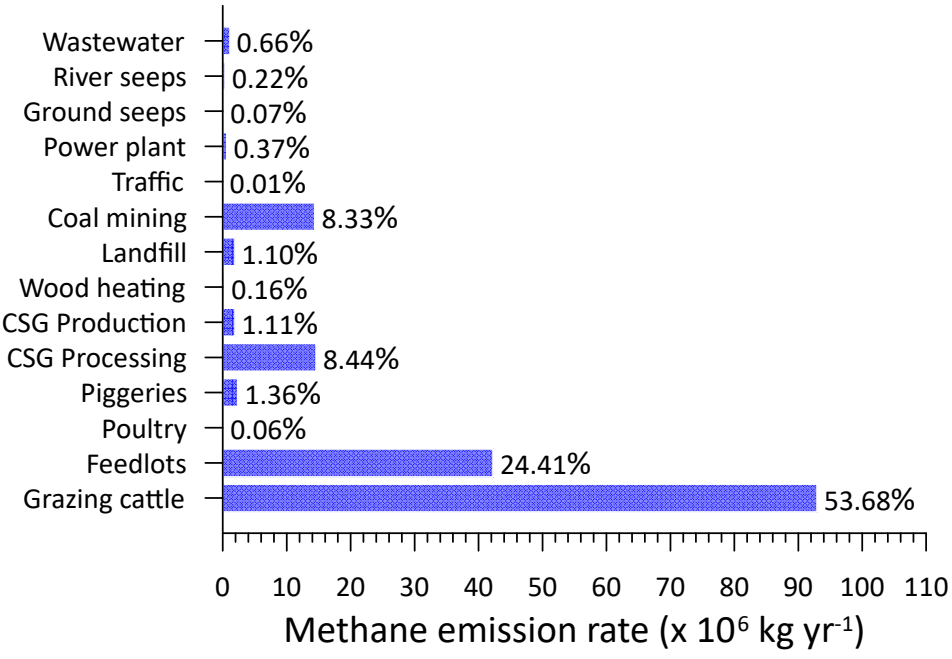

Figure 2. Bottom-up methane inventory emissions from the Surat Basin by sector/source; % of the total also shown. The total emission is 173.2×10^6 kg CH_4 yr^{-1}.

Figure 3a presents the distribution of inventory methane emissions (kg yr^{-1} $gridcell^{-1}$) at a grid resolution of 5×5 km^2 (69×69 grid points). There are localised sources as well as extensive, uniformly distributed source areas. The latter are emissions due to grazing cattle. These emissions are plotted in Figure 3b in which four different coloured areas are the so-called National

Resource Management (NRM) regions. In each of these regions the available total number of grazing cattle was distributed uniformly, with the total number of grazing cattle in the study area being 1,086,059. There were 235 cattle feedlots and Figure 3c shows the distribution of their emissions. These are localised, but distributed throughout the region, with some located between the two monitoring stations. Two mining source areas are also located between the two monitoring stations (Figure 3d).

The CSG emissions are shown in Figure 3e (processing) and Figure 3f (production). The CSG production emissions are from wellhead (separators, wellhead control equipment, maintenance and leaks), combustion (flaring, well head pumps, backup generators, and diesel used by vehicles) and pipeline emissions (high point vents on produced water pipelines and pipeline control equipment) (Day et al., 2013). The CSG processing sources consist of processing facility emissions (control equipment, compressor venting, and gas conditioning units), combustion emissions (flaring, plant compressors, backup generators, and diesel used by vehicles), and collection and storage of water produced. Emissions from some of the CSG sources are continuous while others are intermittent (however, the inventory assumes all CSG emissions are time invariant). There were 5 CSG operators with 13 processing facilities and 4628 wells within the study domain. The well numbers included CSG producing (~ 85%) as well as exploration/appraisal/capped wells. Because of insufficient information, methane emissions from two of the five operators are not part of the inventory, but it was established that these two operators, with a total of 256 wells, only accounted for about 1.5% of the CSG activities that may be related to emissions ~~related to CSG activities (which include a total of 256 wells)~~. The biggest contributor to the total CSG methane emissions was venting (88%) from processing, ~~followed by flaring (8%) from both processing and production.~~ Methane from p~~P~~roduced ~~-~~water is a component of both CSG production and processing is an important source (e.g. Iverach et al., 2015) and is calculated at ~~These emissions are calculated at~~ 1.63 × 10^6 kg ~~/~~yr^{-1} (~~~□~~10% of the total CSG emissions)~~.~~, Contribution from flaring was~~is~~ about 8%.

All major ~~sources considered in the~~ bottom-up emissions, namely from grazing cattle, feedlots, CSG processing and production, and coal mining, have potential ~~considerable~~ uncertainty, ~~which~~ arisinges from uncertainty in both the activity data and emission factors, for example their potential temporal variation and how up to date they are with respect to the study period considered. ~~It is difficult to calculate the uncertainty accurately, but a rough estimate of the upper bound of uncertainty in each of these source emissions is ± 50%.~~

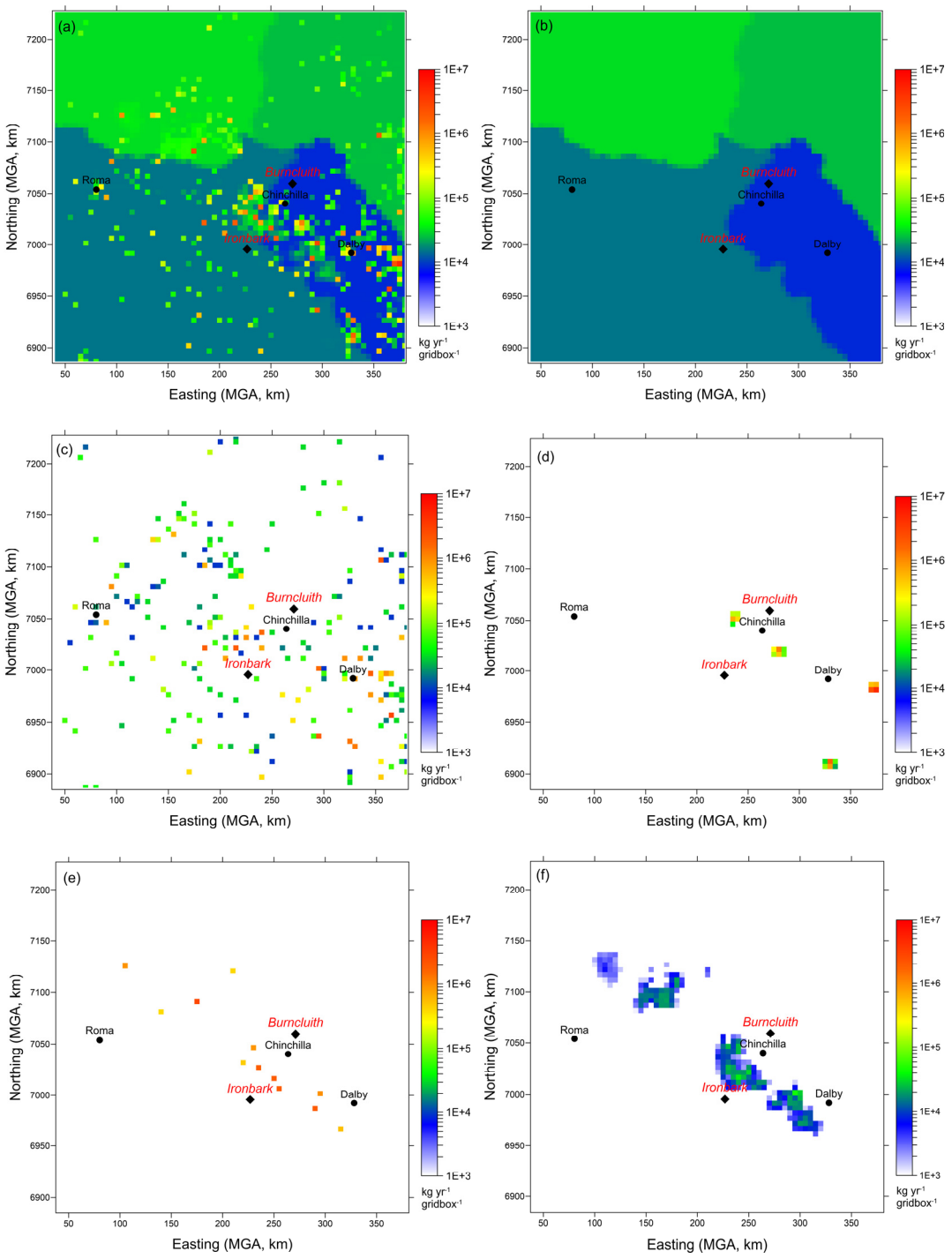

Figure 3. Bottom-up methane inventory emissions from the Surat Basin (kg CH_4 yr^{-1} $gridbox^{-1}$, the grid-box size is 5 × 5 km^2). Also shown are the Ironbark and Burncluith monitoring sites, and the three biggest towns. (a) All emissions, and those due to (b) grazing cattle, (c) cattle feedlots, (d) coal mining, (e) CSG processing, and (f) CSG production.

4 Modelling regional methane using the bottom-up inventory

We use the above inventory emissions in a (forward) regional meteorological and transport model and compare the modelled methane with the ambient measurements from the two sites.

4.1 Model and configuration~~setup~~

The prognostic, nestable, mesoscale model used is The Air Pollution Model (TAPM vn4.0.54) developed by CSIRO, which has coupled meteorological and dispersion components and which is designed for applications ranging in scale from local to regional (~ < 1000 km) (Hurley et al., 2005; Hurley, 2008 ~~Hurley and Luhar, 2009~~). ~~The dispersion module makes use of the predicted finer-scale meteorology and turbulence fields and comprises an Eulerian grid-based conservation equation for species concentration (Hurley et al., 2005).~~

The meteorological component of TAPM predicts the local-scale flow against a background of larger-scale meteorology provided by the input synoptic-scale analyses (or forecasts). It solves momentum equations for horizontal wind components; the incompressible continuity equation for the vertical velocity in a terrain-following coordinate system; and scalar equations for potential virtual temperature, specific humidity of water vapour, cloud water/ice, rainwater and snow. Explicit cloud microphysical processes are included. Pressure is determined from the sum of hydrostatic and optional non-hydrostatic components, and a Poisson equation is solved for the non-hydrostatic component (not used here). Turbulence closure in the mean prognostic equations uses a gradient diffusion approach with non-local or counter-gradient corrections, which depends on eddy diffusivity (K) and gradients of mean variables and a mass-flux approach. The eddy diffusivity K is determined using prognostic equations for the turbulent kinetic energy (E) and its dissipation rate (ε). A vegetative canopy, soil scheme, and urban scheme are used at the surface, while radiative fluxes, both at the surface and at upper levels, are also included. Surface boundary conditions for the turbulent fluxes are determined using the Monin-Obukhov similarity theory and parameterisations for stomatal resistance.

The dispersion module makes use of the predicted finer-scale meteorology and turbulence fields from the meteorological component, and comprises a default~~n~~ Eulerian grid-based conservation equation for species concentration (Hurley et al., 2005). ~~TAPM uses the synoptic-scale meteorological reanalyses given for horizontal winds, moisture and temperature and available from the U.S. NCEP (National Centers for Environmental Prediction) every 6 hours at a spatial resolution of 2.5° × 2.5° on several levels.~~

The model has previously been applied to a variety of flow, turbulence and dispersion problems at various scales, such as those reported by Luhar and Hurley (2003), Luhar et al. (2008), Hurley and Luhar (2009), Luhar and Hurley (2012),~~,~~ ~~and~~ Luhar et al. (2014),~~,~~ Matthaios et al. (2017), and Luhar et al. (2020), which include model evaluation studies.~~.~~

TAPM can be used in a one-way nestable mode to improve efficiency and resolution. The global databases input to the model include land use, terrain height, leaf-area index, synoptic-scale meteorological reanalyses, and sea-surface temperature (SST).

We applied TAPM for the duration 1 July 2015 – 31 December 2016 by using two nested domains for both meteorology and dispersion: 370 × 370 km^2 with grid resolution 5 × 5 km^2 and 1110 × 1110 km^2 with grid resolution 15 × 15 km^2. Both domains had 75 × 75 grid points and were centred on (150°4.5' E, 26°35' S), which is equivalent to 208.657 km east and 7056.383 km north in MGA. There were 25 vertical levels, of which the lowest four were 10 m, 25 m, 50 m and 100 m AGL. The input synoptic-scale fields of the horizontal wind components, temperature and moisture required as boundary conditions for the outermost model domain were sourced from the U.S. NCEP (National Centers for Environmental Prediction) reanalysis database given at a resolution of 2.5° latitude × 2.5° longitude at 6-hourly intervals (Kalnay et al., 1996; https://psl.noaa.gov/data/gridded/data.ncep.reanalysis.html). The model outputs hourly-averaged fields of meteorology and concentration.

The bottom-up inventory emissions lie within the inner model domain. In this model setup, each inventory emission grid cell (at 5 × 5 km^2) was considered as an area source, apart from the emissions from the power stations which were taken as point sources together with specification of their stack heights and plume-rise parameters. For computational efficiency, rather than considering all 14 emission categories plotted in Figure 2 as separate sources, we aggregated them into 9 sectors with each sector taken as a tracer source: Grazing cattle (Source 1); Feedlot, Piggeries and Poultry (Source 2); CSG Processing (Source 3); CSG Production (Source 4); Mining (Source 5); River seeps (Source 6); Domestic wood heating, Wastewater treatment and Motor vehicles (Source 7); Ground seeps and Landfill (Source 8); and Power stations (Source 9). The relative emissions (%) of the above nine Sources are 53.8, 25.8, 8.4, 1.1, 8.3, 0.21, 0.82, 1.2 and 0.37%.

4.2 Estimation of~~ed~~ background methane concentration

Since the simulated methane does not include the background levels that are representative of methane emissions located outside the bottom-up inventory, we devised a method for estimating hourly varying background CH_4 for each site involving concentrations under high atmospheric mixing conditions and the hourly standard deviation of concentration (see details in the Supplement S3. The estimated background concentration can be either added to the simulated methane or subtracted from the observed methane.

The estimated background methane concentration time series for Ironbark and Burncluith look~~s~~ very similar ~~(not shown)~~, and in Figure 4 we present~~s~~ ~~(green line)~~ the average (green line) of the~~estimated time series of the~~ two background time series. The plot ~~CH_4 concentration for Ironbark,~~ show~~sing~~ a marked seasonal variation in the background methane with a peak in September (early spring) and a minimum in February (late summer). To view the background variation with respect to the measured methane signal, we also present in Figure 4 as dot points the unfiltered hourly mean observations (clipped at 2100 ppb) at Ironbark. ~~The estimated background concentration time series for Burncluith looks very similar (not shown).~~ The uncertainty in the background CH_4 is 3.6 ppb and 3.3 ppb for Ironbark and Burncluith, respectively. The difference between the estimated background at Ironbark and that at Burncluith (purple line in Figure 4) is small and within ± 5 ppb. Any difference between the two backgrounds could be due to different sites in the study area getting impacted by different out-of-domain

emissions depending on the transport meteorology. On average, the background concentration at Ironbark is greater by 1 ppb, and the standard deviation of the difference is 1.4 ppb. ~~We take t~~The average of the two background time series is taken to represent the regional hourly background CH_4 concentration, with an average uncertainty of 3.5 ppb.

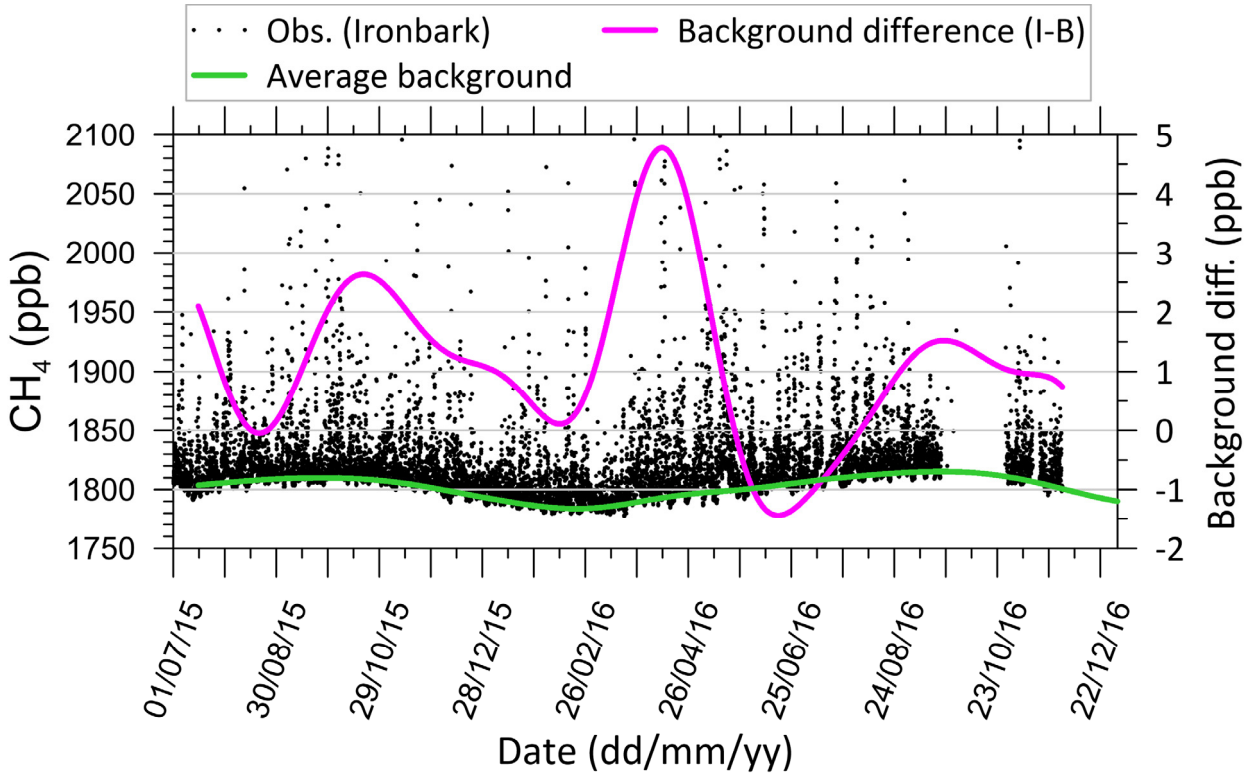

Figure 4. Estimated average hourly-averaged background CH_4 concentration time series ~~at Ironbark~~ (green line), and the difference between the estimated backgrounds between Ironbark and Burncluith (purple line). The data points are the hourly mean measurements at Ironbark without any filtering (clipped at 2100 ppb to make the background concentration variation stand out better).

4.3 Model performance for meteorology

Accurate modelling of the flow field over our region of interest is important as it controls the atmospheric plume transport and dispersion which in turn influences the accuracy of prediction of CH_4, and conversely the accuracy of inferred emissions. The hourly-averaged predicted winds extracted from the model output for the inner nest at the lowest model vertical level~~a height (of~~ 10 m) at the grid point nearest to each of the two monitoring stations were compared with the observations from the two

~~monitoring~~ stations for the duration of the simulation, with the missing data hours not considered. The details of the model performance for meteorology is given in the Supplement S4. At both sites, the measured winds were most frequent from the north-east sector, with those at Burncluith being generally weaker in strength than those at Ironbark. As judged from the correlation coefficient (r) and index of agreement (IOA) values, the performance of TAPM for wind speed and wind direction was comparable to that obtained in other TAPM modelling studies.

4.4 Modelled methane compared to observations

The monitoring sites were selected to avoid potential large, sustained methane sources within 10-20 km or even small sources within about a kilometre of the measurement inlet. Small sources that were closer to the inlets (mainly Burncluith) were identified and their signals filtered from the data as described in Section 2. As a result, we expect that the hourly-averaged filtered data are as representative as possible of the atmospheric methane concentration across the 5 × 5 km model grid cell containing the observation site, and can be directly compared to the model simulations.

The hourly-averaged modelled methane concentrations on the innermost grid domain were extracted at the lowest model level at the grid point nearest to each of the monitoring sites for comparison with the observations. The hourly-averaged ~~methane~~ concentrations simulated for individual 9 source categories were aggregated and added to the estimated background concentration to compare with the observed, filtered CH_4 concentrations.

The scatter plots in Figure 5 comparing the modelled and observed CH_4 at the two sites display a substantial degree of scatter, which is not unusual for atmospheric transport and diffusion models driven by predicted meteorology and using hourly-averaged concentrations paired in both time and space (e.g. Luhar et al., 2008). While the correlation coefficient values of 0.57 and 0.74 for Ironbark and Burncluith, respectively, imply a reasonable model prediction (see Table 1 for additional model performance statistics for the inventory emissions), it is clear that the modelled levels are generally lower than the observations, particularly the higher-end concentrations at Ironbark.

There could be various reasons for the differences between the modelled and observed methane, including uncertainty associated with the bottom-up emission inventory, its potential temporal variation, sources missing from the emission inventory, potential changes to the 2015 bottom-up inventory used here in the year 2016 (see Section 7.4), and the general modelling uncertainty, including that related to ~~in the model's ability~~ representing point measurements by grid-cell averaged model values~~to fully represent the atmospheric processes within the study domain~~.

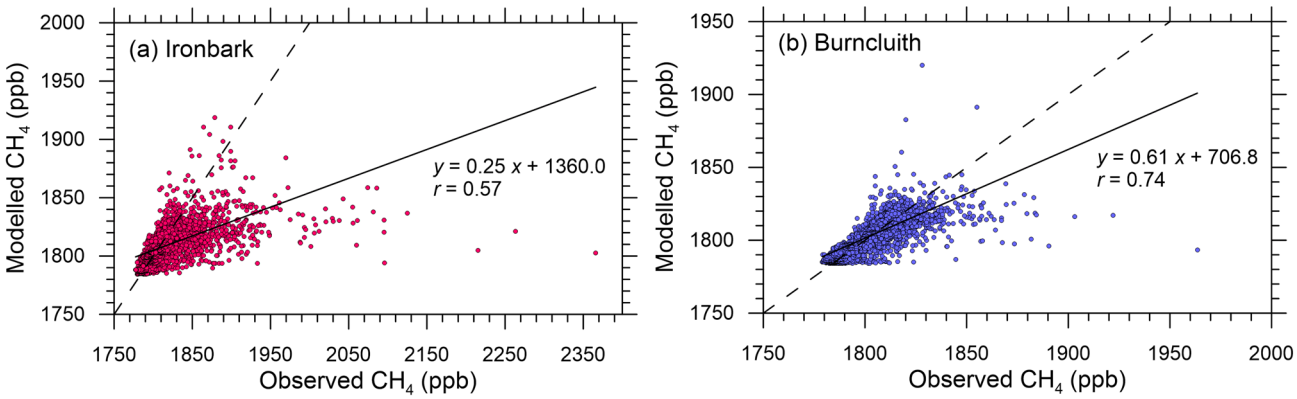

Figure 5. Hourly-averaged observed methane plotted against the simulated methane for the two monitoring stations. The solid line is the least-squares fit, and the dashed line is the 1:1 line (i.e. perfect agreement).

The comparison in Figure 5 involving hourly methane paired in time and space enables a simple, yet stringent, validation check of a transport model, especially one that is driven by turbulent flow fields predicted by a prognostic meteorological model instead of observations. A complementary but less stringent approach in validating air quality models is the quantile-quantile (q-q) plot, which is a graphical technique for testing "goodness of fit" between two distributions. In such a plot, typically, sorted modelled concentrations are plotted against sorted observed values (i.e. unpaired in time) at a monitoring location (e.g., Venkatram et al., 2001; Luhar and Hurley, 2003; http://www.itl.nist.gov/div898/handbook/eda/section3/qqplot.htm). If the two sets come from a population with the same distribution, the data points should fall approximately along the 1:1 line. The principal advantage of a q-q plot is that a "good fit" is easy to recognize, and various distributional aspects, such as shape, tail behaviour and outliers, can be simultaneously examined.

In the q-q plot in Figure 6 for Ironbark, the observed CH_4 distribution is modelled well for measurements < 1820 ppb, but for higher observed concentrations, which account for approximately 25% of the sample size, the modelled values are smaller For Burncluith, the q-q plot shows a substantially better model performance, with the model underestimation of higher-end (> 1820 ppb) methane observations, which is approximately 10% of the sample size, much reduced compared to Ironbark. Overall, TAPM is largely predicting the observed CH_4 distribution correctly, except for a relatively few higher-end concentrations.

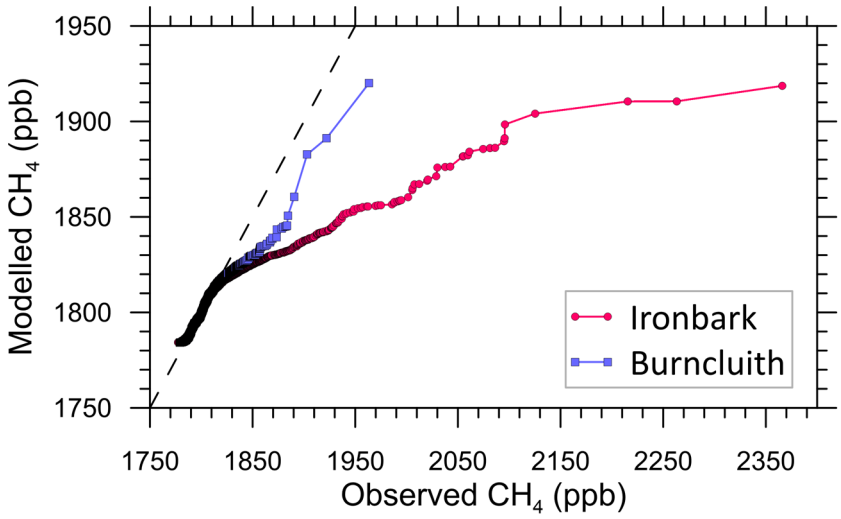

Figure 6. Q-q plot showing the sorted hourly-averaged observed CH_4 concentrations versus the sorted modelled ones at Ironbark and Burncluith. The line of perfect agreement (dashed line) is also shown.

325

4.5 Contribution to the modelled methane by various source categories

The top four source categories based on their contribution to the modelled CH_4 averaged over the full study period at Ironbark were Source 1 (45%, Grazing cattle), Source 2 (25%, Feedlot, Piggeries and Poultry), Source 3 (19%, CSG Processing), and Source 5 (5.5%, Mining). These were the same at Burncluith, but with their respective contributions being 69%, 17%, 6.4% and 4.1%. The CSG Production (Source 4) contributions are 2.2% and 0.73%, respectively, at the two sites.

In contrast, the largest four contributors to the highest~~top~~ 5% of the modelled hourly-averaged~~simulated~~ methane concentrations (i.e. all the concentrations above the 95th percentile) at Ironbark turn out to be Source 3 (35%), Source 2 (27%), Source 1 (25%) and Source 5 (7%). These at Burncluith are Source 1 (28%), Source 2 (25%), Source 3 (22%) and Source 5 (13%). The CSG Production (Source 4) contributes 3.8% and 2.5%, respectively, at the two sites. The Source 2 grouping is dominated by Feedlots.

The CSG Processing (Source 3) emissions are localised near the two sites which result in methane spikes under favourable winds and thus contribute more to the higher-end modelled methane than to the overall average methane. In contrast, the simulation average methane is dominated by Sources 1 and 2 because concentration enhancements due to these sources occur under most wind conditions as a result of their very wide distribution across the region.

5 Regional top-down, or inverse, modelling for emission estimation

Given that the bottom~~top~~-up~~down~~ emission inventory underestimates the observed methane in the Surat Basin, then one may ask what is the quantity and distribution of methane emissions that is implied by the methane concentration measurements at Ironbark and Burncluith? This is addressed by the inverse modelling approach for regional emissions formulated and applied below.

5.1 Bayesian inverse modelling approach

Our inverse model uses a Bayesian inference approach that incorporates, a source-receptor relationship, concentration measurements, and prior information on source parameters (i.e. source information obtained independently of the measurements) (Rao, 2007; Singh et al., 2015). The approach updates the source prior as concentration measurements are considered, and accounts for both model and observational uncertainties.

Several applications using the Bayesian approach have previously been conducted for methane source estimation, including those at local scale (Yee and Flesch, 2010; Luhar et al., 2014; Feitz et al., 2018) and regional scale (Jeong et al., 2012; Miller et al., 2014; Henne et al., 2016; Cui et al., 2017).

The approach hinges on Bayes' theorem (Jaynes, 2003):

$$p(\mathbf{q}|\mathbf{c}) = \frac{p(\mathbf{c}|\mathbf{q}) \, . \, p(\mathbf{q})}{p(\mathbf{c})}, \tag{1}$$

where the *prior* PDF $p(\mathbf{q})$ reflects our knowledge of the source parameter vector $\mathbf{q}$ prior to receiving the concentration observations $\mathbf{c}$; $p(\mathbf{c}|\mathbf{q})$ is the *likelihood* function which is the probability of experiencing $\mathbf{c}$ for a given $\mathbf{q}$ and is typically obtained using a model-derived source-receptor linkage; the *posterior* $p(\mathbf{q}|\mathbf{c})$ relates to the update of $p(\mathbf{q})$ by its modulation by $p(\mathbf{c}|\mathbf{q})$ which contains the new information brought in by the concentration measurements $\mathbf{c}$; and $p(\mathbf{c})$ [$=\int p(\mathbf{c}|\mathbf{q})p(\mathbf{q})d\mathbf{q}$] is the *evidence* and is basically a normalisation constant in the present application (Yee and Flesch, 2010). The likelihood function, also termed the source-receptor relationship, is derived using a transport and dispersion model.

It is assumed that the number of sources (N_s) and their locations $\left(\mathbf{x}_{s,1}, \ldots, \mathbf{x}_{s,j}, \ldots, \mathbf{x}_{s,N_S}\right)$ where $\mathbf{x}_{s,1} \equiv \left(x_{s,1}, y_{s,1}, z_{s,1}\right)$ are given *a priori* and the source emissions are non-zero. The emission rates of these sources are to be estimated, and these are represented by $\mathbf{q} \equiv \left(q_1, \ldots, q_j, \ldots, q_{N_S}\right)$ with a total of N_S unknown emission rates. Assuming each source emission to be independent, the prior PDF can be written as:

$$p(\mathbf{q}) = \prod_{j=1}^{N_S} p(q_j). \tag{2}$$

Assuming that the model and measurement uncertainties are independent and distributed normally, the total likelihood of all **c** for a given hypothesis of **q** is calculated as (Yee, 2012)

$$p(\mathbf{c}|\mathbf{q}) = \prod_{i=1}^{N_m} \frac{1}{\sqrt{2\pi}\left(\sigma_i^2 + \sigma_{m,i}^2\right)^{1/2}} \exp\left\{-\frac{\left(c_{m,i}(\mathbf{q}) - c_i\right)^2}{2\left(\sigma_i^2 + \sigma_{m,i}^2\right)}\right\}, \quad (3)$$

$\mathbf{c} \equiv \left(c_1, \ldots, c_i, \ldots, c_{N_m}\right)$, c_i is the observed concentration at *i*-th instant (time and location), $c_{m,i}$ is the corresponding modelled concentration for a given hypothesis of **q**, σ_i is the independent measurement error, $\sigma_{m,i}$ is the independent model error, N_m is the number of concentration data (which can be time series from several independent monitors). $c_{m,i}$ for all hypotheses, or possible values, for **q** is calculated and used in constructing the likelihood distribution $p(\mathbf{c}|\mathbf{q})$. Hence the posterior PDF for a given source hypothesis **q** is calculated as:

$$p(\mathbf{q}|\mathbf{c}) = \frac{1}{Z_0} \prod_{j=1}^{N_s} p(q_j) \prod_{i=1}^{N_m} \frac{1}{\sqrt{2\pi}\left(\sigma_i^2 + \sigma_{m,i}^2\right)^{1/2}} \exp\left\{-\frac{\left(c_{m,i}(\mathbf{q}) - c_i\right)^2}{2\left(\sigma_i^2 + \sigma_{m,i}^2\right)}\right\}, \quad (4)$$

where Z_0 is equivalent to $p(\mathbf{c})$ and is essentially a normalisation constant. The posterior yields probabilities of all emission rates (**q**) considered.

The total modelled concentration at a given location $\mathbf{x}_r$ and time is determined as

$$c_{m,i} = \sum_{j=1}^{N_s} c_{m,ij}. \quad (5)$$

Because methane is treated as a passive tracer, the concentration field simulated for one rate of emission can be scaled linearly for another without the need to re-run the model. Thus

$$c_{m,ij} = q_j \alpha_{ij}\left(\mathbf{x}_{s,j}, \mathbf{x}_{r,i}\right), \quad (6)$$

for each emission rate component of **q**. The quantity $\alpha_{ij}\left(\mathbf{x}_{s,j}, \mathbf{x}_{r,i}\right)$ is the source-receptor relationship or coupling coefficient and is equivalent to the modelled mean concentration at a given time and location $\mathbf{x}_{r,i}$ due to *j*-th source release at location $\mathbf{x}_{s,j}$ with a unit emission rate.

In Eq. (4), in the absence of an informative prior, a uniform prior PDF can be used with the given limits (q_{max}, q_{min})

$$p(q_j) = \frac{1}{q_{max,j} - q_{min,j}}, \quad (7)$$

with the probability being zero outside these bounds.

If the prior is Gaussian, then

$$p(q_j) = \frac{1}{\sqrt{2\pi}\,\sigma_{p,j}} \exp\left\{-\frac{(q_j - q_{p,j})^2}{2\sigma_{p,j}^2}\right\}, \quad (8)$$

where q_p and σ_p are the prior mean emission rate and its standard deviation, respectively.

High dimensionality of the posterior makes its direct computation and the subsequent integration (the 'brute-force' method) over the source-parameter space very expensive or perhaps even impossible. For Gaussian priors and uncertainties, the posterior can be solved for the mean and variance with their analytical matrix forms (Tarantola, 2005; Jeong et al., 2012). To make the inverse approach more generally applicable and efficient, we use a Markov chain Monte Carlo (MCMC) technique incorporating the Metropolis-Hastings algorithm to sample the posterior PDF (Tarantola, 2005; Yee, 2012). With MCMC, non-Gaussian priors or uncertainties, or parameters with known physical constraints can also be included (Miller et al., 2014). The normalization constant Z_0 in Eq. (4) need not be known before MCMC samples can be drawn from the posterior PDF. This ability to generate a sample without knowing this constant of proportionality (which is often extremely difficult to compute) is a major feature of MCMC algorithms (Luhar et al., 2014). The frequency distribution of the MCMC-generated samples represents the posterior.

The posterior PDF can be marginalized to obtain the mean emissions rate for each source as follows:

$$\bar{q}_j = \int q_j \, p(\mathbf{q}|\mathbf{c}) \, d\mathbf{q}, \quad (9)$$

and likewise, the variance can also be determined.

5.2 Construction of the hourly source-receptor relationship

In order to use hourly measurements, the source-receptor relationship needs to be calculated every hour for every source (real or potential) location and every monitor location using either forward or backward transport modelling (Rao, 2007). Generally speaking, if the number of source locations under consideration is greater than the number of receptor locations (as for the present case) then the backward approach is much more computationally efficient (Luhar et al., 2014).

In the backward approach, source matter is tracked backwards in time from a monitor treated as a source. The value at a given point of the constructed backward concentration field is analogous to the magnitude of contribution made by an emitting source at that point to the true (i.e. forward) modelled concentration at the monitor. Hence, we can use a single backward source-receptor relationship distribution determined every hour to get the contribution made by each real or potential source located in the domain. This contrasts with the forward modelling approach in which each source location ~~has to~~must be considered as a unique, separate source and its dispersion computed for every hour. Essentially, the source-receptor relationship furnishes a way to chart the distribution of source potential within given geographical domain. However, it does not quantitatively allocate the real contribution of sources within the domain to the concentration levels detected at monitoring stations— this is done by the Bayesian inference (Eq. (4)).

One backward approach for regional scale is to use backward trajectories constructed by only using three-dimensional winds computed from a meteorological model (e.g., Cheng et al., 1993). However, such wind trajectories only represent advective transport and do not account for turbulent mixing which causes a plume to disperse as it travels in the atmosphere. If measurements given at a high temporal resolution, e.g. hourly averages, are to be used for inversion it is necessary that the influence of atmospheric flow and dispersion processes that occur at such scales is considered. This can only be properly done by simulating backward tracer plumes which considers both advection and turbulent mixing.

We modify TAPM to construct backward dispersing plumes. The Eulerian dispersion module in TAPM comprises a solution of the advection-diffusion equation for the ensemble mean concentration c, which for a passive species is (e.g. Yee et al., 2008):

$$\frac{\partial c}{\partial t} + \bar{\mathbf{u}}.\nabla c - \nabla.(\mathbf{K}\,\nabla c) = S, \tag{10}$$

in which the unknown turbulent flux terms are closed using the K-theory or gradient transport approach. The forcing term S represents species emissions. The elements of the eddy diffusivity tensor $\mathbf{K}$ are zero except along its main diagonal (K_x, K_y, K_z). The diffusion is assumed to be symmetric in the horizontal plane, so $K_x = K_y = K_H$ (say). K_H and K_z are determined using the modelled turbulent kinetic energy (TKE) and the TKE dissipation rate.

The vertical component $\bar{w}$ of the mean wind vector $\bar{\mathbf{u}}$ ($\equiv \bar{u}, \bar{v}, \bar{w}$) in Eq. (10) is determined by using the continuity equation after the mean horizontal wind velocity components ($\bar{u}, \bar{v}$) are calculated.

The Eulerian adjoint of Eq. (10) describes the backward evolution of a scalar field (c^*), and is also termed backward or retro plume, adjoint function, sensitivity function, or influence function, and is given as (Marchuk, 1995; Pudykiewicz, 1998; Hourdin and Talagrand, 2006; Yee et al., 2008)

$$-\frac{\partial c^*}{\partial t} - \bar{\mathbf{u}}.\nabla c^* - \nabla.(\mathbf{K}\,\nabla c^*) = M, \tag{11}$$

where M is the forcing term representing the measurement distribution, which is treated as a source at the measurement (or receptor) location. Therefore, α_{ij} in Eq. (6) is equivalent to c^* derived for a unit emission rate.

The implementation of Eq. (11) in TAPM is done through changes in the forward model code as follows. The meteorological and turbulence fields calculated by the model at every hour (not hourly-averaged) are stored for the full simulation period. The modelled horizontal components ($\bar{u}, \bar{v}$) of wind are reversed (i.e. by sign change). The (inverted) vertical wind component ($\bar{w}$) is then calculated by solving the continuity equation given the reversed horizontal wind components. The turbulence parameters remain the same. The diffusivities in the dispersion component are positive and do not have any correction for counter-gradient flux in the vertical, and, therefore, they were not modified for the backward mode. The two monitor locations were treated as separate 'sources' each having unit emission, and hourly-averaged plume dispersion fields due to these

'sources' was determined by running the TAPM dispersion module backwards in time for the entire simulation duration by using the reversed winds calculated previously. The meteorological and turbulence fields were linearly interpolated in time for dispersion calculations for model time steps lying between two successive hours. The resulting hourly-averaged backward concentration fields were used as the source-receptor relationship. Since we assume that all methane sources are located near the ground within the lowest model level (i.e. 10 m AGL), only the 10-m hourly source-receptor relationship was required.

One complexity with doing a backward dispersion calculation using one continuous release over the full simulation period over a large domain, as done here, is that the source-receptor field at a given hour is a superposition of plume footprints from the current hour as well as previous hours (typically ~~up to~~ 4–5 hours for the present domain size). So, there is a time history in the source-receptor field at a given time (whose influence becomes smaller and smaller as the distance between the source and the receptor becomes smaller, the domain size decreases, ~~or~~ the averaging time is increased, or when the winds are strong). However, this time history in a backward run corresponds to future hours in a forward run, so at a given hour there can be a time mismatch between the forward concentration at a grid point and the backward concentration at that point. One way to deal with this problem is to do a backward simulation for every hour separately; however, this is extremely expensive computationally. As a practical and approximate solution~~fix~~ to this issue, at a particular backward travel hour (t) the plume travel time (t_r) from the release point (i.e. the monitor location) to a grid point ($\mathbf{x}$) is determined by releasing a second tracer (with concentration $c^* = c_2^*$) backwards from the monitor simultaneously with the main tracer (with concentration $c^* = c_1^*$) with the same tracer properties except that it decays exponentially with a decay rate of λ (= 10^{-6} s^{-1}), so

$$c_2^*(\mathbf{x}, t) = c_1^*(\mathbf{x}, t)\exp(-\lambda t_r), \tag{12}$$

which gives

$$t_r(\mathbf{x}, t) = \frac{1}{\lambda}\ln\left[\frac{c_1^*(\mathbf{x}, t)}{c_2^*(\mathbf{x}, t)}\right]. \tag{13}$$

The source-receptor value ($c^* = c_1^*$) calculated at a grid point location $\mathbf{x}$ at a given backward travel hour $t = t_b$ is then taken equal to that calculated at the same location at $t = t_b + t_r$ (where t_r rounded to the nearest hour). The forward travel hour for a grid point is ~~then~~ equal to the total hours in a simulation period minus t_b. Therefore, the source-receptor relationship (c^*) for the grid points at time t is constructed from the output of c_1^* at different times according to the value of t_r at individual grid points. A maximum value for t_r needs to be specified, which we take 15 h – approximately the time taken by the backward plume from either monitor to leave the (innermost) model domain (beyond this value, c^* is zero). This is needed to avoid occasional spurious smearing in the spatial patterns of c^* caused by a diluted, turning, or recirculating plume that has travelled longer than t_r overlapping the direct plume at a particular location.

To illustrate the modelled forward and backward relationship and the impact of accounting for t_r, Figure 7a presents the hourly-averaged forward modelled 10-m concentration field (c) in the innermost model domain on 20 June 2016 at 2300 h (local

standard time) due to a sample of 12 point sources, all emitting at the same fixed rate and whose locations correspond to some of the feedlots. Figure 7b is the backward modelled 10-m concentration field (c^*) for Ironbark (I) at the same time without the travel time correction (i.e. $t_r = 0$), and Figure 7c is the same field with the travel time correction. Essentially, the value at any point in the backward field is equivalent to the forward model concentration value at Ironbark if there were a source at that point with the same emission rate (as the backward emission rate). The backward concentration value at a given location represents the probability (including both frequency and intensity) a source emission at that location adds to the concentration at the monitoring site. The backward field is mainly determined by flow the field across the domain and the separation between the receptor and the source. Figure 7a suggests that only one source, S1, contributes to concentration at Ironbark. Figure 7c is consistent with this, in which the backward plume from Ironbark only impacts S1 with the same magnitude, and not any other source location. On the other hand, the backward plume in Figure 7b does not pass through any of the 12 sources, meaning no impact of these sources at Ironbark, which obviously is not correct as S1 does impact Ironbark. Figure 7c is the source-receptor relationship (normalised by the fixed emission rate) for Ironbark for the hour under consideration.

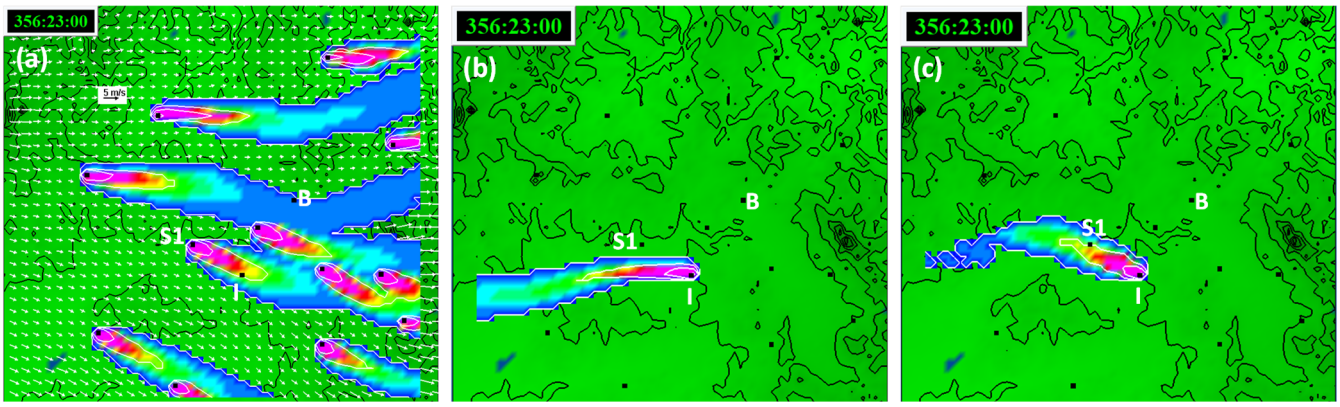

Figure 7. (a) Forward modelled hourly-averaged 10-m concentration field on 20 June 2016 at 2300 h (local standard time) due to 12 point sources, with the 10-m modelled winds also shown; (b) backward modelled 10-m concentration field for Ironbark (I) at the same time without the travel time correction ($t_r = 0$); and (c) backward modelled 10-m concentration field for Ironbark with the travel time correction. Each source point has the same emission rate. The plume contours (white) and colours represent the same concentration values. The black contours represent the topography. The model domain size is 370 × 370 km^2, and the Ironbark (I) and Burncluith (B) locations are shown.

A hourly-averaged modelled backward concentration field (c^*/q, s m^{-3}) at the lowest model level (i.e. 10 m AGL), an example of which is shown in Figure 7c, obtained for a unit emission rate (q = 1 g s^{-1}) is in essence the required hourly source-receptor relationship which can be linearly scaled for any other emission rate (q). ~~We use the hourly-averaged backward fields computed at the lowest model level (i.e. 10 m AGL) for the innermost model domain in our inverse methodology, an example of which is shown in Figure 7c.~~

~~As an example, Figure 8a presents the modelled backward concentration field ($/q$, s m^{-3}) due to a unit point release (q = 1 g s^{-1}) averaged over all hourly fields over the simulation period for Ironbark. Essentially, the value at any point in Figure 8a is equivalent to the simulation average forward model concentration value at this monitoring location if there were a source at that point with unit emission. Put differently, t~~The backward concentration value at a given location represents the probability ~~(including both frequency and intensity) a source emission at that location adds to the concentration at the monitoring site. The backward field is mainly determined by flow the field across the domain and the separation between the receptor and the source.~~

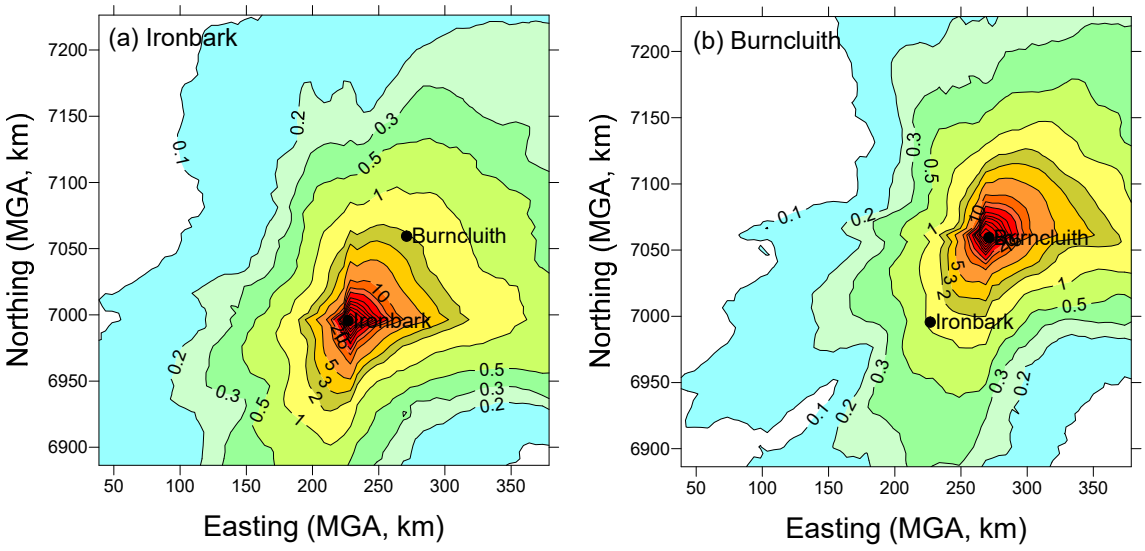

Figure 8. Normalised modelled backward distribution of near-surface concentration (c^*/q, × 10^{-9} s m^{-3}), which is an average over the entire study period: (a) Ironbark, and (b) Burncluith.

The modelled backward concentration field (c^*/q, s m^{-3}) averaged over all hourly fields over the simulation period for Ironbark is shown in Figure 8a, which suggests that, ~~It is apparent from Figure 8a that~~ overall, any sources located farther from the monitoring station would contribute less as plume concentrations decrease with increasing distances, and vice versa. The directional distribution of the backward field is also a function of the distribution of regional winds which determine how often the receptor is downwind of a source (see wind roses in Figure S3). The values in the south-east and north-west corners of the study domain are particularly low, so potential sources there would, on average, have low probability of being sampled at Ironbark.

The backward distribution for Burncluith (Figure 8b) is very similar, but since it is located north of Ironbark it would sample potential sources in the north-east better.

The two monitoring sites combined sample most part of the CSG sources in the domain (which was the prime objective of our monitoring).

5.3 Bayesian inversion setup

Assuming that emission rates are time invariant, we use all hourly methane data (N_m) from the two monitoring stations together in one combined Bayesian calculation to determine the total emission rates from gridded sources using Eq. (4). Since each hour corresponds to a unique meteorological condition, the use of all hours simultaneously provides the meteorological variability needed to achieve a better "triangulation" for source estimation. The greater the number of useful measurement hours, the greater the variability, and hence the better the constraining of the source. This approach is similar to that used by Luhar et al. (2014) in the context of a local point source. It requires the source-receptor matrix ($c^*(\mathbf{x}, t)$) for each hour for each measurement site (e.g. Figure 7c).

For the purposes of inferring emissions using our Bayesian methodology, t~~T~~he source array of 69 × 69 used in the forward modelling above is rather too large a source number ~~for the inverse methodology~~ to explore all the source possibilities (i.e. hypotheses)~~,~~ on hourly basis, even with use of the MCMC sampling. ~~, and, m~~Moreover, there is only a limited amount of information available from just~~only~~ two monitoring sites. A coarser array of sources is more practicable, and c~~C~~onsequently~~,~~ we consider an array of 11 × 11 localised sources ($N_s = 121$, cell size ~ 31 × 31 km^2) ~~is considered~~ within the same model domain, whose total emission rates are time invariant~~.~~ during a given simulation period. No sub-grid variability of these emission rates is considered. The hourly source-receptor relationships calculated at 5 × 5 km^2 resolution for Ironbark and Burncluith were used. Our inverse methodology used does not distinguish between different source categories. This is mainly because the concentration of methane alone was monitored and not tracers specific to methane source types. Therefore, there are no separate sources categories in the inferred emissions, unlike what was done for the forward simulation, and only total emissions are optimised.

~~We assume that all source emissions are time invariant during a given simulation period – this allows the utilisation of all valid hourly concentrations available during that period in a single Bayesian calculation to determine the (time invariant) emission rates.~~

To reduce serial correlations in the sequence of MCMC samples drawn from the posterior using the Metropolis-Hastings algorithm, we only retained every 5th sample. The total number of useable samples was 21,000 for each source, of which the first 1,000 samples were discarded as "burn-in" samples. The selected samples were then used in the calculation of the source statistics.

6 Inversion using the 'synthetic' concentration data

A 'synthetic' inverse run is first performed by using the simulated hourly time series of concentration at Ironbark and Burncluith involving the bottom-up inventory (regridded to 11 × 11 sources, see Figure 9a~~b~~) to investigate whether the inverse methodology is able to retrieve the bottom-up emissions and under what type of priors and their uncertainties. The results of this exercise provide a useful guidance to the subsequent inversion using the real-world data, particularly~~.~~ ~~The given modelled (or synthetic) time series do not directly possess any background, instrumental, and model errors and, therefore, prove very useful in validating an inversion methodology. The results from an inversion of synthetic data can provide guidance~~about the selection of the prior and its uncertainty specification ~~for an inversion using real-world data~~.

Only the forward modelled (or synthetic) concentrations at the two monitoring sites were used at times when valid (or filtered) methane observations were available ($N_m = 10581$). The measurement uncertainty was taken as σ = 3.5 ppb based on the previous calculation, and the uncertainty in the transport model was assumed to be σ_m = 20% of the modelled concentration (Yee and Flesch, 2010; Luhar et al., 2014). (These values will also be used later for the inversion based on the methane data.) ~~All hourly synthetic concentrations modelled for the full simulation period at the two sites (i.e. $N_m = 2 \times 13200$) were used in one single Bayesian inversion to derive the emission rates.~~

6.1 Selection of the prior

Specifying the prior PDF $p(\mathbf{q})$ is an important step, even for the present synthetic case because we are still limited to the same degree of information available (i.e. the modelled concentration time series from only two sites), the number of unknown sources to estimate, and the domain size as in the inversion case with the real concentration data considered subsequently. We specify the following two Gaussian priors:

- An identical (or uniform) Gaussian $p(\mathbf{q})$ for each source with a mean methane emission rate q_p = 45.4 g s^{-1} (= 1.43 × 10^6 kg yr^{-1}) per source is specified, with a specified standard deviation σ_p. This mean value is essentially the total bottom-up emission from the domain divided by the number of sources (i.e. 121).
- The bottom-up inventory emissions as a Gaussian prior. The inventory emissions shown in Figure 9a are taken as the mean values of a Gaussian prior for each source, with a specified standard deviation σ_p.

6.2 Results for the synthetic case

~~The emission rates inferred by the inverse model are shown in Figure 9a, with the total emission being 162 × 10^6 kg yr^{-1}, a figure very similar to the bottom-up inventory total 173 × 10^6 kg yr^{-1}.~~

In Figure 10a, the methane emission rates inferred by the top-down methodology for the uniform Gaussian prior case with a prior uncertainty of σ_p = 5% of the mean for each source are plotted against the bottom-up inventory sources used to construct the synthetic concentration time series for the inversion (the number of sources is 11 × 11). Ideally, the data points should fall

along the 1:1 line, but due to the limited amount of information supplied via the modelled concentrations from only two monitors and the prior being narrow and not very informative, most inferred emission emission rates are scattered around the prior mean, i.e. $q_p = 45.4$ g s^{-1}, although it is apparent that a few inferred emission rates are greater than this value and tending to the corresponding bottom-up emission rates. The spatial distribution of the inferred emissions is presented in Figure 9b, which, as expected, is much more uniform than the inventory emissions in Figure 9a.

When the prior uncertainty is increased to $\sigma_p = 10\%$ of the mean(Figure 10b), the scatter increases, but most inferred emissions stay around the prior mean, barring some higher-end ones which move further closer to the corresponding bottom-up emission rates. Further increase in σ_p leads to a larger increase in scatter, with no improvement in the inferred emissions.

The total infrared emissions are 179.3×10^6 and 175.7×10^6 kg yr^{-1} for $\sigma_p = 5\%$ and 10% of the mean, respectively – values very similar to the bottom-up inventory total 173.2×10^6 kg yr^{-1}.

Figure 11a is the same as Figure 10a except that the Gaussian prior with the individual bottom-up inventory emissions as its mean values has been used. The inversion retrieves the bottom-up emissions very well with a little scatter in the data points. The spatial distribution of the inferred emissions is presented in Figure 9c for this case, which is very similar to that of the inventory emissions in Figure 9a. As the prior uncertainty is increased to $\sigma_p = 10\%$ of the mean (Figure 11b), the uncertainty in the retrieved emissions gets larger, with a slight decrease in the correlation.

The total infrared emissions corresponding to Figure 11a and Figure 11a are 164.8×10^6 and 156.9×10^6 kg yr^{-1}, respectively – values somewhat smaller than the inventory total 173×10^6 kg yr^{-1}.

A comparison of Figure 9c~~a~~ with the bottom-up inventory (Figure 9a~~b~~) indicates that some regions in the south-east, for example the strong coal mining source at the grid location (11, 4), and north west corners are not replicated as well by~~that~~ the inverse model ~~is able to simulate the large emission rate in the region located just north of the Ironbark site. There is a strong inventory emission on the eastern domain boundary which the model does not replicate~~. This is despite a perfect/strong prior with a relatively small uncertainty, and could be due to the fact that ~~A possible reason for this is that~~ the two monitoring locations~~stations~~ do not sample this source area sufficiently (see Figure 8). Extra monitoring stations and/or separate, narrower priors for sources that make very small contributions to methane at the two sites would be needed to cover these areas better~~reduce the differences between Figure 9a and Figure 9b~~.

The above synthetic case results suggest that with only two monitoring locations the bottom-up inventory Gaussian prior works well and is, indeed, needed. Obviously, a small prior uncertainty biases the inferred emission distribution towards the prior $p(\mathbf{q})$, and what uncertainty level is selected depends on the available information supplied to the inversion. The synthetic case reveals that $\sigma_p \sim 5\%$ of the mean is needed to retrieve the bottom-up emissions. Thus, for a real inversion using the methane measurements one may expect that a tighter prior uncertainty would be needed. Further guidance on σ_p can also comes from

comparison of the forward modelled methane concentrations using the inferred emissions with the methane observations from the two sites.

The synthetic case results also demonstrated~~suggest~~ that the regional inverse model formulated was~~is~~ stable and~~,~~ feasible with MCMC~~., and credible as evident from its getting the total emissions nearly right and replicating the largest emission area reasonably well with only a broad prior and two monitoring locations, but at the same time requiring a relatively small prior uncertainty. The synthetic case considered is an overly demanding case because the prior used is not very informative, compared to the real inversion cases considered in the next section in which the bottom-up inventory emissions allow the option of a better prior.~~

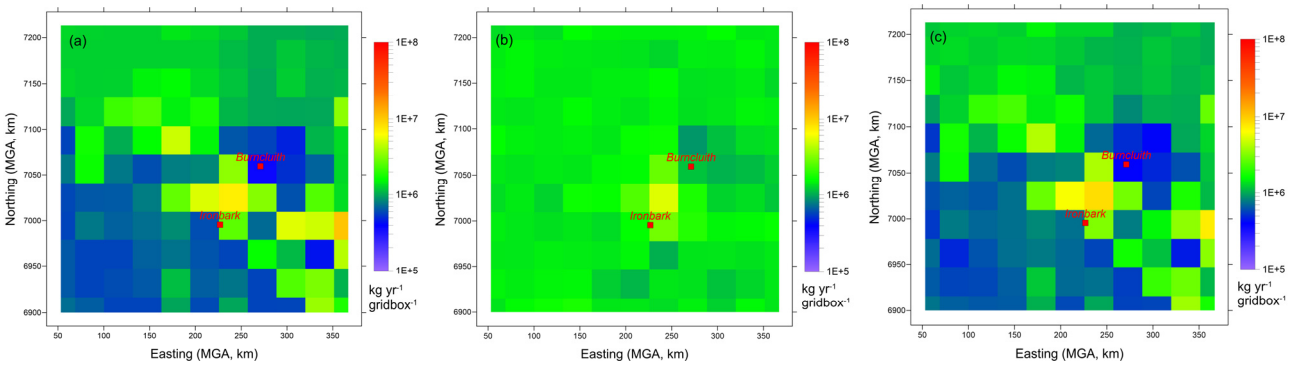

Figure 9. ~~(a)~~ Emission rates of CH_4 (kg yr^{-1} gridcell^{-1}) (a) based on the bottom-up inventory, (b) estimated by the synthetic inversion using a uniform Gaussian prior with an uncertainty of σ_p = 5% of the mean for each source~~, and (b) bottom-up inventory emission rates~~, and (c) estimated by the synthetic inversion using the bottom-up inventory in (b) as a Gaussian prior with an uncertainty of σ_p = 5% of the mean for each source. There are 11 × 11 sources.

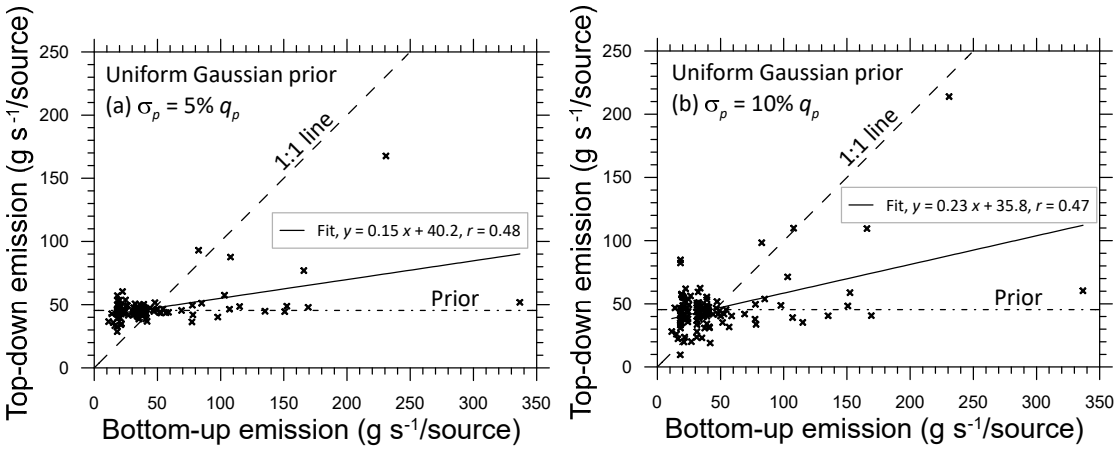

Figure 10. Scatter plot of the bottom-up inventory methane emission rates (g s^{-1} per source) versus those inferred from the inverse (top-down) methodology for the synthetic case involving a uniform Gaussian prior with a prior uncertainty of (a) σ_p = 5% and (b) σ_p = 10% of the mean for each source. The number of sources is 11 × 11. The dash-dot line is the mean value of the prior, the dashed line is the 1:1 line (i.e. perfect agreement) and the solid line is the least-squares fit.

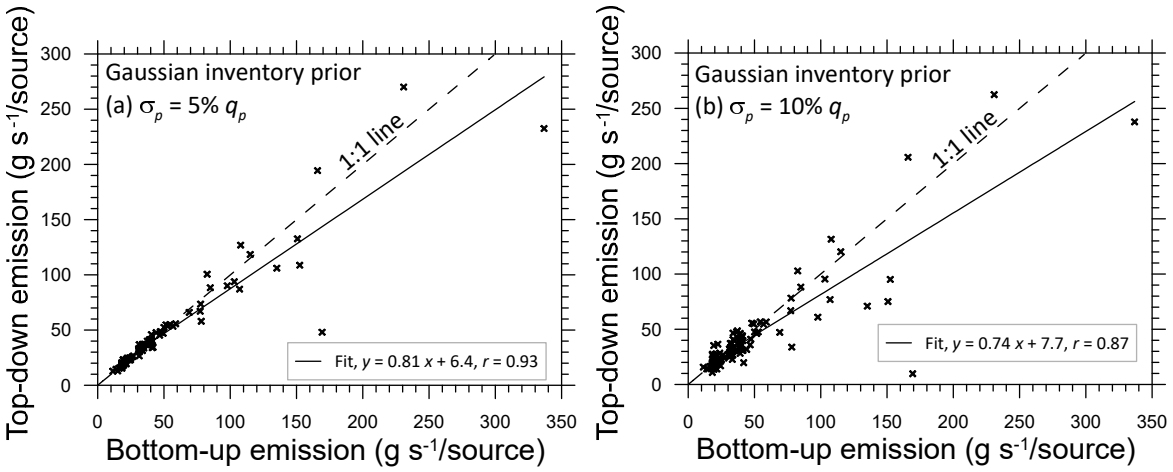

Figure 11. Scatter plot of the bottom-up inventory methane emission rates (g s^{-1} per source) versus those inferred from the inverse (top-down) methodology for the synthetic case involving the inventory source emissions as the mean of a Gaussian prior with a prior uncertainty of (a) σ_p = 5% and (b) σ_p = 10% of the mean for each source. The number of sources is 11 × 11. The dashed line is the 1:1 line (i.e. perfect agreement) and the solid line is the least-squares fit.

7 Inversion using the methane measurements

We now use the filtered methane measurements from the two monitoring stations to quantify emissions using our inverse methodology. The above synthetic case results have revealed that a good, tight prior is needed to infer emissions within the selected domain using concentrations from the two monitoring locations. One may, of course, ask as to how the source inference using the real-world measurements is influenced depending on the type of prior that may be available, ranging from a non-informative one to the most informative we have, i.e. the bottom-up inventory.

We use t~~T~~he same filtered methane observations as used in the forward transport modelling (so $N_m = 10581$) ~~are used~~ in a~~one~~ single Bayesian inverse run. ~~, with t~~The uncertainty in the measurements is σ = 3.5 ppb ~~based on previous calculation~~ and the modelled uncertainty is σ_m = 20% of the mean~~modelled~~ concentration, as used in the synthetic inversion~~(Yee and Flesch, 2010; Luhar et al., 2014)~~.

7.1 Priors and inferred emissions

Three cases involving different priors are considered.

7.1.1 Non-informative uniform prior (Case 1)

A case of ~~virtually no prior, or~~ non-~~un~~informative prior~~,~~ is first considered~~,~~ in which the only constraint is that the emission rate for each source lies within the broad range 10–10,000 g s^{-1}~~,~~ with uniform probability, where the upper limit is nearly double the total domain-wide bottom-up inventory.

The inferred emissions (Figure 12a) between the two monitoring sites and around the centre of the region are qualitatively in accordance with the bottom-up inventory emissions (Figure 9a~~b~~), but with larger magnitudes. In contrast, the inverse estimates in locations farther from these source areas are smaller than the inventory emissions. Remarkably, the total inferred emission with the non-informative prior is 162 × 10^6 kg yr^{-1} which compares well with the inventory total. The largest emission rate of about 1100 g s^{-1} in Figure 12a is about 10% of the upper bound of the specified prior range.

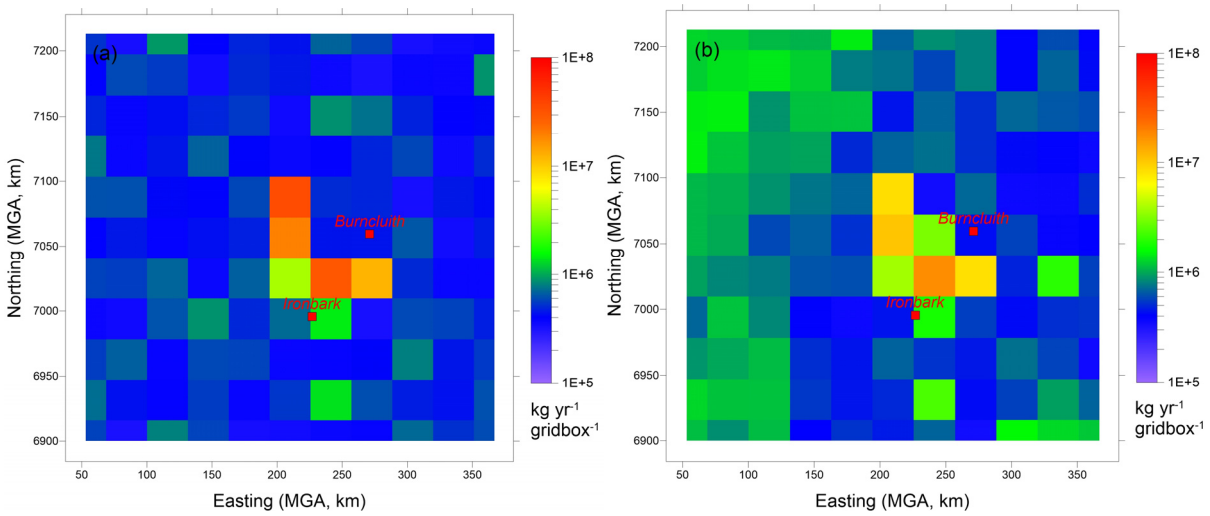

Figure 12. Emission rates of CH_4 (kg yr^{-1} $gridcell^{-1}$) estimated by the inversion: (a) with a non-informative uniform prior (Case 1); and (b) with a uniform Gaussian prior (Case 2).

7.1.2 Uniform Gaussian prior (Case 2)

Next, a more realistic prior PDF is specified with a Gaussian distribution having an identical mean of 45.4 g s^{-1} and σ_p = 10% of the mean, for each source. The mean is the same as that is used in one of ~~for~~ the synthetic runs.

The inferred emissions for this case shown in Figure 12b are qualitatively similar to Figure 12a; however, in the former the high emission sources are relatively less pronounced, with emissions from other source locations generally being larger. The total annual emission from the Surat Basin obtained using this inversion is 143 × 10^6 kg yr^{-1}.

7.1.3 Gaussian prior with the bottom-up inventory emissions (Case 3)

In this case, the inventory emissions shown in Figure 9a~~b~~ are taken as the mean values of a Gaussian prior for each source. As every source prior now has a more realistic specification of the mean value compared Case 2, the uncertainty in the prior is chosen to be smaller than that specified in Case 2. A small prior uncertainty is also guided by the synthetic case results presented earlier.

The inferred emission rates in Figure 13a obtained for Case 3 with σ_p = 1% of the mean (Case 3a) appear very similar to the inventory emission rates (Figure 9a~~b~~). The fact that even the intense emission on the eastern boundary of the domain present in the inventory is mostly reproduced despite this area being not sampled relatively sufficiently by the two network locations means that the chosen prior with a very small uncertainty is somewhat too inflexible which forces the inversion towards a result that is very similar to the prior itself, thus in essence overriding the information inherent in the concentration observations.

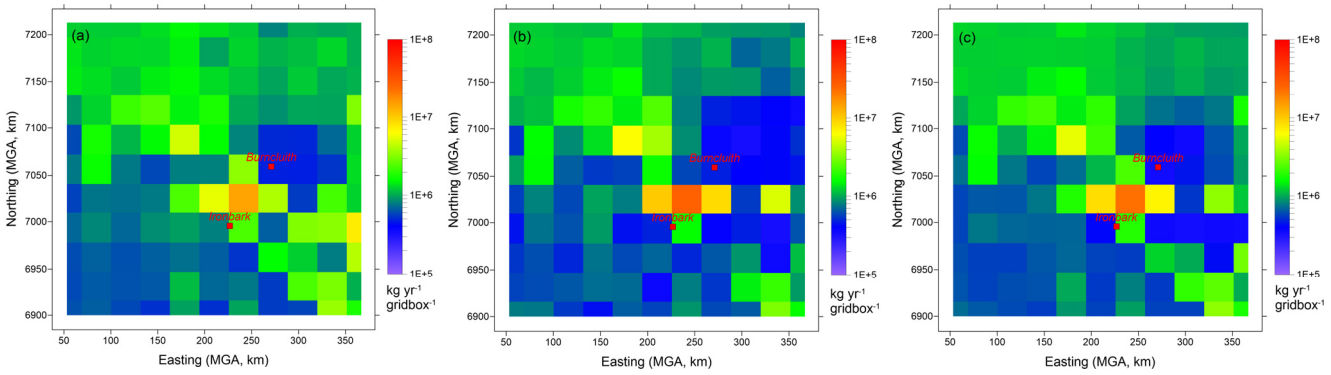

Figure 13. Emission rates of CH_4 (kg yr^{-1} $gridcell^{-1}$) estimated by the inversion with a Gaussian prior involving mean values equal to the bottom-up emissions (Figure 9a~~b~~) and the standard deviation equal to (a) 1%, (b) 5% and (c) 3% of the mean values.

Figure 13b is obtained using the same inverse model setup as Figure 13a, except that the prior is relaxed somewhat by increasing σ_p to 5% of the mean (Case 3b). This leads to the source areas in the centre of the Surat Basin and those between Ironbark and Burncluth becoming more conspicuous. In contrast, the source areas near the eastern boundary of the domain nearly fade, with the concentration observations applying greater influence in areas where the source-receptor relationship, shown in Figure 8, is stronger. Clearly, the inversion is sensitive to σ_p, however, it is apparent that σ_p = 1% to 5% of the mean yields a reasonable trade-off between the benefit of the inversion approaching the prior in areas where the chances of the two monitoring stations detecting methane signal is small and simultaneously making sure that the selected prior would not unduly overrule the information supplied by the concentration measurements. Consequently, another inversion was performed for σ_p

= 3% of the mean (Case 3c). The inferred emission from this run presented in Figure 13c in essence stand between the inferred emissions for σ_p = 1% and those for 5% of the mean. This Case 3c inversion ~~with σ_p = 3%~~ is our best estimate, which gives an annual total CH_4 emission of 165.8 × 10^6 kg yr^{-1}. The fine tuning of prior uncertainty also has some trial and error component driven by the need that the inferred emissions are able to describe the measured concentrations when used in a forward model simulation (see the validation Section 7.2).

As noticed in the synthetic inversion case, and in Figure 13a and Figure 13b, a large prior uncertainty biases the inversion towards emission rates that have high probability, which may indicate that the number of monitoring stations is insufficient for the uncertainty in the prior to be relaxed.

Figure 14a presents the difference between the inferred methane emissions given in Figure 13c and the bottom-up inventory emissions in Figure 9a~~b~~. The largest difference is found for the grid box between Ironbark and Burncluith, with the inferred emissions (22.9 × 10^6 kg yr^{-1}) being larger by approximately a factor of three than the latter (7.3 × 10^6 kg yr^{-1}). The total inventory emission for this source grid is controlled by CSG Processing (51%); feedlots, poultry and piggeries combined (32%); and CSG Production (6%) sectors.

The calculated posterior uncertainty (standard deviation) relative to the inferred mean emissions (%) ~~The calculated standard deviation of the inferred emissions~~ corresponding to ~~the case shown in~~ Figure 13c (Case 3c, σ_p = 3% of the prior mean) is presented in Figure 14b. Most of t~~T~~hese values are very similar to the relative uncertainty in the prior (i.e. σ_p = 3% of the prior mean).~~approximately 1-2 orders of magnitude lower than the mean emission rates in Figure 13c. In general, the standard deviations are larger for larger inferred emissions. One reason as to why these uncertainties in the emission posterior are quite low, as discussed above, is the very small prescribed uncertainty that needs to be specified in the prior.~~ Interestingly, the farthest grid point east of Ironbark (11, 4), which corresponds to a relatively strong coal mine source in the bottom-up inventory (Figure 3d), has a disproportionally large uncertainty (~ 25%~~compared to the mean) emission rate in Figure 13c~~.

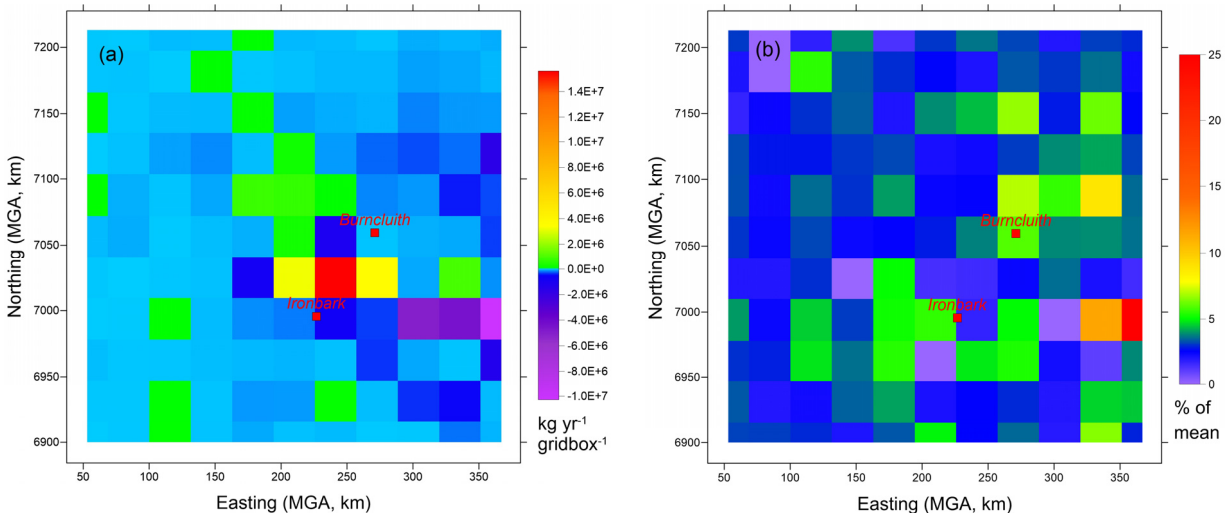

Figure 14. (a) Difference between the inferred methane emissions (Figure 13c) and the bottom-up inventory emissions (kg yr^{-1} gridbox^{-1}), and (b) posterior uncertainty (standard deviation) relative to the ~~(uncertainty) of the~~ inferred mean emissions (%~~kg yr^{-1} gridbox^{-1}~~) presented in Figure 13c (Case 3c).

7.2 Validation of the inverse emission estimates

To examine to what extent the inferred emissions represent the methane concentration measurements compared to the bottom-up emissions, we conducted three separate forward transport model runs using the inferred emissions from the above inverse modelling Cases 1, 2, and 3 (i.e. Figure 12a, Figure 12b and Figure 13~~e~~, respectively).

~~Figure 15a presents~~ The q-q plots of the observed data against the modelled CH_4 computed using the Case 1 inferred emissions (Figure 15a, d) show that~~.~~ ~~t~~There is an overestimation of methane at both monitoring stations for the higher-end concentrations, but the simulated CH_4 at Ironbark is much better reproduced than when using the bottom-up emissions (grey lines). For Burncluith, the overestimation is almost as large in magnitude as the underestimation obtained when the inventory emissions are used.

~~As demonstrated by Figure 15b, T~~the Case 2 inferred emissions involving a proper, but still crude, prior lead to a significant improvement in the methane simulation, especially at Burncluith (Figure 15b, e).

As apparent from Figure 15c, f, the use of the bottom-up inventory as ~~further refinement in the~~ the prior in Case 3c with 3% prior uncertainty relative to the mean yields emission estimates that further improve the simulation of methane, especially at Ironbark. Comparatively, the use of 1% prior uncertainty leads to a better performance at Ironbark but worse at Burncluith. With 5% prior uncertainty, the performance is other way round. With the exception of about 4 outlying data points at the higher-end of the concentration distribution, the Case 3c inversion with 3% prior uncertainty (corresponding to ~~Figure 12e~~

Figure 13c) leads to the best overall model reproduction of the measured CH_4 from the two monitoring sites. The underprediction seen when the inventory emissions are used (grey curves in Figure 15) is nearly eliminated.

Table 1 presents performance statistics for the three Case 3 inversions and for the bottom-up emissions as to how well they describe the methane concentration measurements at the two sites when used in the forward modelling. The observed (O) and modelled (M) concentrations are paired in time for these statistics, which are: r = correlation coefficient, IOA = index of agreement, a = slope and b = intercept of the linear best fit line, FB = fractional bias, and RMSE = root mean square error. FB = $2(\bar{O} - \bar{M})/(\bar{O} + \bar{M})$, which varies between -2 (overestimation) and +2 (underestimation); and IOA = $1 - [\overline{(M - O)^2}/\overline{(|M - \bar{O}| + |O - \bar{O}|)^2}]$, where 0 = no agreement and 1 = perfect agreement. The IOA, unlike r, is sensitive to differences between the observed and model means as well as to certain changes in proportionality.

Compared to the bottom-up emissions, the inferred emissions improve the prediction of methane at Ironbark, except for a slight decrease in correlation. At Burncluith, the improvement is limited to the slope. Note that these statistics are dominated by lower-end concentrations which are much more numerous than the higher-end concentrations. The q-q plots in Figure 15 on the other hand tend to emphasise more model performance for a small number of higher-end concentrations.

Some deterioration in the model performance when the inferred emissions are used could be caused by the 11 × 11 source distribution representing the emissions in the domain being rather coarse (compared to 69 × 69 used for the bottom-up emissions). Considering the performance statistics in Table 1 and the q-q plots in Figure 15c and f, the Case 3c inversion is our best estimate of emissions.

Table 1: Performance statistics for the emissions from the Case 3 inversions and for the bottom-up emissions as to how well they describe the methane concentration measurements when used in the forward modelling (r = correlation coefficient, IOA = index of agreement, a = slope, b = intercept, FB = fractional bias, RMSE = root mean square error).

Emissions	Ironbark (N = 6432)						Burncluith (N = 4149)					
	r	IOA	a	b (ppb)	FB	RMSE (ppb)	r	IOA	a	b (ppb)	FB	RMSE (ppb)
Case 3a ($\sigma_p = 1\%\ q_p$)	0.53	0.68	0.36	1153	0.61×10^{-3}	25.5	0.69	0.82	0.71	527	-0.45×10^{-3}	11.1
Case 3b ($\sigma_p = 5\%\ q_p$	0.49	0.66	0.55	863	-1.98×10^{-3}	32.0	0.58	0.71	0.87	244	-1.26×10^{-3}	16.8
Case 3c ($\sigma_p = 3\%\ q_p$	0.51	0.68	0.48	954	-0.72×10^{-3}	28.4	0.63	0.76	0.79	381	-0.86×10^{-3}	14.0
Bottom-up emissions	0.57	0.59	0.25	1360	3.36×10^{-3}	25.4	0.74	0.84	0.61	707	0.35×10^{-3}	9.4

~~Clearly, differences between the model and observations remain, and the possible causes for that include differences between the observed and modelled regional meteorology, only two monitoring sites within a relatively large study domain, the selected~~

~~11 × 11 source distribution representing the emissions in the domain being rather coarse, and potential temporal variation of source emissions.~~

755

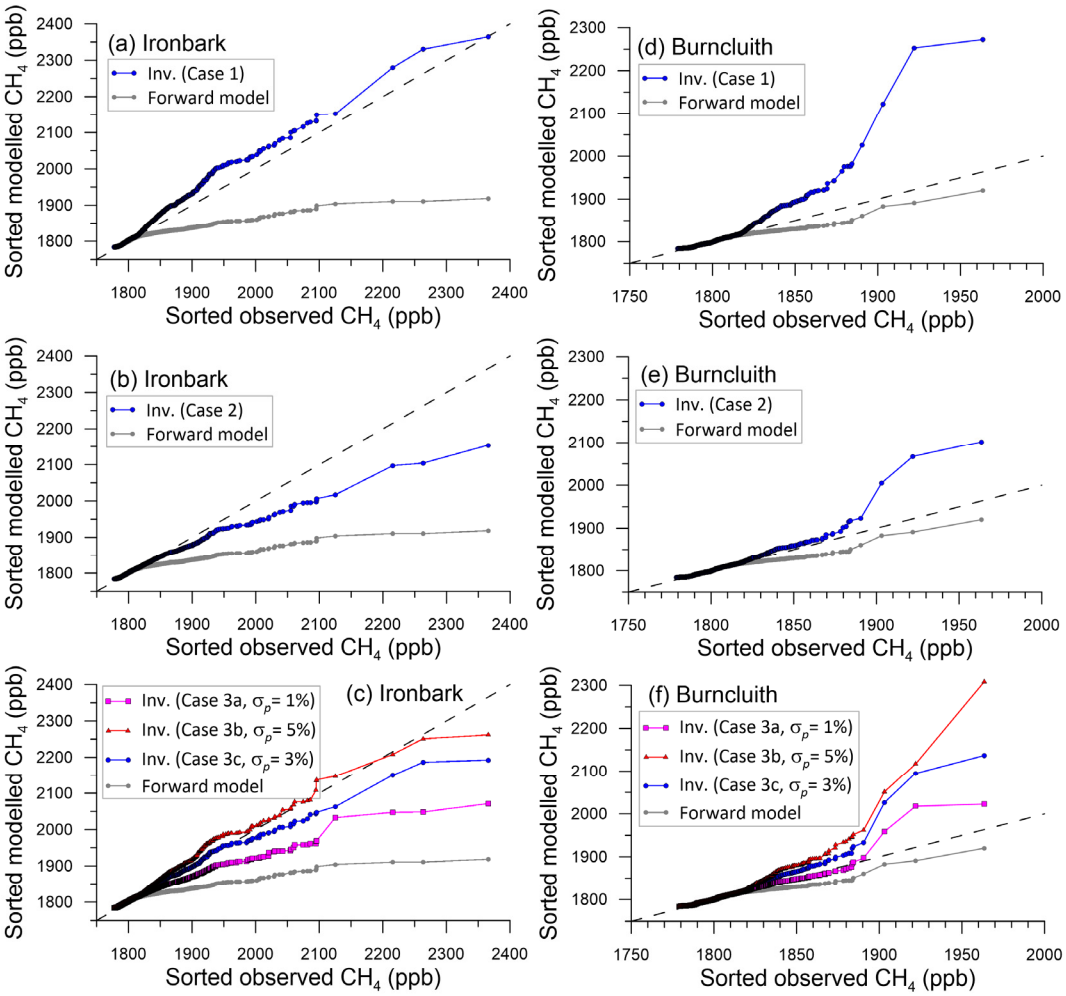

Figure 15. Q-q plots showing the sorted hourly observed versus the sorted modelled CH_4 at the Ironbark and Burncluith monitoring stations. The modelled concentrations utilise emission estimates from (a) Case -1 inversion, (b) Case -2 inversion, and (c) Case -3 inversions (i.e. with 1, 3, and 5% uncertainty in the prior relative to the mean). The forward model concentrations from Figure 6 predicted using the bottom-up emissions are shown as grey lines. Dashed line represents perfect agreement.

7.3 Emissions from the CSG area

Given the focus on CSG activity related emissions in the Surat Basin, we compare the aggregate bottom-up and inferred emissions from the CSG areas, many of which are concentrated near and between the two monitoring stations. The subdomain that includes all the CSG sources in the study area is shown Figure 16, which is an area of about 18260 km^2, ~~and covers~~ 15% of the study domain, covers 19 of the 121 source grids considered. The CSG subdomain also contains emissions from other sectors (see Figure 3).

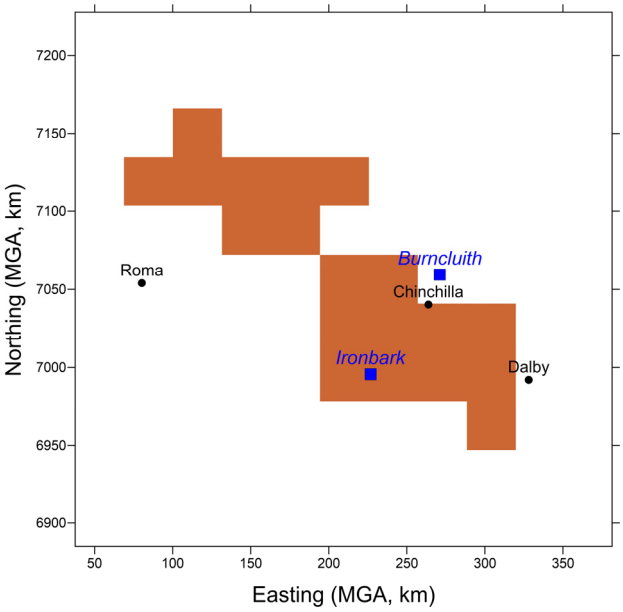

Figure 16. A subdomain of the study area that corresponds to all the CSG source areas (shaded grid cells) in the bottom-up emission inventory. It coverseconsists of 19 of the 121 source gridsgridcells (each with a source footprint of 31 × 31 km^2) considered in the inverse modelling.and is considered for aggregating emission rates.

The total bottom-up inventory emissions from the CSG sub-domain is 47.7 × 10^6 kg yr^{-1} (cf. 173.2 × 10^6 kg yr^{-1} for the domain) whereas that obtained using the inversion (Case 3c, Figure 13c) is 63.6 × 10^6 kg yr^{-1} (cf. 165.8 × 10^6 kg yr^{-1} for the domain) which is 33% larger than the former. The total bottom-up emission for this subdomain is dominated by CSG (34.7%, of which 30.6% is due to CSG Processing), followed by grazing cattle (29.9%), feedlots (23.5%) and coal mines (7.7%), which together account for 95.8% of the emissions from this area. Since the inverse methodology does not differentiate between source sectors, emissions from individual sectors cannot be inferred. Considering that the grazing cattle emissions are diffuse sources and thus not responsible for peaks in the measurements that dominate the inverse estimates, and since feedlots are scattered throughout the domain (Figure 3c) including the non-CSG areas from where there is no general inference of higher emissions, it is plausible that the increase in the inferred emissions would mainly correspond to CSG as the source sector.

A considerable portion of the CSG emissions is in the area between the two monitoring stations. The inferred emissions in this area are much greater than the corresponding bottom-up inventory emissions. This area also has significant coal mining emissions nearby (Figure 3d). It is possible that the methane emissions from a combination of these two source sectors are much larger than the inventory emissions.

Conversely, the total bottom-up inventory emissions from the non-CSG area is 125.5 × 10^6 kg yr^{-1} whereas that obtained using the inversion (Case 3c) is 102.2 × 10^6 kg yr^{-1} which is 18.5% lower than the former. The total bottom-up emission for this area is dominated by grazing cattle (62.7%), followed by feedlots (24.8%) and coal mines (8.6%), which together account for 96.1%

of the emissions from this area. It is possible that the emission factor of 84 kg CH_4 animal^{-1} yr^{-1} for Australian grazing cattle (Harper et al., 1991) used in the bottom-up inventory (see the Supplement S6) is an overestimate (cf. 51 kg CH_4 animal^{-1} yr^{-1} for beef cattle (pasture) used by the Australian National Inventory Report (NIR, 2017) or 63 kg CH_4 animal^{-1} yr^{-1} for non-dairy cattle for the Oceania (IPCC, 2019)), and that would be consistent with the lower top-down methane emission from the non-CSG area compared to the inventory. This also means that the CSG component of the top-down emissions in CSG sub-domain could be higher to compensate for the lower grazing cattle emissions if a lower emission factor for grazing cattle is used.

Apart from the uncertainties associated with the bottom-up emissions, potential methane emissions from some sources, namely wetlands (the amount of which in the area is very limited; https://wetlandinfo.des.qld.gov.au), land clearing, termites, material handling and fuel usage related to mining activities, ground-water wells, and biomass burning are not part of the bottom-up emissions. In contrast, all CH_4 sources are implicitly represented in the inversions, apart from the biomass burning events which have been filtered using the CO filter. It is difficult to pinpoint which source sectors might be underrepresented in the bottom-up inventory without some kind of source discrimination, for instance, through the use of tracers such as the CH_4 isotopes.

7.4 Temporal variation of the inferred emission

In the previous inverse calculations, all filtered methane measurements obtained during July 2015–December 2016 were combined in a single~~one~~ Bayesian calculation to derive a time invariant top-down emission distribution. Here we apply the inverse model with the Case 3c settings (as used for Figure 13c with 3% prior uncertainty relative to the mean) to 3-monthly measurement blocks within the above period in order to examine potential temporal variation of the inferred emissions. Obviously, for a 3-monthly simulation the amount of concentration data supplied to the Bayesian inversion is much less than that for the full simulation. Figure 17a presents the 3-monthly variation of the inferred emissions as kg CH_4 yr^{-1} (bar plots), along with the (constant) bottom-up inventory emissions (red line) and the (constant) inferred emissions from Case 3c (blue line). The 3-monthly emission rates are within 165–180 kg yr^{-1} and are generally larger than when the full measurement duration is considered. This is because as the amount of information supplied to the inverse model reduces, the inferred emissions are not modulated to the same extent as that for the full period, and thus they tend to move closer to the bottom-up inventory which is used as a prior with a tight uncertainty. (Time-varying inventory emissions, if available, would act as a better prior, together with additional measurement sites).

Figure 17b is the same as Figure 17a but for the CSG subdomain. The 3-monthly inferred emissions lie between the bottom-up inventory value and the inferred value obtained when the measurements from the full period are used. Again, as in Figure 17a, 3-monthly inferred emissions push towards the inventory value as the information supplied to the inverse model reduces.

Figure 17c is the same as Figure 17a but for the non-CSG subdomain (which is dominated by grazing cattle emissions (62.7%) as per the bottom-up inventory). In this plot, we also present a 3-monthly climatological average (1992 – current 2020) of rainfall at the Dalby airport (location 27.16°S, 151.26°E), located next to the town of Dalby, within the study domain. The

rainfall data were obtained from the Australian Bureau of Meteorology (http://www.bom.gov.au/climate/averages/tables/cw_041522.shtml). There is a good correlation (r = 0.79) between the 3-monthly inferred non-CSG methane emission and the rainfall, suggesting that the inferred emission variation could, to some extent, be attributed to the seasonality of pasture growth and wetlands, –influenced by rainfall. This correlation for the 3-monthly inferred emissions from the full domain (Figure 17a) is 0.71 and it is -0.06 for those from the CSG subdomain (Figure 17b). Assuming that the higher the rainfall the higher the grazing cattle (and wetland) emissions, these r values indicate that the seasonal variability of the inferred emissions within the full domain is also influenced by grazing cattle, but the inferred emission seasonality for the CSG area cannot be linked with grazing cattle seasonality.

Another potential contributor to the temporal variability in the inferred emissions in Figure 17 is the seasonality of the winds in the area which influence the source-receptor relationships. We have not explored this possibility here.

The uncertainties in the inferred seasonal emissions Figure 17 is around 5% of the mean – a relatively small value largely the result of a tight prior.

To test how well the ~~The~~ temporal variation~~s~~ of the inferred emissions represents reality, ~~in Figure 17a and Figure 17b are qualitatively similar. It is difficult to know whether these variations truly represent reality. Again,~~ we conducted a forward TAPM run using these ~~3-monthly~~ emissions ~~from the above inversion~~, and the resulting q-q plots (red dots) are shown in Figure 18. The methane data at Burncluith are best described by these 3-monthly varying emissions compared to any other emission setup, but at Ironbark, these emissions underestimate the methane data (the inversion setup corresponding to Figure 15c best describes the Ironbark data).– Additional measured parameters (e.g. tracers), as well as more monitoring stations and other additional data (e.g. about the prior), would be useful in further constraining the emissions.

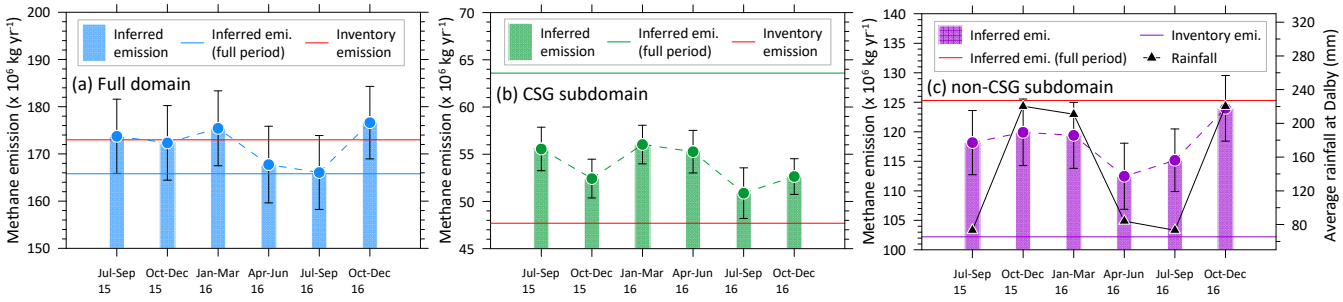

Figure 17. 3-monthly~~Temporal~~ variation of the inferred emissions (bar plots), including one standard deviation uncertainty (~5% of the mean), for (a) the full study domain, ~~and~~ (b) the CSG subdomain, and (c) the non-CSG subdomain. The respective constant bottom-up inventory emissions (red line) and the constant inverse/inferred emissions from Case 3c (Figure 13c) are also shown. Note the emission units.

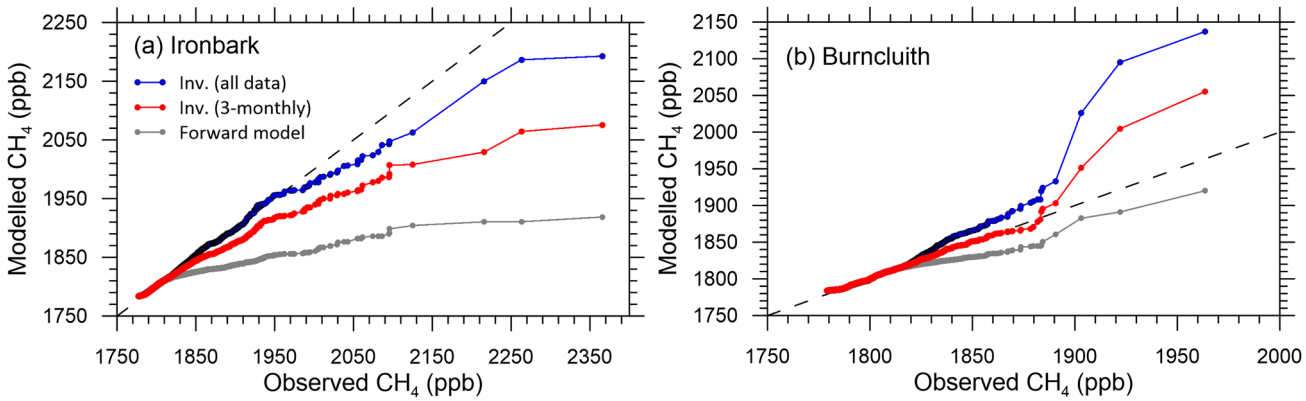

Figure 18. Q-q plots showing the sorted hourly observed versus the sorted modelled CH_4 at the two monitoring stations. The modelled values (blue dots) are predicted using the emissions from Case ~~-~~3c inversion (with 3% uncertainty in the prior relative to the mean); the red dots are produced from 3-monthly inversions; and the forward model concentrations from Figure 6 predicted using the bottom-up emissions are shown as grey lines. Dashed line represents perfect agreement.

Given the rapid rise in the CSG production~~development~~ in the Surat Basin, one may deduce that the 2016 CSG methane emissions were larger than the 2015 bottom-up emissions and, therefore, could potentially explain the top-down emissions in the CSG area being higher than the inventory emissions. Figure 19 shows that compared to July–December 2015, the total CSG produced was higher by 32% during January–June 2016 and by 45% during July–December 2016, ~~(~~which correlates with an increase in the number of CSG production wells in the area~~)~~. However, Figure 19 also shows that there is a downward trend in the amount of flared/vented gas. Considering, based on the bottom-up inventory in Section 3, that venting (from processing) is the biggest contributor (88%) followed by flaring (8%) (from both processing and production) to the total CSG methane emissions, it is plausible that despite the increase in the CSG development in the area the CSG-related methane emissions have not increased, and that they may have even gone down. The temporal variation of the inferred emissions in ~~However, notwithstanding the limited number of data available in deriving the top-down trend in~~ Figure 17b ~~and the 2015 bottom-up inventory used as the prior and assuming that the CSG area remains the same, this figure~~ for the CSG dominated area also does not indicate~~support~~ any consistent increase in emissions from 2015 to 2016. ~~As stated in Section 3, the main contributor to the total inventory CSG methane emissions was venting, followed by flaring. Figure 16 suggests that although the amount of CSG produced steadily increased until 2017, the amount of venting/flaring does not show any such trend. As a matter of fact, overall, there is a decreasing trend in venting/flaring. Therefore, an increase in the amount of CSG produced doesmay not necessarily mean that the methane emissions would have increased proportionally.~~ Thus, the 33% higher top-down emission estimate from the CSG area compared to the inventory estimate cannot be explained in terms of the growth in the CSG production from 2015 to 2016 and is possibly related to underestimated or missing emissions in the inventory. This also implies that the emissions from CSG may be more closely related to practices in the industry than to the amount of CSG produced.

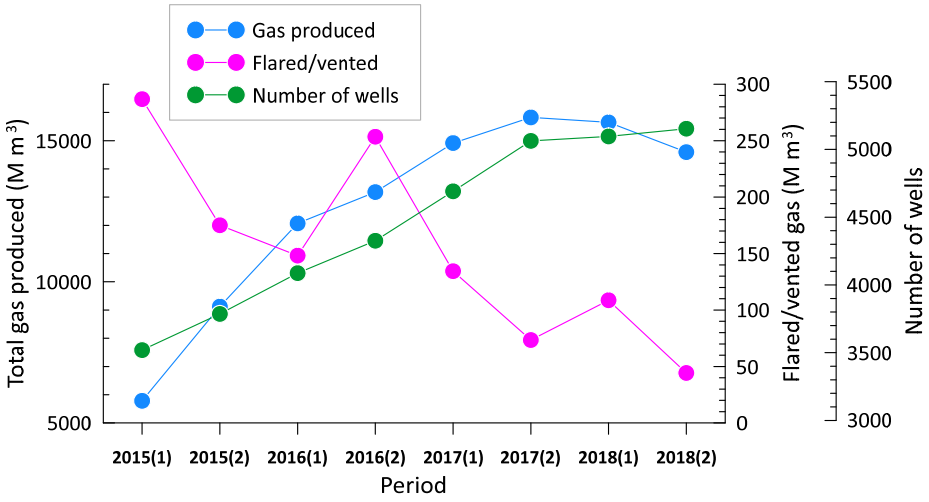

875

Figure 19. Six-monthly trends of the total CSG produced, ~~and the~~ amount of flared/vented gas, and number of wells in the Surat Basin (data from https://www.data.qld.gov.au/dataset/petroleum-gas-production-and-reserve-statistics[1]).

880 **7.5 Sensitivity to background methane**

Figure 4 shows that there is a slight difference in the estimated background CH_4 levels between the two monitoring locations, with the Ironbark background methane larger by 1 ppb on average than Burncluith and the standard deviation of the background differences being 1.4 ppb, the latter is comparable to the background concentration uncertainty (= 3.5 ppb) considered in the inversion.

885 We conducted an inverse modelling sensitivity test with the same model setup as that for Figure 13c (Case 3c, with the bottom-up inventory as a Gaussian prior with $\sigma_p = 3\%\ q_p$), except that instead of using the background times series that was averaged over the two sites we used the respective background timeseries for these sites. The results were virtually the same compared to Figure 13c, other than some insignificant changes in areas with low emissions. Table 2 gives the annual inferred emissions, which show no sensitivity.

890 Our background concentration calculation methodology (Supplement S3) assumes that under very vigorous atmospheric mixing conditions in the daytime, the measured concentrations within study domain represent methane levels both within and outside the domain boundaries, so that the measured concentrations can be taken to represent the background under such conditions. Because the background concentration is calculated from the measurements within the source region under study,

[1] This data file places the gas fields of Spring Gully and Peat within the Bowen Basin whereas in our bottom-inventory these are part of the Surat Basin. This is because of how the gas field zones and basin boundaries are defined. The gas fields included in our study are based on their geographic locations relative to the square study domain selected. Adding these two gas fields to the Surat Basin does not change the trends shown in Figure 19.

there is a possibility that the real background is potentially lower than what we have used. To examine this, another inversion sensitivity test was conducted by using an alternate methane background (with all other settings the same as the final Case 3c) and this is described in detail in the Supplement S5. The alternate background was constructed using the averaged background from the two sites and the marine baseline methane measurements from the Cape Grim Baseline Air Pollution Station (https://capegrim.csiro.au), located on the north-west tip of Tasmania (40.7ºS, 144.7ºE). The marine baseline methane represents concentration levels without the direct influence of the continental sources. The alternate background falls between the average Surat background as used in the paper and the Cape Grim baseline and is, on average, lower than the Surat background by 2.8 ppb.

The inversion results in Table 2 show that compared to the inferred emissions obtained using the original background methane the alternate background gives total emissions that are 6.8% higher, whereas the increase is the smallest at 3.9% in the CSG subdomain, and is largest at 8.5% in the non-CSG region. Overall, this increase is expected because the increase in the concentration signal by 2.8 ppb as a result of the use of the alternate background (which is 2.8 ppb lower than the original background) needs to be to accounted for by the inversion by increasing the amount of inferred emissions. We also find that the amount of increase in the inferred emissions with the alternate background is almost uniformly spread through the study domain, and there are no significant spatial distributional shifts in the inferred emissions with the two background choices. This means that if these emissions are used in a forward model simulation, they would lift the modelled concentrations throughout the region by a very similar amount (probably by 2.8 ppb).

Table 2: Inferred emissions ($\times 10^6$ kg yr^{-1}) obtained using: the methane background averaged over the two sites (as used in the paper, Case 3c), the individual methane background from the two sites, and the alternate methane background calculated using the Cape Grim baseline methane data (see Supplement S5). The values in the parentheses are % change over the inferred emissions using the averaged background. The bottom-up inventory emissions are also included for comparison.

Methane background	Total	CSG subdomain	Non-CSG subdomain
Average background (as used in this paper)	165.8	63.6	102.2
Separate backgrounds from the two sites	164.8 (-0.6%)	62.7 (-1.4%)	102.1 (-0.1%)
Alternate background (see Supplement S5)	177.0 (+6.8%)	66.1 (+3.9%)	110.9 (+8.5%)
Bottom-up inventory	173.2	47.7	125.5

8 Conclusions

This paper presenteds both top-down and bottom-up quantification of gridded methane emissions from the CSG producing Surat Basin, an area of 350 × 350 km^2 in Queensland, Australia. The 2015 bottom-up methane emission inventory served as a very useful prior in our regional top-down methodology based on a Bayesian inference approach that utilised hourly-mean CH_4 concentrations monitored at the Ironbark and Burncluith stations for 1.5 years, hourly source-receptor relationship, and an MCMC technique for posterior PDF sampling.

The largest contribution to the emissions in the bottom-up methane inventory is from grazing cattle (~50%), cattle feedlots (~25%), and CSG processing (~8%), with the aggregate emissions in the study area being approximately 173.2 × 10^6 kg CH_4 yr^{-1}. Although the forward transport modelling with the bottom-up emissions yielded a credible simulation of the suitably filtered observed methane concentrations, about 15% of the higher-end concentration observations were underestimated.

The top-down Bayesian inverse approach demonstrated that even when we do not specify an informative prior, the source signal inherent in the methane observations from only two sites constrains the total emission well. But, in contrast to the inventory emissions, the inferred emissions are more intensely located in the centre of the study region and less in regions that are farther. The importance of specifying a suitable prior in the Bayesian inference was apparent, with the bottom-up inventory proving very valuable for that purpose. Particularly, a Gaussian prior having mean values taken the same as the bottom-up emissions with an uncertainty equal to 3% of the mean yielded the best emission distribution, as evident from its performance in faithfully reproducing the measured methane concentration timeseries. This inverse setup yielded a domain-wide emission of 165.8 × 10^6 kg CH_4 yr^{-1} which is very slightly less than the one obtained from the bottom-up inventory. However, within a subdomain covering all the CSG source areas, the inferred emissions 63.6 × 10^6 kg CH_4 yr^{-1} are is 33% larger than thatose deduced from the bottom-up inventory. The dominant localised inventory emissions in this area are from CSG, followed by feedlots. Since feedlots are scattered throughout the domain including the non-CSG areas from where there is no inference of higher emissions, it is plausible that the increase in the inferred emissions would mainly correspond to CSG as the source sector.

The source-receptor relationship showed that having only two monitoring stations is inadequate for sampling distant source areas within the large study domain, especially areas in the south-east and north-west corners (the network design for the two monitoring stations mainly focused on the central CSG regions). Lengthening the measurement period to sample these areas better would not have helped because the wind climatology of the area is not likely to change considerably. When source areas are not sampled well, one may impose stricter priors that are more credible than the inferred emissions, or alternatively increase the number of stations. The former strategy is probably reflected in our use of a small uncertainty in the prior (i.e. 3% of the mean) for the best inversion case. A smaller prior uncertainty pushes the inversion more towards the prior itself with distant source areas not sampled sufficiently by the network sites looking like the prior distribution. A larger prior uncertainty results in the inversion moving towards higher emissions for sources that are close to the monitoring stations.

The inverse methodology could not distinguish between different source categories, mainly because the concentration of methane alone was monitored and not tracers specific to methane source types. To do source discrimination and attribution, monitoring of tracer species such as methane isotopes ($^{13}CH_4$, CH_3D and $^{14}CH_4$), or other hydrocarbons in cases where they are associated with the source gas, would prove useful when suitable sampling systems or instrumentation for field deployment become available.

The methods developed in this study could be used to improve the monitoring and management of greenhouse gas and other air emissions from the onshore gas industry, including that in the Surat Basin. They provide independent information to industry and communities living in gas development regions on one of the main environmental impacts potentially arising from onshore gas developments. Improved quantification of methane emissions on the regional scale is an important step in emissions reductions from the onshore gas sector and possibly other industries. The present top-down method is particularly suited to distributed emissions with potentially unknown locations across a large geological gas reservoir and gas production infrastructure. If monitoring is deployed before gas exploration and production begins then a baseline would be established from which emissions from the industry might be detected. Ongoing top-down quantification, with monitoring stations located close to where emissions appear and with source-specific information from tracers could provide the information necessary to validate emissions from the gas industry to support greenhouse gas inventories.

Data availability

The data and model output included in this paper can be made available by contacting the corresponding author (Ashok Luhar: ashok.luhar@csiro.au).

Author contributions

AKL performed the model development and application, analysed model output and data, and wrote the paper with contributions and comments from the co-authors. DME conducted the field study design, in-situ monitoring and data analysis, and GISERA project management. ZML conducted the in-situ monitoring, data collection, and data analysis. JN contributed to data processing. DS assisted with the monitoring sites, instrumentation and data collection. LS developed the bottom-up inventory. CO provided general information on methane sources.

Competing interests

The authors declare that they have no conflict of interest.

Acknowledgments

This work was partially supported by CSIRO's Gas Industry Social and Environmental Research Alliance (GISERA) (https://gisera.csiro.au) and Active Integrated Matter (AIM) Future Science Platform (FSP) (https://research.csiro.au/aim). Mark Kitchen and Steve Zegelin provided valuable instrumental and technical support. The authors thank Peter Rayner, Martin Cope and Dimitri Lafleur for their helpful comments on this work, and Natalie Shaw for her assistance with the preparation of the bottom-up inventory for the Surat Basin. Damian Barrett advised on this work, and Stuart Day furnished insights into local source monitoring. Useful comments by the two anonymous referees and Bryce Kelly are much appreciated. NCEP Reanalysis data provided by the NOAA/OAR/ESRL PSL, Boulder, Colorado, USA, from their Web site at https://psl.noaa.gov.

References

Alvarez, R. A., Zavala-Araiza, D., Lyon, D. R., Allen, D. T., Barkley, Z. R., Brandt, A. R., et al.: Assessment of methane emissions from the U.S. oil and gas supply chain, Science, 361(6398), 186–188, https://doi.org/10.1126/science.aar7204, 2018.

Brandt, A. R., Heath, G. A., Kort, E. A., O'Sullivan, F., Pétron, G., Jordaan, S.M., et al.: Methane leaks from North American natural gas systems, Science, 343(6172), 733–735, https://doi.org/10.1126/science.1247045, 2014.

Cheng, M.-D., Hopke, P. K., and Zeng, Y.: A receptor-oriented methodology for determining source regions of particulate sulfate at Dorset, Ontario, Journal of Geophysical Research, 98(D9), 16,839–16,849, https://doi.org/10.1029/92JD02622, 1993.

Cui, Y. Y., Brioude, J., Angevine, W.M., Peischl, J., McKeen, S. A., Kim, S.-W., et al.: Top-down estimate of methane emissions in California using a mesoscale inverse modeling technique: The San Joaquin Valley, Journal of Geophysical Research, 122(6), 3686–3699, https://doi.org/10.1002/2016JD026398, 2017.

Day, S., Dell'Amico, M., Etheridge, D., Ong, C., Rodger, A., Sherman, B., and Barrett, D.: Characterisation of regional fluxes of methane in the Surat Basin, Queensland. Phase 1: A review and analysis of literature on methane detection and flux determination. CSIRO Australia report, 2013.

Day, S., Ong, C., Rodger, A., Etheridge, D., Hibberd, M., van Gorsel, E., et al.: Characterisation of regional fluxes of methane in the Surat Basin, Queensland: Phase 2: A pilot study of methodology to detect and quantify methane sources, CSIRO Australia report EP15369, 2015.

DNRM: Queensland's Petroleum and Coal Seam Gas 2015–16, Department of Natural Resources and Mines, Queensland Government, Australia, 8 pp., http://www.australiaminerals.gov.au/__data/assets/pdf_file/0003/47622/Queenslands-petroleum-and-coal-seam-gas-2017.pdf, 2017.

Etheridge, D., Loh, Z., Schroder, I., Berko, H., Kuske, T., Allison, C., et al.: Metadata report: Arcturus atmospheric greenhouse gas monitoring. Record 2014/37, Geoscience Australia, Canberra, 2014.

Etheridge, D. M., Day, S., Hibberd, M. F., Luhar, A., Spencer, D. A., Loh, Z. M., et al.: Characterisation of regional fluxes of methane in the Surat Basin, Queensland: The continuous monitoring results – installation, commissioning and operation of two field stations and preliminary data, Milestone 3.1 GISERA Greenhouse Gas Research – Phase 3, CSIRO Australia report, 2016.

Etiope, G, Ciotoli, G, Schwietzke, S and Schoell, M.: Gridded maps of geological methane emissions and their isotopic signature, Earth Syst Sci Data, 11, 1–22, doi: 10.5194/essd-11-1-2019, 2019.

Etiope, G. and Schwietzke, S.: Global geological methane emissions: an update of top-down and bottom-up estimates, Elem Sci Anth, 7(1), p. 47, http://doi.org/10.1525/elementa.383, 2019.

Feitz, A., Schroder, I., Phillips, F., Coates, T., Neghandhi, K., Day, S., et al.: The Ginninderra CH_4 and CO_2 release experiment: An evaluation of gas detection and quantification techniques, International Journal of Greenhouse Gas Control, 70, 202–224, https://doi.org/10.1016/j.ijggc.2017.11.018, 2018.

Harper, L. A, Denmead, O. T., Freney, J. R, and Byers, F. M.: Direct measurements of methane emissions from grazing and feedlot cattle, Journal of Animal Science, 77, 1392–1401, https://doi.org/10.2527/1999.7761392x, 1999.

Henne, S., Brunner, D., Oney, B., Leuenberger, M., Eugster, W., Bamberger, I., et al.: Validation of the Swiss methane emission inventory by atmospheric observations and inverse modelling, Atmospheric Chemistry and Physics, 16(6), 3683–3710, https://doi.org/10.5194/acp-16-3683-2016, 2016.

Hmiel, B., Petrenko, V. V., Dyonisius, M. N. et al.: Preindustrial $^{14}CH_4$ indicates greater anthropogenic fossil CH_4 emissions, Nature 578, 409–412, https://doi.org/10.1038/s41586-020-1991-8, 2020.

Hourdin, F. and Talagrand, O.: Eulerian backtracking of atmospheric tracers. I: Adjoint derivation and parametrization of subgrid-scale transport, Quarterly Journal of the Royal Meteorological Society, 132(615), 567–583, https://doi.org/10.1256/qj.03.198.A, 2006.

Hurley, P.: TAPM V4. Part 1: Technical Description. CSIRO Marine and Atmospheric Research Paper No. 25, Australia, p. 59. Available at: http://www.cmar.csiro.au/research/tapm/docs/tapm_v4_technical_paper_part1.pdf, 2008.

Hurley, P. J. and Luhar, A. K.: Modelling the meteorology at the Cabauw tower for 2005, Boundary-Layer Meteorology, 132(1), 43–57, https://doi.org/10.1007/s10546-009-9384-4, 2009.

Hurley, P. J., Physick, W. L., and Luhar, A. K.: TAPM: a practical approach to prognostic meteorological and air pollution modelling, Environmental Modelling and Software, 20(6), 737–752, https://doi.org/10.1016/j.envsoft.2004.04.006, 2005.

IPCC~~, 2014~~: Climate Change 2014: Synthesis Report. Contribution of Working Groups I, II and III to the Fifth Assessment Report of the Intergovernmental Panel on Climate Change [Core Writing Team, R.K. Pachauri and L.A. Meyer (eds.)]. IPCC, Geneva, Switzerland, 151 pp. http://www.ipcc.ch/pdf/assessment-report/ar5/syr/SYR_AR5_FINAL_full.pdf~~.~~, 2014.

IPCC: 2019 Refinement to the 2006 IPCC Guidelines for National Greenhouse Gas Inventories (Calvo Buendia, E., Tanabe, K., Kranjc, A., Baasansuren, J., Fukuda, M., Ngarize, S., Osako, A., Pyrozhenko, Y., Shermanau, P. and Federici, S. (eds.)), Volume 4: Agriculture, Forestry and Other Land Use: Chapter 10: Emissions from Livestock and Manure Management, Published: IPCC, Switzerland, 2019.

~~IPCC: Climate Change: The Physical Science Basis, Contribution of Working Group I to the Fifth Assessment Report of the Intergovernmental Panel on Climate Change, edited by: Stocker, T. F., Qin, D., Plattner, G. K., Tignor, M., Allen, S. K., Boschung, J., Nauels, A., Xia, Y., Bex, V., and Midgley, P. M., Cambridge University Press, Cambridge, United Kingdom and New York, NY, USA, 1535 pp., 2013.~~

Iverach, C. P., Cendon, D. I., Hankin, S. I., Lowry, D., Fisher, R. E., France, J. L., Nisbet, E.G, Baker, A., and Kelly, B. F. J.: Assessing connectivity between an overlying aquifer and a coal seam gas resource using methane isotopes, dissolved organic carbon and tritium, Scientific Reports, 5, 15996, https://doi.org/10.1038/srep15996, 2015.

Jaynes, E. T.: Probability theory: The logic of science, Cambridge University Press, Cambridge, UK, 753 pp., 2003.

Jeong, S., Zhao, C. Andrews, A. E., Bianco, L., Wilczak, J. M., and Fischer, M. L.: Seasonal variation of CH_4 emissions from central California, Journal of Geophysical Research, 117, D11306, https://doi.org/10.1029/2011JD016896, 2012.

Kalnay, E., Kanamitsu, M., Kistler, R., Collins, W., Deaven, D., et al.: The NCEP/NCAR 40-year reanalysis project, Bull. Amer. Meteor. Soc., 77, 437–472, https://doi.org/10.1175/1520-0477(1996)077<0437:TNYRP>2.0.CO;2, 1996.

Luhar, A. K. and Hurley, P.: Evaluation of TAPM, a prognostic meteorological and air pollution model, using urban and rural point source data, Atmospheric Environment, 37(20), 2795–2810, https://doi.org/10.1016/S1352-2310(03)00204-8, 2003.

Luhar, A. K., Mitchell, R. M., Meyer, C. P., Qin, Y., Campbell, S., Gras, J. L., and Parry, D.: Biomass burning emissions over northern Australia constrained by aerosol measurements: II–Model validation, and impacts on air quality and radiative forcing, Atmospheric Environment, 42(7), 1647–1664, https://doi.org/10.1016/j.atmosenv.2007.12.040, 2008.

Luhar, A. K., and Hurley, P. J.: Application of a coupled prognostic model to turbulence and dispersion in light-wind stable conditions, with an analytical correction to vertically resolve concentrations near the surface, Atmospheric Environment, 51, 56–66, https://doi.org/10.1016/j.atmosenv.2012.01.046, 2012.

Luhar, A. K., Etheridge, D. M., Leuning, R., Loh, Z. M., Jenkins, C. R., and Yee, E.: Locating and quantifying greenhouse gas emissions at a geological CO_2 storage site using atmospheric modeling and measurements, Journal of Geophysical Research: Atmospheres, 119(18), 10959–10979, https://doi.org/10.1002/2014JD021880, 2014.

Luhar, A. K., Thatcher, M., and Hurley, P. J.: Evaluating a building-averaged urban surface scheme in an operational mesoscale model for flow and dispersion, Atmos. Environ., 88, 47–58, http://dx.doi.org/10.1016/j.atmosenv.2014.01.059, 2014.

Luhar, A. K., Emmerson, K. M., Reisen, F., Williamson, G. J., and Cope, M. E.: Modelling smoke distribution in the vicinity of a large and prolonged fire from an open-cut coal mine. Atmos Environ., 229, 117471, https://doi.org/10.1016/j.atmosenv.2020.117471, 2020.

Marchuk, G. I.: Adjoint equations and analysis of complex systems. Dordrecht, Netherlands: Springer Science. pp. 466, 1995.

Matthaios, V. N., Triantafyllou, A. G., and Koutrakis, P.: PM_{10} episodes in Greece: Local sources versus long-range transport—observations and model simulations. Journal of the Air and Waste Management Association, 67(1), 105–126, https://doi.org/10.1080/10962247.2016.1231146, 2017.

Miller, S. M., Michalak, A. M., and Levi, P. J.: Atmospheric inverse modeling with known physical bounds: an example from trace gas emissions, Geoscientific Model Development, *7*(1), 303–315, https://doi.org/10.5194/gmd-7-303-2014, 2014.

NIR: National Inventory Report 2015 Volume 1, Commonwealth of Australia, https://www.industry.gov.au/sites/default/files/2020-07/national-inventory-report-2015-volume-1.pdf, 2017.

Pudykiewicz, J. A.: Application of adjoint tracer transport equations for evaluating source parameters, Atmospheric Environment, 32(17), 3039–3050, https://doi.org/10.1016/S1352-2310(97)00480-9, 1998.

Rao, K. S.: Source estimation methods for atmospheric dispersion, Atmospheric Environment, 41(33), 6964–6973, https://doi.org/10.1016/j.atmosenv.2007.04.064, 2007.

Saunois, M., Stavert, A. R., Poulter, B., Bousquet, P., Canadell, J. G., Jackson, R. B., et al.: The global methane budget 2000–2017~~2~~, Earth System Science Data, 12, 1561–1623, https://doi.org/10.5194/essd-12-1561-2020, 2020~~16~~.

Schneising, O., Burrows, J. P., Dickerson, R. R., Buchwitz, M., Reuter, M., and Bovensmann, H.: Remote sensing of fugitive methane emissions from oil and gas production in North American tight geologic formations, Earth's Future, *2*, 548–558, https://doi.org/10.1002/2014EF000265, 2014.

Singh, S. K., Sharan, M., and Issartel, J.-P.: Inverse modelling methods for identifying unknown releases in emergency scenarios: an overview, Int. J. Environment and Pollution, 57(1/2), 68–91, https://doi.org/10.1504/IJEP.2015.072121, 2015.

Tarantola, A.: Inverse problem theory and methods for model parameter estimation. Society for Industrial and Applied Mathematics, Philadelphia, 342 p., 2005.

Towler, B., Firouzi, M., Underschultz, J., Rifkin, W., Garnett, A., Schultz, H., et al.: An overview of the coal seam gas developments in Queensland, Journal of Natural Gas Science and Engineering, 31, 249–271, https://doi.org/10.1016/j.jngse.2016.02.040, 2016.

Venkatram, A., Brode, R., Cimorelli, A., Lee, R., Paine, R., Perry, S., et al.: A complex terrain dispersion model for regulatory applications, Atmospheric Environment, 35~~(24)~~, 4211–4221, https://doi.org/10.1016/S1352-2310(01)00186-8, 2001.

Wang, Y. P., and S. T. Bentley, S. T.: Development of a spatially explicit inventory of methane emissions from Australia and its verification using atmospheric concentration data, Atmospheric Environment, 36, 4965–4975, https://doi.org/10.1016/S1352-2310(02)00589-7, 2002.

WMO: WMO Greenhouse Gas Bulletin, No. 14, 22 November 2018, https://library.wmo.int/doc_num.php?explnum_id=5455, ISSN 2078-0796, 2018.

Yee, E., Lien, F.-S., Keats, A., and D'Amours, R.: Bayesian inversion of concentration data: Source reconstruction in the adjoint representation of atmospheric diffusion, Journal of Wind Engineering and Industrial Aerodynamics, 96(10-11), 1805–1816, https://doi.org/10.1016/j.jweia.2008.02.024, 2008.

Yee, E. and Flesch, T. K.: Inference of emission rates from multiple sources using Bayesian probability theory, Journal of Environmental Monitoring, 12, 622–634, https://doi.org/10.1039/B916954G, 2010.

Yee, E.: Inverse dispersion for an unknown number of sources: Model selection and uncertainty analysis, ISRN Applied Mathematics, Article ID 465320, 20 pp., 2012.

Quantifying methane emissions from Queensland's coal seam gas producing Surat Basin using inventory data and a regional Bayesian inversion

Ashok K. Luhar[1], David M. Etheridge[1], Zoë M. Loh[1], Julie Noonan[1], Darren Spencer[1], Lisa Smith[2], and Cindy Ong[3]

[1]CSIRO Oceans and Atmosphere, Aspendale, Victoria 3195, Australia
[2]Katestone Environmental Pty. Ltd., Milton, QLD 4064, Australia
[3]CSIRO Energy, Kensington, WA 6152, Australia

Correspondence to: Ashok Luhar (Ashok.Luhar@csiro.au)

Abstract. Methane (CH_4) is a potent greenhouse gas and a key precursor of tropospheric ozone, itself a powerful greenhouse gas and air pollutant. Methane emissions across Queensland's Surat Basin, Australia, result from a mix of activities, including the production and processing of coal seam gas (CSG). We measured methane concentrations over 1.5 years from two monitoring stations established 80 km apart on either side of the main CSG belt located within a study area of 350 × 350 km^2. Using an inverse ~~Coupling bottom-up inventory and inverse~~ modelling approach~~es~~ coupled with a bottom-up inventory, we quantify methane emissions from this area. The inventory suggests that the total emission is 173.2 × 10^6 kg CH_4 yr^{-1}, with grazing cattle contributing about half of that, cattle feedlots ~ 25%, and CSG Processing ~ 8%. Using the inventory emissions in a forward regional transport model indicates that the above sources are significant contributors to methane at both monitors. However, the model underestimates approximately the highest 15% of the observed methane concentrations, suggesting underestimated or missing emissions. An efficient regional Bayesian inverse model is developed, incorporating an hourly source-receptor relationship based on a backward-in-time configuration of the forward regional transport model, a posterior sampling scheme, and the hourly methane observations and a derived methane background. The inferred emissions obtained from one of the inverse model setups that uses a Gaussian prior whose averages are identical to the gridded bottom-up inventory emissions across the domain with an uncertainty of 3% of the averages best describes the observed methane. Having only two stations is not adequate at sampling distant source areas of the study domain, and this necessitates a small prior uncertainty. This inverse setup yields a total emission of 165.8 × 10^6 kg CH_4 yr^{-1}, slightly smaller than the inventory total. However, in a subdomain covering the CSG development areas, the inferred emissions are 63.6 × 10^6 kg CH_4 yr^{-1}, 33% larger than those from the inventory. We also infer seasonal variation of methane emissions and examine its correlation with climatological rainfall in the area.~~within the full study domain, and CSG and non-CSG subdomains.~~

1 Introduction

Methane (CH_4) is a potent greenhouse gas with a global warming potential 84 times greater than carbon dioxide (CO_2) over a 20-year period and 28 times greater over a 100-year period (IPCC, 2014). It is emitted by both anthropogenic activities (e.g. ~~such as~~ coal mining and the raising of cattle) and natural sources (e.g. wetlands). In terms of anthropogenic radiative forcing, methane is the second most important greenhouse gas after CO_2. Globally averaged surface CH_4 concentrations have increased by almost 160% since pre-industrial times, from ~~a level of~~ 7312~~2~~ ppb (by volume) in 1750 to 1859 ppb in 2018 (Meinshausen et al., 2017; WMO, 2018; Rubino et al., 2019), and this increase has been largely due to changes in anthropogenic methane (~~e.g.,~~ IPCC, 2014). Compared to CO_2, the atmospheric lifetime of methane is much shorter (~ 10 years), which means that near-term warming of the climate could diminish following mitigation actions that reduce methane emissions. Being chemically reactive, methane also plays an important role as a precursor to tropospheric ozone, itself a greenhouse gas and an air pollutant affecting human health and plant productivity. Thus, understanding and quantifying methane emissions at various scales is crucial to studying changes in atmospheric radiative forcing and air quality.

Globally, a top-down estimate over the period 2008~~0~~-2017 suggests that agriculture and waste contribute to about ~~5~~60% of the total anthropogenic methane emissions, followed by fossil fuel production and use (gas, oil, coal mining and industry) at 3~~1~~5% (Saunois et al., 2020). However, a study using measurements of carbon-14 in methane recently showed that nearly all methane from fossil sources is anthropogenic, contrasting with the bottom-up estimates of significant natural geologic seepage (Etiope et al., 2019; Etiope and Schwietze, 2019), and that fossil fuel methane emissions may be underestimated by up to 40% (Hmiel et al., 2020). Significant CH_4 emissions from conventional and unconventional gas fields have been reported in the scientific literature (e.g., Brandt et al., 2014; Schneising et al., 2014; Alvarez et al., 2018).

In the Australian state of Queensland, since the mid-2000s there has been a rapid growth of the production of coal seam gas (CSG), which is virtually pure methane (Towler et al., 2016; DNRM, 2017). CSG, also known as coalbed methane, is classed as an unconventional natural gas, typically extracted from coal seams at depths of 200–1000 m. As of 2015-16, 96% of the gas production in Queensland was CSG, with most of it coming from the Surat Basin (78%, 21187 Mm^3) and the rest (18%, 4958 Mm^3) from the Bowen Basin (DNRM, 2017). With the sharp rise of CSG production, methane emissions from the Surat Basin are a focus of Australia's CSIRO Gas Industry Social and Environmental Research Alliance (GISERA) (https://gisera.csiro.au) research in Air Quality and Greenhouse Gas. The Surat Basin is predominantly rural, and methane sources other than CSG include agriculture and coal mining. CSG activities that lead to potential methane emissions include CSG wells, pumps, pipelines, vents, pneumatic controls, and produced water bodies (Day et al., 2013).

The objective of the present paper is to quantify methane emissions from a region of 350 × 350 km^2 of Queensland's side of the Surat Basin (Figure 1~~Figure 1~~, covering the area 148° 17' 43.4"–151° 49' 30.5" E, 25° 3' 48.8"–28° 5' 3.7" S) that encompasses the main CSG production and processing areas using a top-down approach~~technique~~ coupled with~~assisted by~~ a bottom-up emission inventory that serves as a prior. The latter involves deriving emissions through a compilation of sources

and activity data and application of emission factors. We conducted concurrent in-situ atmospheric monitoring of methane during July 2015 – December 2016 at two locations, namely Ironbark and Burncluith, 80 km from each other. The two stations were setup such that they were on either side of the broad present and projected CSG work area in the Surat Basin. The measured concentrations allow for an atmospherically based validation of the bottom-up inventory by using it in a forward mesoscale meteorological and transport model~~–~~, namely TAPM (see Section 4.1), and comparing the predicted methane concentrations with the measurements at the two sites.

~~The main focus in the paper is on the formulation of a~~An efficient top-down, or inverse, modelling methodology for regional scale (~ 100–1000 km) is formulated, and ~~its~~ appli~~ed~~cation to quantify CH_4 emissions in the Surat Basin. It combines a Bayesian inference approach, an hourly-averaged high-resolution backward-in-time construction of the forward ~~mesoscale meteorological and transport~~ model TAPM, and a posterior probability density function (PDF) sampling scheme. A method to correct for time-lag effects in the backward plume methodology is presented. The 1.5 years long hourly methane measurements from the two stations are combined in a Bayesian calculation to derive a top-down emission distribution. Methane background calculation and filtering methodologies are devised. Various Bayesian priors and their uncertainties, including the use of the bottom-up emissions to act as a prior, are tested. The inferred top-down CH_4 emissions are examined alongside the bottom-up inventory emissions for the whole study domain as well as subdomains containing the CSG and non-CSG activities. We also compare the performance of the top-down ~~emissions~~ method by comparing the modelled methane concentrations obtained using the top-down derived emissions~~them~~ in forward modelling with the observed concentrations. To our knowledge, this study is the first in Australia to quantify regional scale CH_4 emissions through a top-down approach employing transport modelling and concentration measurements, although studies at other spatial scales with broadly similar approaches have been reported, e.g. by Luhar et al. (2014) and Feitz et al. (2018) for single point sources at local scale and by Wang and Bentley (2002) at continental scale with Australian methane emissions divided into eight source regions.

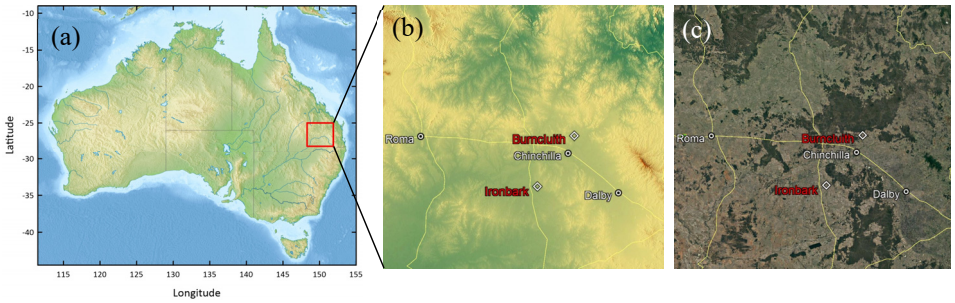

Figure 1. (a) Map of Australia, showing the 350 × 350 km² study domain (red square) of Queensland's part of the Surat Basin. The base relief map is from https://www.mapsland.com/oceania/australia/large-relief-map-of-australia (used under Creative Commons Attribution-ShareAlike 3.0 Licence); (b) orography of the study domain, with terrain elevation ranging approximately between 100 m (green) and 1140 m (red) above sea level; (c) a Google Earth map of the study domain showing the surface characteristics. The Ironbark and Burncluith monitoring sites, and the three biggest towns of Dalby, Roma and Chinchilla (population ~ 12700, 6850 and 6600, respectively) in the area are also shown in (b) and (c).

2 Monitoring and data filtering

We set up two monitoring stations, namely Ironbark (150° 14' 37.6" E, 27° 8' 6.6" S; 226.806 km east, 6995.596 km north MGA (Map Grid Australia), Zone 56) and Burncluith (150° 42' 5.4" E, 26° 34' 2.4" S; 271.051 km east, 7059.430 km north MGA, Zone 56), located about 80 km apart on two sides of the main coal seam gas belt of the Surat Basin (Figure 1~~Figure 1~~b,c). The selection of the site locations was largely based on a meteorological and dispersion modelling study (Day et al., 2015; Etheridge et al., 2016) that suggested that with the prevailing winds from the north-east and south-west quadrants, long-term continuous monitoring of greenhouse gas concentrations at these two locations would optimise the size and frequency of detection of methane emissions from the broader CSG source region without being unduly impacted by individual sources in the proximity of the measurement sites. There were other practical considerations, namely access, power, security, landowner assistance and possible future developments that would impact the site.

Continuous high frequency (~ 0.3 Hz) measurements of the concentrations of CH_4, CO_2 and water vapour (and also carbon monoxide (CO) at Burncluith) were made at the two sites for about three years with an overlapping period of 1.5 years (July 2015 to December 2016) using Picarro cavity ring down spectrometers (model G2301 at Ironbark, and G2401 at Burncluith) with inlets placed on masts at a height of 10 m. The installations are described by Etheridge et al. (2016). Measured concentrations (strictly speaking, mole fractions in dry air, also volumetric mixing ratios) from each site can be exactly intercompared due to identical calibrations and measurement methodologies. The additional CO measurements at Burncluith are useful in detecting combustion sources of CO_2 and CH_4. Measurement accuracy was better than ± 0.1 ppm for CO_2 and ±

1 ppb for CH_4 (Etheridge et al., 2014). Concurrent meteorological observations included winds measured at 5.8 m ~~AGL (~~above ground level~~)~~ (AGL) at Ironbark and at 7.6 m AGL at Burncluith using sonic anemometers.

The Burncluith station was located on a private farm and there were 30–40 cattle in the adjoining paddocks ~~next to it~~. Occasionally, under suitable meteorological conditions with the cattle upwind of the inlet, the emissions from the local cattle caused one or many sharp peaks in the observed methane signal, typical of a nearby point source. We developed a method which removes these sharp, transient peaks but does not alter the underlying signals from the numerous, region-wide feedlots, grazing cattle or other sources. This filtering method is described in the Supplement S1.1 and, for consistency, was also applied to the data from Ironbark, although local cattle are less in number and further away at this site.

Frequently, high methane concentrations at the two sites were observed at night under light wind stable conditions, particularly at Burncluith. Despite being of much practical interest, however, light winds are difficult to represent in a mesoscale meteorological and transport model. The causes for that include inadequate physical understanding of light-wind processes, flow properties being very sensitive to local topography, and model resolution constraints (Luhar and Hurley, 2012). As a practical measure, we filtered out the nighttime sampling hours for light wind conditions, and this method is described in the Supplement S1.2.

Methane emissions due to biomass burning are not part of the bottom-up inventory that we consider in the present modelling due to their being sporadic and highly unpredictable. Enhanced levels of CH_4 and CO were detected at Burncluith ~~in the course of~~during forest fires in the northern sector of Burncluith and wood-heater operations from the property located in the proximity of the monitoring station. The observed CO was used to filter out these occasional biomass burning events from the measured concentration time series, an approach similar to that used by Jeong et al. (2012). Details of the CO filter are given in the Supplement S1.3.

The number of data hours after the filtering was 6432 for Ironbark and 4149 for Burncluith (cf. the original, valid number of data points of 10938 and 12660, respectively). Unless stated otherwise, the filtered CH_4 data were used for our analysis and modelling.

3 Bottom-up emission inventory

Activity data for the year 2015 were used to develop a bottom-up emission inventory for methane for the Surat Basin. The emission inventory covered a domain of 345 × 345 km^2 with a spatial resolution of 1 × 1 km^2. Standard methodologies were generally adopted with data from various State and Federal Government Departments (e.g. (National Pollutant Inventory (NPI), National Greenhouse and Energy Reporting (NGER), and National Resource Management (NRM)). The bottom-up inventory included the following fourteen emission sectors: (1) feedlots, (2) grazing cattle, (3) piggeries, (4) poultry farms, (5) power stations, (6) coal mining, (7) CSG processing, (8) CSG production, (9) domestic woodheating, (10) vehicular traffic, (11) land-fills, (12) sewage treatment plants, (13) river seepage, and (14) geological seepage. The first four can be grouped as agricultural

activities. The inventory excluded CH_4 emissions from burning of biomass, land clearing, termites, ground-water wells (that were registered), wetlands, or fuel consumption and any material handling related to mining activities. Additional details pertaining to the bottom-up inventory compilation are briefly given in the Supplement S2, with a full report (Katestone, 2018) given in the Supplement S65.

Figure 2~~Figure 2~~ presents the bottom-up inventory emissions attributed to the various sectors in the Surat Basin, with the total emissions being 173.2×10^6 kg CH_4 yr^{-1}. Grazing cattle has the largest contribution, followed by cattle feedlots and CSG processing. We use this emission inventory for our study duration, July 2015–December 2016, with the assumption that any emission changes from the year 2015 to 2016 were insignificant. It is also assumed that all emissions are invariant with time. Although diurnal and seasonal variations for some emissions, viz. wood-heating, traffic, and power plant, are available in the raw data used in the inventory, contributions from these emissions are amongst the smallest and, therefore, we averaged these emissions over the full year for the purpose of computational efficiency in the modelling conducted here.

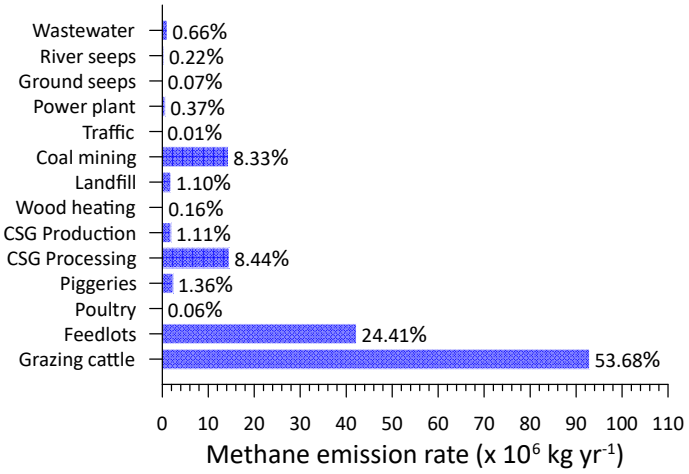

Figure 2. Bottom-up methane inventory emissions from the Surat Basin by sector/source; % of the total also shown. The total emission is 173.2×10^6 kg CH_4 yr^{-1}.

Figure 3~~Figure 3~~a presents the distribution of inventory methane emissions (kg yr^{-1} $gridcell^{-1}$) regridded at a ~~grid~~ resolution of 5×5 km^2 (69×69 grid points). There are localised sources as well as extensive, uniformly distributed source areas. The latter are emissions due to grazing cattle. These emissions are plotted in Figure 3~~Figure 3~~b in which four different coloured areas

are the so-called National Resource Management (NRM) regions. In each of these regions the available total number of grazing cattle was distributed uniformly, with the total number of grazing cattle in the study area being 1,086,059. There were 235 cattle feedlots and Figure 3~~Figure 3~~c shows the distribution of their emissions. These are localised, but distributed throughout the region, with some located between the two monitoring stations. Two mining source areas are also located between the two monitoring stations (Figure 3~~Figure 3~~d).

The CSG emissions are shown in Figure 3~~Figure 3~~e (processing) and Figure 3~~Figure 3~~f (production). The CSG production emissions are from wellhead (separators, wellhead control equipment, maintenance and leaks), combustion (flaring, well head pumps, backup generators, and diesel used by vehicles) and pipeline emissions (high point vents on produced water pipelines and pipeline control equipment) (Day et al., 2013). The CSG processing sources consist of processing facility emissions (control equipment, compressor venting, and gas conditioning units), combustion emissions (flaring, plant compressors, backup generators, and diesel used by vehicles), and collection and storage of water produced. Emissions from some of the CSG sources are continuous while others are intermittent (however, the inventory assumes all CSG emissions are time invariant). There were 5 CSG operators with 13 processing facilities and 4628 wells within the study domain. The well numbers included CSG producing (~ 85%) as well as exploration/appraisal/capped wells. Because of insufficient information, methane emissions from two of the five operators are not part of the inventory, but it was established that these two operators, with a total of 256 wells, only accounted for about 1.5% of the CSG activities that may be related to emissions. The biggest contributor to the total CSG methane emissions was venting (88%) from processing.~~,~~ Methane from produced water is a component of both CSG production and processing is an important source (~~e.g.~~ Iverach et al., 2015). It was included under venting~~I~~ and was~~is~~ calculated at 1.63×10^6 kg yr^{-1} (~10% of the total CSG emissions). Contribution from flaring was about 8%.

All major bottom-up emissions, namely from grazing cattle, feedlots, CSG processing and production, and coal mining, have potentially significant uncertainty, arising from uncertainty in both the activity data and emission factors, for example their potential temporal variation and how up to date they are with respect to the study period considered.

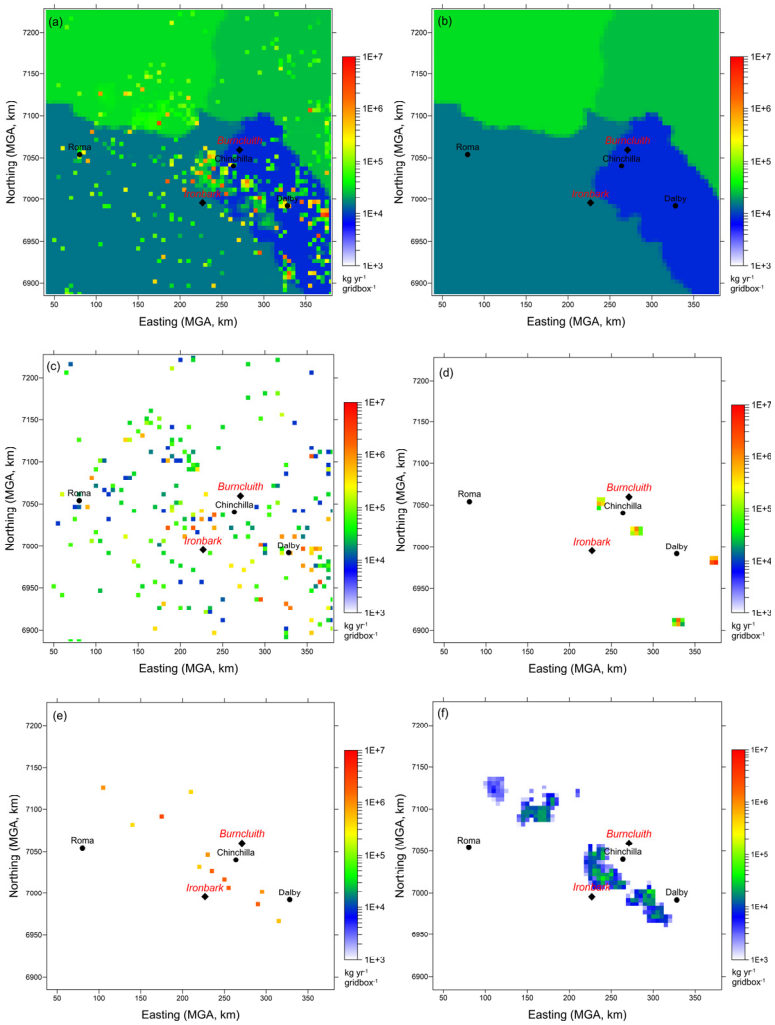

185 **Figure 3. Bottom-up methane inventory emissions from the Surat Basin (kg CH_4 yr^{-1} $gridbox^{-1}$, the grid-box size is 5 × 5 km^2). Also shown are the Ironbark and Burncluith monitoring sites, and the three biggest towns. (a) All emissions, and those due to (b) grazing cattle, (c) cattle feedlots, (d) coal mining, (e) CSG processing, and (f) CSG production.**

4 Modelling regional methane using the bottom-up emission inventory

We use the above inventory emissions in a (forward) regional meteorological and transport model and compare the modelled methane with the ambient measurements from the two sites.

4.1 Model and configuration

The prognostic~~, nestable,~~ mesoscale model used is The Air Pollution Model (TAPM vn4.0.5) developed by CSIRO, which has coupled meteorological and dispersion components and ~~which~~ is designed for applications ranging in scale from local to regional (~ < 1000 km) (Hurley et al., 2005; Hurley, 2008).

The meteorological component of TAPM predicts the local-scale flow against a background of larger-scale meteorology provided by the input synoptic-scale analyses (or forecasts). It solves momentum equations for horizontal wind components; the incompressible continuity equation for the vertical velocity in a terrain-following coordinate system; and scalar equations for potential virtual temperature, specific humidity of water vapour, cloud water/ice, rainwater and snow. Explicit cloud microphysical processes are included. Pressure is determined from the sum of hydrostatic and optional non-hydrostatic components, and a Poisson equation is solved for the non-hydrostatic component (not used here). Turbulence closure in the mean prognostic equations uses a gradient diffusion approach with non-local or counter-gradient corrections, which depends on eddy diffusivity (K) and gradients of mean variables and a mass-flux approach. The eddy diffusivity K is determined using prognostic equations for the turbulent kinetic energy (E) and its dissipation rate (ε). A vegetative canopy, soil scheme, and urban scheme are used at the surface, while radiative fluxes, both at the surface and at upper levels, are also included. Surface boundary conditions for the turbulent fluxes are determined using the Monin-Obukhov similarity theory and parameterisations for stomatal resistance.

The dispersion module makes use of the predicted finer-scale meteorology and turbulence fields from the meteorological ~~component, and~~component and comprises a default Eulerian grid-based conservation equation for species concentration (Hurley et al., 2005). The model has previously been applied to a variety of flow, turbulence and dispersion problems at various scales, such as those reported by Luhar and Hurley (2003), Luhar et al. (2008), Hurley and Luhar (2009), Luhar and Hurley (2012), Luhar et al. (2014), Matthaios et al. (2017), and Luhar et al. (2020), which include model evaluation studies.

TAPM can be used in a one-way nestable mode to improve efficiency and resolution. The global databases input to the model include land use, terrain height, leaf-area index, synoptic-scale meteorological reanalyses, and sea-surface temperature ~~(SST)~~.

We applied TAPM for the duration 1 July 2015 – 31 December 2016 with~~by using~~ two nested domains for both meteorology and dispersion: 370 × 370 km^2 with grid resolution 5 × 5 km^2 and 1110 × 1110 km^2 with grid resolution 15 × 15 km^2. Both domains had 75 × 75 grid points and were centred on (150°4.5' E, 26°35' S), which is equivalent to 208.657 km east and 7056.383 km north ~~in~~ MGA. There were 25 vertical levels, of which the lowest four were 10 m, 25 m, 50 m and 100 m AGL. The input synoptic-scale fields of the horizontal wind components, temperature and moisture required as boundary conditions

for the outermost model domain were sourced from the U.S. NCEP (National Centers for Environmental Prediction) reanalysis database given at a resolution of 2.5° latitude × 2.5° longitude at 6-hourly intervals (Kalnay et al., 1996; https://psl.noaa.gov/data/gridded/data.ncep.reanalysis.html). The model outputs hourly-averaged fields of meteorology and concentration.

The bottom-up inventory emissions lie within the inner model domain. In this model setup, each inventory emission grid cell (at 5 × 5 km^2) was considered as a surface~~an area~~ source, apart from the emissions from the power stations which were taken as point sources ~~together~~ with specification of their stack heights and plume-rise parameters. For computational efficiency, rather than considering all 14 emission categories plotted in Figure 2~~Figure 2~~ as separate sources, we aggregated them into 9 sectors with each sector taken as a tracer source: Grazing cattle (Source 1); Feedlots, Piggeries and Poultry (Source 2); CSG Processing (Source 3); CSG Production (Source 4); Mining (Source 5); River seeps (Source 6); Domestic wood heating, Wastewater treatment and Motor vehicles (Source 7); Ground seeps and Landfill (Source 8); and Power stations (Source 9). The relative emissions (%) of the above nine Sources are 53.8, 25.8, 8.4, 1.1, 8.3, 0.21, 0.82, 1.2 and 0.37%.

4.2 Estimation of background methane concentration

Since the simulated methane does not include the background levels that are representative of methane emissions located outside the bottom-up inventory, we devised a method for estimating hourly varying background CH_4 for each site involving concentrations under high atmospheric mixing conditions and the hourly standard deviation of concentration (see details in the Supplement S3). The estimated background concentration can be either added to the simulated methane or subtracted from the observed methane.

The estimated background methane concentration time series for Ironbark and Burncluith look very similar, and in Figure 4~~Figure 4~~ we present the average (green line) of the two background time series. The plot shows a marked seasonal variation in the background methane with a peak in September (early spring) and a minimum in February (late summer). To view the background variation with respect to the measured methane signal, we also present in Figure 4~~Figure 4~~ as dot points the unfiltered hourly mean observations (clipped at 2100 ppb) at Ironbark. The uncertainty (one standard deviation) in the background CH_4 is 3.6 ppb and 3.3 ppb for Ironbark and Burncluith, respectively. The difference between the estimated background at Ironbark and that at Burncluith (purple line in Figure 4~~Figure 4~~) is small and within ± 5 ppb. Any difference between the two backgrounds could be due to different sites in the study area getting impacted by different out-of-domain emissions depending on the transport meteorology. On average, the background concentration at Ironbark is greater by 1 ppb, and the standard deviation of the difference is 1.4 ppb. The average of the two background time series is taken to represent the regional hourly background CH_4 concentration, with an average uncertainty of 3.5 ppb. Sensitivity of the inferred emissions to other choices of the background concentration is examined in Section 7.4.

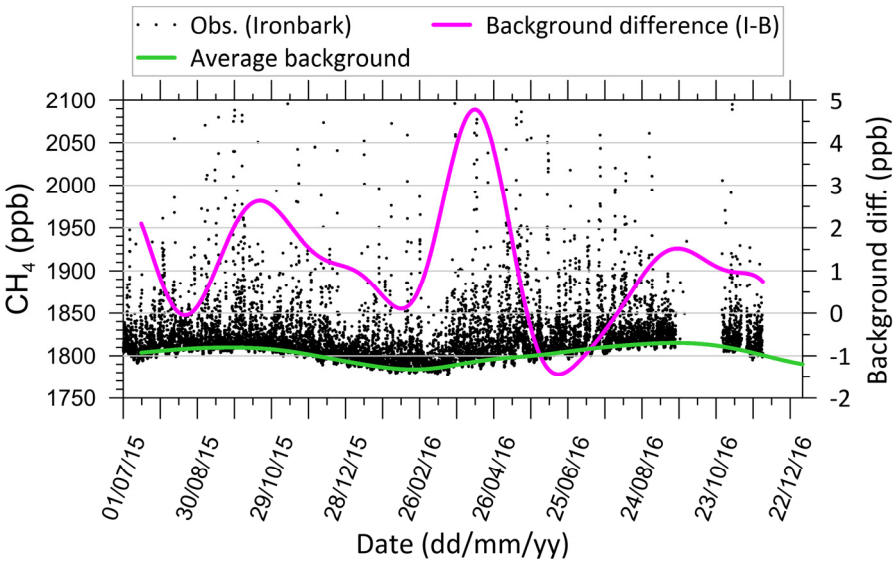

Figure 4. Estimated average hourly-averaged background CH_4 concentration time series (green line), and the difference between the estimated backgrounds between Ironbark and Burncluith (purple line). The data points are the hourly mean measurements at Ironbark without any filtering (clipped at 2100 ppb to make the background concentration variation stand out better).

4.3 Model performance for meteorology

Accurate modelling of the flow field over our region of interest is important as it controls the atmospheric plume transport and dispersion which in turn influences the accuracy of prediction of CH_4, and conversely the accuracy of inferred emissions. The hourly-averaged predicted winds extracted from the model output for the inner nest at the lowest model vertical level (10 m) at the grid point nearest to each of the two monitoring stations were compared with the observations from the two stations for the duration of the simulation~~, with the missing data hours not considered~~. The details of the model performance for meteorology is given in the Supplement S4. At both sites, the measured winds were most frequent from the north-east sector, with those at Burncluith being generally weaker in strength than those at Ironbark. As judged from the correlation coefficient (r) and index of agreement (IOA) values, the performance of TAPM for wind speed and wind direction was comparable to that obtained in other TAPM modelling studies (see the Supplement S4).

4.4 Modelled methane compared to observations

The monitoring sites were selected to avoid potential large, sustained methane sources within 10-20 km or even small sources within about a kilometre of the measurement inlet. Small sources that were closer to the inlets (mainly Burncluith) were identified and their signals filtered from the data as described in Section 2. As a result, we expect that the hourly-averaged filtered data are as representative as possible of the atmospheric methane concentration across the 5 × 5 km model grid cell containing the observation site, and can be directly compared to the model simulations.

The hourly-averaged modelled methane concentrations on the innermost grid domain were extracted at the lowest model level at the grid point nearest to each of the monitoring sites for comparison with the observations. The hourly-averaged concentrations simulated for the individual 9 source categories were aggregated and added to the estimated background concentration to compare with the observed, filtered CH_4 concentrations.

The scatter plots in Figure 5~~Figure 5~~ comparing the modelled and observed CH_4 at the two sites display a substantial degree of scatter, which is not unusual for atmospheric transport and diffusion models driven by predicted meteorology and using hourly-averaged concentrations paired in both time and space (e.g. Luhar et al., 2008). While the correlation coefficient values of 0.57 and 0.74 for Ironbark and Burncluith, respectively, imply a reasonable model prediction (see Table 1~~Table 1~~ for additional model performance statistics for the inventory emissions), it is clear that the modelled levels are generally lower than the observations, particularly the higher-end concentrations at Ironbark.

There could be various reasons for the differences between the modelled and observed methane, including uncertainty associated with the bottom-up emission inventory, its potential temporal variation, sources missing from the emission inventory, potential changes to the 2015 bottom-up inventory used here in the year 2016 (see Section 7.4), and the general modelling uncertainty, including that related to representing point measurements by grid-cell averaged model values.

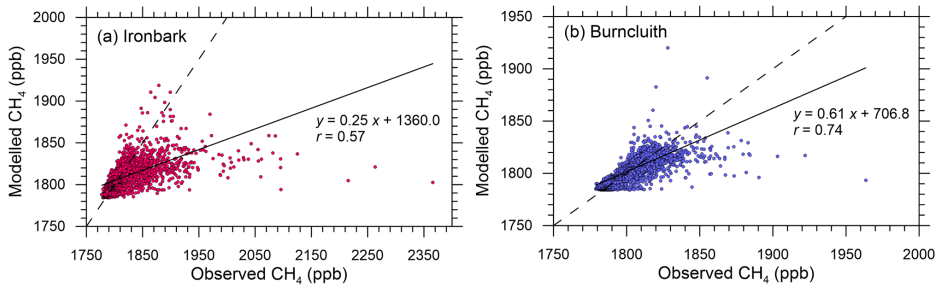

Figure 5. Hourly-averaged observed methane plotted against the simulated methane for the two monitoring stations. The solid line is the least-squares fit, and the dashed line is the 1:1 line (i.e. perfect agreement).

The comparison in Figure 5~~Figure 5~~ involving hourly methane paired in time and space enables a simple, yet stringent, validation check of a transport model, especially one that is driven by turbulent flow fields predicted by a prognostic meteorological model instead of observations. A complementary but less stringent approach in validating air quality models is the quantile-quantile (q-q) plot, which is a graphical technique for testing "goodness of fit" between two distributions. In such a plot, typically, sorted modelled concentrations are plotted against sorted observed values (i.e. unpaired in time) at a monitoring location (e.g., Venkatram et al., 2001; Luhar and Hurley, 2003; http://www.itl.nist.gov/div898/handbook/eda/section3/qqplot.htm). If the two sets come from a population with the same distribution, the data points should fall approximately along the 1:1 line. The principal advantage of a q-q plot is that a "good fit" is easy to recognize, and various distributional aspects, such as shape, tail behaviour and outliers, can be simultaneously examined.

In the q-q plot in Figure 6~~Figure 6~~ for Ironbark, the observed CH_4 distribution is modelled well for measurements < 1820 ppb, but for higher observed concentrations, which account for approximately 25% of the sample size, the modelled values are smaller. For Burncluith, the q-q plot shows a substantially better model performance, with the model underestimation of higher-end (> 1820 ppb) methane observations, which is approximately 10% of the sample size, much reduced compared to Ironbark. Overall, TAPM is largely predicting the observed CH_4 distribution correctly, except for a relatively few higher-end concentrations.

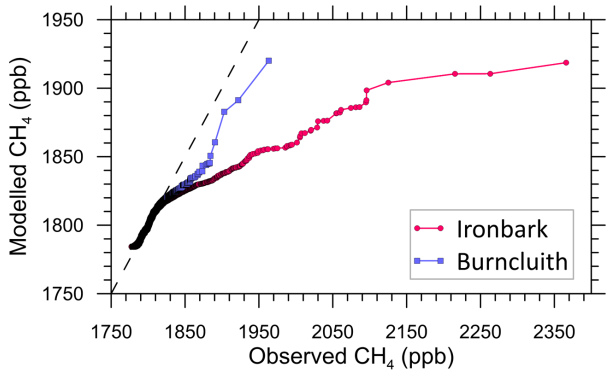

Figure 6. Q-q plot showing the sorted hourly-averaged observed CH_4 concentrations versus the sorted modelled ones at Ironbark and Burncluith. The line of perfect agreement (dashed line) is also shown.

4.5 Contribution to the modelled methane by various source categories

The top four source categories based on their contribution to the modelled CH_4 averaged over the full study period at Ironbark were Source 1 (45%, Grazing cattle), Source 2 (25%, Feedlots, Piggeries and Poultry), Source 3 (19%, CSG Processing), and Source 5 (5.5%, Mining). These were the same at Burncluith, but with their respective contributions being 69%, 17%, 6.4% and 4.1%. The CSG Production (Source 4) contributions are 2.2% and 0.73%, respectively, at the two sites.

In contrast, the largest four contributors to the highest 5% of the modelled hourly-averaged methane concentrations (i.e. all the concentrations above the 95th percentile) at Ironbark turn out to be Source 3 (35%), Source 2 (27%), Source 1 (25%) and Source 5 (7%). These at Burncluith are Source 1 (28%), Source 2 (25%), Source 3 (22%) and Source 5 (13%). The CSG Production (Source 4) contributes 3.8% and 2.5%, respectively, at the two sites. The Source 2 grouping is dominated by Feedlots.

The CSG Processing (Source 3) emissions are localised near the two sites which result in methane spikes under favourable winds and thus contribute more to the higher-end modelled methane than to the overall average methane. In contrast, the simulation average methane is dominated by Sources 1 and 2 because concentration enhancements due to these sources occur under most wind conditions ~~as a result of~~because of their very wide distribution across the region.

5 Regional top-down, or inverse, modelling for emission estimation

Given that the bottom-up emission inventory underestimates the observed methane in the Surat Basin, then one may ask what is the magnitude~~quantity~~ and distribution of methane emissions that is implied by the methane concentration measurements at Ironbark and Burncluith? This is addressed by the inverse modelling approach for regional emissions formulated and applied below.

5.1 Bayesian inverse modelling approach

Our inverse model uses a Bayesian inference approach that incorporates, a source-receptor relationship, concentration measurements, and prior information on source parameters (i.e. source information obtained independently of the measurements) (Rao, 2007; Singh et al., 2015). The approach updates the source prior as concentration measurements are considered, and accounts for both model and observational uncertainties.

Several applications using the Bayesian approach have previously been conducted for methane source estimation, including those at local scale (Yee and Flesch, 2010; Luhar et al., 2014; Feitz et al., 2018) and regional scale (Jeong et al., 2012; Miller et al., 2014; Henne et al., 2016; Cui et al., 2017).

The approach hinges on Bayes' theorem (Jaynes, 2003):

$$p(\mathbf{q}|\mathbf{c}) = \frac{p(\mathbf{c}|\mathbf{q}) \cdot p(\mathbf{q})}{p(\mathbf{c})}, \quad (1)$$

where the *prior* PDF $p(\mathbf{q})$ reflects our knowledge of the source parameter vector $\mathbf{q}$ prior to receiving the concentration observations $\mathbf{c}$; $p(\mathbf{c}|\mathbf{q})$ is the *likelihood* function which is the probability of experiencing $\mathbf{c}$ for a given $\mathbf{q}$ and is typically obtained using a model-derived source-receptor linkage; the *posterior* $p(\mathbf{q}|\mathbf{c})$ relates to the update of $p(\mathbf{q})$ by its modulation by $p(\mathbf{c}|\mathbf{q})$ which contains the new information brought in by the concentration measurements $\mathbf{c}$; and $p(\mathbf{c})$ [$=\int p(\mathbf{c}|\mathbf{q})p(\mathbf{q})d\mathbf{q}$] is the *evidence* and is basically a normalisation constant in the present application (Yee and Flesch, 2010). The likelihood function, also termed the source-receptor relationship, is derived using a transport and dispersion model.

It is assumed that the number of sources (N_s) and their locations $(\mathbf{x}_{s,1}, \ldots, \mathbf{x}_{s,j}, \ldots, \mathbf{x}_{s,N_S})$ where $\mathbf{x}_{s,1} \equiv (x_{s,1}, y_{s,1}, z_{s,1})$ are given *a priori* and the source emissions are positive and non-zero. The emission rates of these sources are to be estimated, and these are represented by $\mathbf{q} \equiv (q_1, \ldots, q_j, \ldots, q_{N_S})$ with a total of N_S unknown emission rates. Assuming each source emission to be independent, the prior PDF can be written as:

$$p(\mathbf{q}) = \prod_{j=1}^{N_s} p(q_j). \quad (2)$$

Assuming that the model and measurement uncertainties are independent and distributed normally, the total likelihood of all $\mathbf{c}$ for a given hypothesis of $\mathbf{q}$ is calculated as (Yee, 2012)

$$p(\mathbf{c}|\mathbf{q}) = \prod_{i=1}^{N_m} \frac{1}{\sqrt{2\pi}\left(\sigma_i^2 + \sigma_{m,i}^2\right)^{1/2}} \exp\left\{-\frac{\left(c_{m,i}(\mathbf{q}) - c_i\right)^2}{2\left(\sigma_i^2 + \sigma_{m,i}^2\right)}\right\}, \quad (3)$$

$\mathbf{c} \equiv (c_1, \ldots, c_i, \ldots, c_{N_m})$, c_i is the observed concentration at i-th instant (time and location), $c_{m,i}$ is the corresponding modelled concentration for a given hypothesis of $\mathbf{q}$, σ_i is the independent measurement error, $\sigma_{m,i}$ is the independent model error, N_m is the number of concentration data (which can be time series from several independent monitors). $c_{m,i}$ for all hypotheses, or possible values, for $\mathbf{q}$ is calculated and used in constructing the likelihood distribution $p(\mathbf{c}|\mathbf{q})$. Hence the posterior PDF for a given source hypothesis $\mathbf{q}$ is calculated as:

$$p(\mathbf{q}|\mathbf{c}) = \frac{1}{Z_0} \prod_{j=1}^{N_s} p(q_j) \prod_{i=1}^{N_m} \frac{1}{\sqrt{2\pi}\left(\sigma_i^2 + \sigma_{m,i}^2\right)^{1/2}} \exp\left\{-\frac{\left(c_{m,i}(\mathbf{q}) - c_i\right)^2}{2\left(\sigma_i^2 + \sigma_{m,i}^2\right)}\right\}, \quad (4)$$

where Z_0 is equivalent to $p(\mathbf{c})$ and is essentially a normalisation constant. The posterior yields probabilities of all emission rates ($\mathbf{q}$) considered.

The total modelled concentration at a given location $\mathbf{x}_r$ and time is determined as

$$c_{m,i} = \sum_{j=1}^{N_s} c_{m,ij}. \quad (5)$$

Because methane is treated as a passive tracer, the concentration field simulated for one rate of emission can be scaled linearly for another without the need to re-run the model. Thus

$$c_{m,ij} = q_j \alpha_{ij}(\mathbf{x}_{s,j}, \mathbf{x}_{r,i}), \quad (6)$$

for each emission rate component of $\mathbf{q}$. The quantity $\alpha_{ij}(\mathbf{x}_{s,j}, \mathbf{x}_{r,i})$ is the source-receptor relationship or coupling coefficient and is equivalent to the modelled mean concentration at a given time and location $\mathbf{x}_{r,i}$ due to j-th source release at location $\mathbf{x}_{s,j}$ with a unit emission rate.

In Eq. (4)~~(4)~~, in the absence of an informative prior, a uniform prior PDF can be used with the given limits (q_{max}, q_{min})

$$p(q_j) = \frac{1}{q_{max,j} - q_{min,j}}, \quad (7)$$

with the probability being zero outside these bounds.

If the prior is Gaussian, then

$$p(q_j) = \frac{1}{\sqrt{2\pi}\,\sigma_{p,j}} \exp\left\{-\frac{(q_j - q_{p,j})^2}{2\sigma_{p,j}^2}\right\}, \quad (8)$$

where q_p and σ_p are the prior mean emission rate and its standard deviation, respectively.

High dimensionality of the posterior makes its direct computation and the subsequent integration (the 'brute-force' method) over the source-parameter space very expensive or perhaps even impossible. For Gaussian priors and uncertainties, the posterior can be solved for the mean and variance with their analytical matrix forms (Tarantola, 2005; Jeong et al., 2012). To make the inverse approach more generally applicable and efficient, we use a Markov chain Monte Carlo (MCMC) technique incorporating the Metropolis-Hastings algorithm to sample the posterior PDF (Tarantola, 2005; Yee, 2012). With MCMC, non-Gaussian priors or uncertainties, or parameters with known physical constraints can also be included (Miller et al., 2014). The normalization constant Z_0 in Eq. (4)~~(4)~~ need not be known before MCMC samples can be drawn from the posterior PDF. This ability to generate a sample without knowing this constant of proportionality (which is often extremely difficult to compute) is a major feature of MCMC algorithms (Luhar et al., 2014). The frequency distribution of the MCMC-generated samples represents the posterior.

The posterior PDF can be marginalized to obtain the mean emissions rate for each source as follows:

$$\bar{q}_j = \int q_j \, p(\mathbf{q}|\mathbf{c}) \, d\mathbf{q}, \quad (9)$$

and likewise, the variance can also be determined.

5.2 Construction of the hourly source-receptor relationship

In order to use hourly measurements, the source-receptor relationship needs to be calculated every hour for every source (real or potential) location and every monitor location using either forward or backward transport modelling (Rao, 2007). Generally speaking, if the number of source locations under consideration is greater than the number of receptor locations (as for the present case) then the backward approach is much more computationally efficient (Luhar et al., 2014).

In the backward approach, source emissions are~~matter is~~ tracked backwards in time from a monitor treated as a source. The value at a given point of the constructed backward concentration field is analogous to the magnitude of contribution made by an emitting source at that point to the true (i.e. forward) modelled concentration at the monitor. Hence, we can use a single backward source-receptor relationship distribution determined every hour to get the contribution made by each real or potential source located in the domain. This contrasts with the forward modelling approach in which each source location must be considered as a unique, separate source and its dispersion computed for every hour. Essentially, the source-receptor relationship furnishes a way to chart the distribution of source potential within given geographical domain. However, it does not quantitatively allocate the real contribution of sources within the domain to the concentration levels detected at monitoring stations— this is done by the Bayesian inference (Eq. (4)~~(4)~~).

One backward approach for regional scale is to use backward trajectories constructed by only using three-dimensional winds computed from a meteorological model (e.g., Cheng et al., 1993). However, such wind trajectories only represent advective transport and do not account for turbulent mixing which causes a plume to disperse as it travels in the atmosphere. If measurements given at a high temporal resolution, e.g. hourly averages, are to be used for inversion it is necessary that the influence of atmospheric flow and dispersion processes that occur at such scales is considered. This can only be properly done by simulating backward tracer plumes which considers both advection and turbulent mixing.

We modify TAPM to construct backward dispersing plumes. The Eulerian dispersion module in TAPM comprises a solution of the advection-diffusion equation for the ensemble mean concentration c, which for a passive species is (e.g. Yee et al., 2008):

$$\frac{\partial c}{\partial t} + \bar{\mathbf{u}}.\nabla c - \nabla.(\mathbf{K}\,\nabla c) = S, \qquad (10)$$

in which the unknown turbulent flux terms are closed using the K-theory or gradient transport approach. The forcing term S represents species emissions. The elements of the eddy diffusivity tensor $\mathbf{K}$ are zero except along its main diagonal (K_x, K_y, K_z). ~~The~~ D~~d~~iffusion is assumed to be symmetric in the horizontal plane, so $K_x = K_y = K_H$ (say). K_H and K_z are determined using the modelled turbulent kinetic energy (TKE) and the TKE dissipation rate.

The vertical component $\bar{w}$ of the mean wind vector $\bar{\mathbf{u}}$ ($\equiv \bar{u}, \bar{v}, \bar{w}$) in Eq. (10)~~(10)~~ is determined by using the continuity equation after the mean horizontal wind velocity components ($\bar{u}, \bar{v}$) are calculated.

The Eulerian adjoint of Eq. (10)~~(10)~~ describes the backward evolution of a scalar field (c^*), and is also termed backward or retro plume, adjoint function, sensitivity function, or influence function, and is given as (Marchuk, 1995; Pudykiewicz, 1998; Hourdin and Talagrand, 2006; Yee et al., 2008)

$$-\frac{\partial c^*}{\partial t} - \bar{\mathbf{u}}.\nabla c^* - \nabla.(\mathbf{K}\nabla c^*) = M, \qquad (11)$$

where M is the forcing term representing the measurement distribution, which is treated as a source at the measurement (or receptor) location. Therefore, α_{ij} in Eq. (6)~~(6)~~ is equivalent to c^* derived for a unit emission rate.

The implementation of Eq. (11)~~(11)~~ in TAPM wasis done through changes in the forward model code as follows. The meteorological and turbulence fields calculated by the model at every hour (not hourly-averaged) wereare stored for the full simulation period. The modelled horizontal components ($\bar{u}, \bar{v}$) of wind wereare reversed (i.e. by sign change). The (inverted) vertical wind component ($\bar{w}$) wasis then calculated by solving the continuity equation given the reversed horizontal wind components. The turbulence parameters values remained the same. The diffusivities in the dispersion component are positive and do not have any correction for counter-gradient flux in the vertical, and, therefore, they were not modified for the backward mode. The two monitor locations were treated as separate 'sources' each having unit emission, and hourly-averaged plume dispersion fields due to these 'sources' was determined by running the TAPM dispersion module backwards in time for the entire simulation duration by using the reversed winds calculated previously. The meteorological and turbulence fields were linearly interpolated in time for dispersion calculations for model time steps lying between two successive hours. The resulting hourly-averaged backward concentration fields were used as the source-receptor relationship. For inversion, Since wwe assume that all methane sources are located near the ground within the lowest model level (i.e. 10 m AGL), and, therefore, only the 10-m hourly source-receptor relationship was required.

One complexity with doing a backward dispersion calculation using one continuous release over the full simulation period over a large domain, as done here, is that the source-receptor field at a given hour is a superposition of plume footprints from the current hour as well as previous hours (typically 4–5 hours for the present domain size). So, there is a time history of the plume in the source-receptor field at a given time (whose influence becomes smaller and smaller as the distance between the source and the receptor becomes smaller, the domain size decreases, the averaging time is increased, or when the winds are strong). However, this time history in a backward run corresponds to future hours in a forward run, so at a given hour there can be a time mismatch between the forward concentration at a grid point and the backward concentration at that point. One way to deal with this problem is to do a separate backward runsimulation for eachevery hour separately for the whole simulation period; however, this is extremely expensive computationally. As a practical and approximate solution to this issue, at a particular backward travel hour (t) the plume travel time (t_r) from the release point (i.e. the monitor location) to a grid

point ($\mathbf{x}$) is determined by releasing a second tracer (with concentration $c^* = c_2^*$) backwards from the monitor simultaneously with the main tracer (with concentration $c^* = c_1^*$) with the same tracer properties except that it decays exponentially with a decay rate of λ (taken as= 10^{-6} s^{-1}), so

$$c_2^*(\mathbf{x}, t) = c_1^*(\mathbf{x}, t)\exp(-\lambda t_r), \tag{12}$$

which gives

$$t_r(\mathbf{x}, t) = \frac{1}{\lambda}\ln\left[\frac{c_1^*(\mathbf{x}, t)}{c_2^*(\mathbf{x}, t)}\right]. \tag{13}$$

The source-receptor value ($c^* = c_1^*$) calculated at a grid point location $\mathbf{x}$ at a given backward travel hour $t = t_b$ is then taken equal to that calculated at the same location at $t = t_b + t_r$ (where t_r rounded to the nearest hour). The forward travel hour for a grid point is equal to the total hours in a simulation period minus t_b. Therefore, the source-receptor relationship (c^*) for the grid points at time t is constructed from the output of c_1^* at different times according to the value of t_r at individual grid points. A maximum value for t_r needs to be specified, which we take 15 h – approximately the time taken by the backward plume from either monitor to leave the (innermost) model domain (beyond this value, c^* is zero). This is needed to avoid occasional spurious smearing in the spatial patterns of c^* caused by a very diluted, turning, or recirculating backward plume that has travelled longer than t_r overlapping the direct backward plume at a particular location.

To illustrate the modelled forward and backward relationship and the impact of accounting for t_r, Figure 7~~Figure 7~~a presents the hourly-averaged forward modelled 10-m concentration field (c) in the innermost model domain on 20 June 2016 at 2300 h (local standard time) due to a sample of 12 point sources, all emitting at the same fixed rate and whose locations correspond to some of the feedlots. Figure 7~~Figure 7~~b is the backward modelled 10-m concentration field (c^*) for Ironbark (I) at the same time without the travel time correction (i.e. $t_r = 0$), and Figure 7~~Figure 7~~c is the same field with the travel time correction. Essentially, the value at any point in the backward field is equivalent to the forward model concentration value at Ironbark if there were a source at that point with the same emission rate (as the backward emission rate). The backward concentration value at a given location represents the probability (including both frequency and intensity) a source emission at that location adds to the concentration at the monitoring site. The backward field is mainly determined by flow the field across the domain and the separation between the receptor and the source. Figure 7~~Figure 7~~a suggests that only one source, S1, contributes to concentration at Ironbark. Figure 7~~Figure 7~~c is consistent with this, in which the backward plume from Ironbark only impacts S1 with the same magnitude, and not any other source location. On the other hand, the backward plume in Figure 7~~Figure 7~~b does not pass through any of the 12 sources, meaning no impact of these sources at Ironbark, which obviously is not correct as S1 does impact Ironbark (Figure 7a). Figure 7~~Figure 7~~c is the source-receptor relationship (normalised by the fixed emission rate) for Ironbark for the hour under consideration.

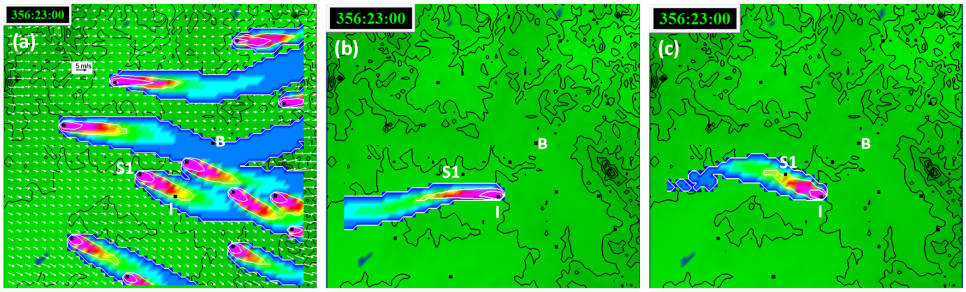

Figure 7. (a) Forward modelled hourly-averaged 10-m concentration field on 20 June 2016 at 2300 h (local standard time) due to 12 point sources, with the 10-m modelled winds also shown; (b) backward modelled 10-m concentration field for Ironbark (I) at the same time without the travel time correction ($t_r = 0$); and (c) backward modelled 10-m concentration field for Ironbark with the travel time correction. Each source point has the same emission rate. The plume contours (white) and colours represent the same concentration values. The black contours represent the topography. The model domain size is 370 × 370 km², and the Ironbark (I) and Burncluith (B) locations are shown.

A hourly-averaged modelled backward concentration field (c^*/q, s m^{-3}) at the lowest model level (i.e. 10 m AGL), an example of which ~~was~~is shown in Figure 7~~Figure 7~~c, obtained for a unit emission rate (q = 1 g s^{-1}) is in essence the required hourly source-receptor relationship which can be linearly scaled for any other emission rate (q).

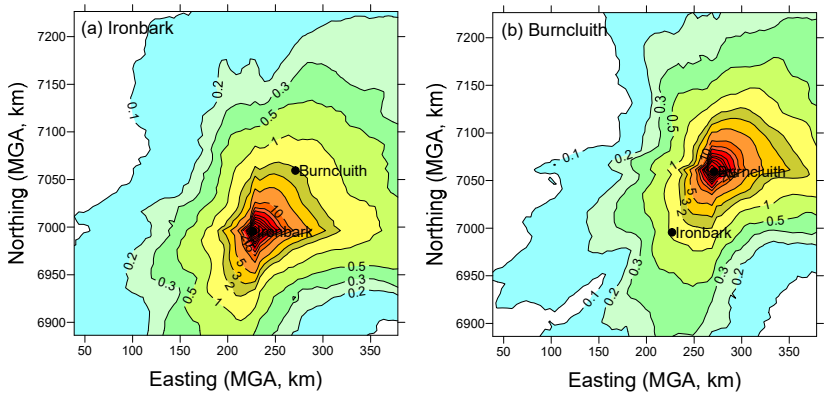

Figure 8. Normalised modelled backward distribution of near-surface concentration (c^*/q, × 10^{-9} s m^{-3}), which is an average over the entire study period: (a) Ironbark, and (b) Burncluith.

The modelled backward concentration field (c^*/q, s m^{-3}) averaged over all hourly fields over the simulation period (i.e. 1.5 years) for Ironbark is shown in Figure 8~~Figure 8~~a, which suggests that, overall, any sources located farther from the monitoring station would contribute less as plume concentrations decrease with increasing distances, and vice versa. The directional distribution of the backward field is also a function of the distribution of regional winds which determine how often the receptor is downwind of a source (see wind roses in Figure S3). The values in the south-east and north-west corners of the study domain are particularly low, so potential sources located there would, on average, have relatively low probability of being sampled at Ironbark.

The backward distribution for Burncluith (Figure 8~~Figure 8~~b) is very similar, but since it is located north of Ironbark it would sample potential sources in the north-east better.

The two monitoring sites combined would sample the bulk~~most part~~ of the CSG sources between and around them in the domain (which was the prime objective of our monitoring).

5.3 Bayesian inversion setup

Assuming that emission rates are time invariant, we use all hourly methane data (N_m) from the two monitoring stations together in one combined Bayesian calculation to determine the total emission rates from gridded sources using Eq. (4)~~(4)~~. Since each hour corresponds to a unique meteorological condition, the use of all hours simultaneously provides the meteorological variability needed to achieve a better "triangulation" for source estimation. ~~The greater the number of useful measurement hours, the greater the variability, and hence the better the constraining of the source.~~ This approach is similar to that used by Luhar et al. (2014) in the context of a local point source. It requires the source-receptor matrix ($c^*(\mathbf{x}, t)$) for each hour for each measurement site (e.g. Figure 7~~Figure 7~~c).

For the purposes of inferring emissions using our Bayesian methodology, the source array of 69 × 69 used in the forward modelling above is rather too large a source number to explore all the source possibilities (i.e. hypotheses) on hourly basis, even with use of the MCMC sampling. Moreover, there is only a limited amount of information available from just two monitoring sites. A coarser array of sources is more practicable, and consequently we consider an array of 11 × 11 localised sources ($N_s = 121$, cell size ~ 31 × 31 km^2) within the same model domain~~, whose total emission rates are time invariant during a given simulation period~~. No sub-grid variability of these emission sources~~rates~~ is considered. The hourly source-receptor relationships calculated at 5 × 5 km^2 resolution for Ironbark and Burncluith were used. Our inverse methodology as used does not distinguish between different source categories. This is mainly because the concentration of methane alone was monitored and not tracers specific to methane source types. Therefore, there are no separate sources categories in the inferred emissions~~,~~ (unlike what was done for the forward simulation)~~,~~ and only total emissions are optimised.

To reduce serial correlations in the sequence of MCMC samples drawn from the posterior using the Metropolis-Hastings algorithm, we only retained every 5th sample. The total number of useable samples was 21,000 for each source, of which the first 1,000 samples were discarded as "burn-in" samples. The selected samples were then used in the calculation of the source statistics.

6 Inversion using ~~the~~ 'synthetic' methane concentration data

A 'synthetic' inverse run is first performed by using the modelled~~simulated~~ hourly-averaged time series of methane concentration at Ironbark and Burncluith obtained using~~involving~~ the bottom-up inventory (regridded to 11 × 11 sources, see Figure 9~~Figure 9~~a, to be consistent with the source number considered in the inversion) to investigate whether the inverse methodology is able to retrieve the bottom-up emissions and under what type of priors and their uncertainties. The results of this exercise provide a useful guidance to the subsequent inversion using the actual measured~~real-world~~ methane data~~, particularly about the selection of the prior and its uncertainty specification~~.

Only the forward modelled (or synthetic) concentrations at the two monitoring sites were used at times when valid (or filtered) methane observations were available ($N_m = 10581$). The background measurement uncertainty was taken as σ = 3.5 ppb based on the previous calculation, and the uncertainty in the transport model was assumed to be σ_m = 20% of the modelled concentration (Yee and Flesch, 2010; Luhar et al., 2014). ~~(~~These values are~~will~~ also ~~be~~ used later in Section 7 for ~~the~~ inversions based on the methane data.~~)~~

6.1 Selection of the prior

Specifying the prior PDF $p(\mathbf{q})$ is an important step, even for the present synthetic case because we are still limited to the same degree of information available (i.e. ~~the modelled~~ concentrations ~~time series~~ from only two sites), the same number of unknown sources to estimate, and the same domain size as in the inversion case with the real concentration data considered subsequently. We specify the following two Gaussian priors:

- An identical (or uniform) Gaussian $p(\mathbf{q})$ for each source with a mean methane emission rate q_p = 45.4 g s^{-1} (= 1.43 × 10^6 kg yr^{-1}) per source is specified, with a specified standard deviation σ_p. This mean value is essentially the total bottom-up emission from the domain divided by the number of sources (i.e. 121).
- The bottom-up inventory emissions as a Gaussian prior. The inventory emissions shown in Figure 9~~Figure 9~~a are taken as the mean values of a Gaussian prior for each source, with a specified standard deviation σ_p.

6.2 Results for the synthetic case

In Figure 10~~Figure 10~~a, the methane emission rates inferred by the inverse~~top-down~~ methodology for the uniform Gaussian prior case with a prior uncertainty of σ_p = 5% of the mean for each source are plotted against the bottom-up inventory sources

used to construct the synthetic concentration time series for the inversion ~~(the number of sources is 11 × 11)~~. Ideally, the data points should fall along the 1:1 line, but due to the limited amount of information supplied via the modelled concentrations from only two monitors and the prior being narrow and not very informative, most inferred emission ~~emission~~ rates are scattered around the prior mean, i.e. q_p = 45.4 g s^{-1}, although it is apparent that a few inferred emission rates are greater than this value and tending to the corresponding bottom-up emission rates. The spatial distribution of the inferred emissions is presented in Figure 9~~Figure 9~~b, which, as expected, is much more uniform than the bottom-up inventory emissions in Figure 9~~Figure 9~~a.

When the prior uncertainty is increased to σ_p = 10% of the mean (Figure 10~~Figure 10~~b), the scatter increases, but most inferred emissions still stay around the prior mean, barring some higher-end ones which move further closer to the corresponding bottom-up emission rates. Further increase in σ_p leads to a larger increase in scatter, with no improvement in the inferred emissions.

The total inferred methane emissions are 179.3 × 10^6 and 175.7 × 10^6 kg yr^{-1} for σ_p = 5% and 10% of the mean, respectively – values very similar to the bottom-up inventory total of 173.2 × 10^6 kg yr^{-1}.

Figure 11~~Figure 11~~a with 5% prior uncertainty is the same as Figure 10~~Figure 10~~a except that the ~~Gaussian prior with the~~ individual bottom-up inventory emissions (Figure 9a) have been used as the~~its~~ mean values of the Gaussian prior~~has been used~~. The inversion retrieves the bottom-up emissions very well with a little scatter in the data points. The spatial distribution of the inferred emissions is presented in Figure 9~~Figure 9~~c for this case, which is very similar to that of the inventory emissions in Figure 9~~Figure 9~~a. As the prior uncertainty is increased to σ_p = 10% of the mean (Figure 11~~Figure 11~~b), the uncertainty in the retrieved emissions gets larger, with a slight decrease in the correlation.

The total inf~~c~~r~~a~~rred emissions corresponding to Figure 11~~Figure 11~~a and Figure 11~~Figure 11~~b~~a~~ are 164.8 × 10^6 and 156.9 × 10^6 kg yr^{-1}, respectively – values somewhat smaller than the inventory total 173.2 × 10^6 kg yr^{-1}.

A comparison of Figure 9~~Figure 9~~c with the bottom-up inventory (Figure 9~~Figure 9~~a) indicates that some regions in the south-east, for example the strong coal mining source on the eastern boundary at the grid location (11, 4), and north west corners are not replicated ~~as well~~ by the inverse model. This is despite a ~~perfect/~~strong prior with a relatively small uncertainty, and could be due to the fact that the two monitoring locations do not sample this source area sufficiently (see Figure 8~~Figure 8~~) (bcause they were sited to optimally sample the CSG region). Extra monitoring stations and/or separate~~,~~ narrower priors for such sources ~~that make very small contributions to methane at the two sites~~ would be needed to cover these areas better.

The ~~above~~ synthetic case results suggest that with only two monitoring locations the bottom-up inventory Gaussian prior works well and is, indeed, needed. Obviously, a small prior uncertainty biases the inferred emission distribution towards the prior $p(\mathbf{q})$, and what uncertainty level is selected depends on the available information supplied to the inversion. The synthetic case reveals that σ_p ~ 5% of the mean is needed to retrieve the bottom-up emissions. Thus, for a real inversion using the methane

measurements one may expect that an evena narrowertighter prior uncertainty maywould be needed. Further guidance on σ_p can also comes from a comparison of the forward modelled methane concentrations using the inferred emissions with the methane observations from the two sites.

The synthetic case results also demonstrated that the regional inverse model formulated was stable and feasible with MCMC.

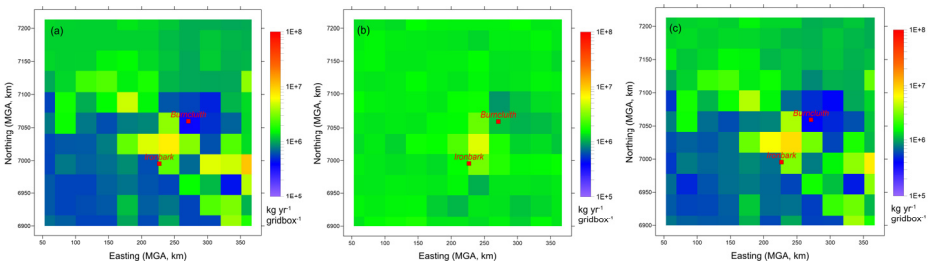

Figure 9. Emission rates of CH_4 (kg yr^{-1} $gridcell^{-1}$) (a) based on the bottom-up inventory, (b) estimated by the synthetic inversion using a uniform Gaussian prior with an uncertainty of σ_p = 5% of the mean for each source, and (c) estimated by the synthetic inversion using the bottom-up inventory in (b) as a Gaussian prior with an uncertainty of σ_p = 5% of the mean for each source. There are 11 × 11 sources, and the grid cell size is 31 × 31 km^2.

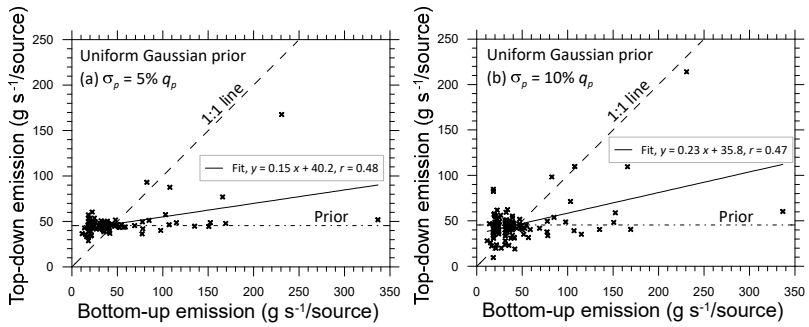

Figure 10. Scatter plot of the bottom-up inventory methane emission rates (g s^{-1} per source) versus those inferred from the inverse (top-down) methodology for the synthetic case involving a uniform Gaussian prior with a prior uncertainty of (a) σ_p = 5% and (b) σ_p = 10% of the mean for each source. The number of sources is 11 × 11. The dash-dot line is the mean value of the prior, the dashed line is the 1:1 line (i.e. perfect agreement) and the solid line is the least-squares fit.

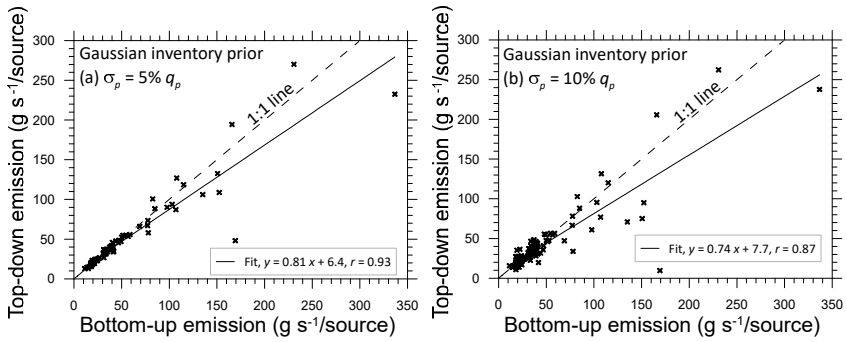

Figure 11. Scatter plot of the bottom-up inventory methane emission rates (g s^{-1} per source) versus those inferred from the inverse (top-down) methodology for the synthetic case involving the bottom-up inventory source emissions as the mean of a Gaussian prior with a prior uncertainty of (a) σ_p = 5% and (b) σ_p = 10% of the mean for each source. The number of sources is 11 × 11. The dashed line is the 1:1 line (i.e. perfect agreement) and the solid line is the least-squares fit.

7 Inversion using the methane measurements

We now use the filtered methane measurements from the two monitoring stations to quantify emissions ~~(with so $N_m = 10581$,) in a single Bayesian inverse run. The uncertainty in the measurements is σ = 3.5 ppb and the modelled uncertainty is σ_m = 20% of the mean concentration, using our inverse methodology)~~. The above synthetic case results have revealed that a good, tight prior is needed to infer emissions within the selected domain using concentrations from the two monitoring locations. We consider several cases ~~One may, of course, ask as to~~ to examine how the source inference ~~using the real-world measurements~~ is influenced using the real-world measurements depending on the type of prior that may be available, ranging from a non-informative one to the most informative we have, i.e. the bottom-up inventory.

~~We use the same filtered methane observations as used in the forward transport modelling (so N_m = 10581) in a single Bayesian inverse run. The uncertainty in the measurements is σ = 3.5 ppb and the modelled uncertainty is σ_m = 20% of the mean concentration, as used in the synthetic inversion.~~

7.1 Priors and inferred emissions

Three cases involving different priors are considered.

7.1.1 Non-informative uniform prior (Case 1)

A case of non-informative prior is first considered in which the only constraint is that the emission rate for each source lies within the broad range 10–10,000 g s^{-1} with uniform probability, where the upper limit is nearly double the total domain-wide bottom-up inventory.

The inferred emissions (Figure 12~~Figure 12~~a) between the two monitoring sites and around the centre of the region are qualitatively in accordance with the bottom-up inventory emissions (Figure 9~~Figure 9~~a), but with larger magnitudes. In contrast, the inverse estimates in locations farther from these source areas are smaller than the inventory emissions. Notably~~Remarkably~~, the total inferred emission with the non-informative prior is 162.0 × 10^6 kg yr^{-1} which compares well with the inventory total. The largest emission rate of about 1100 g s^{-1} per grid cell in Figure 12~~Figure 12~~a is about 10% of the upper bound of the specified prior range.

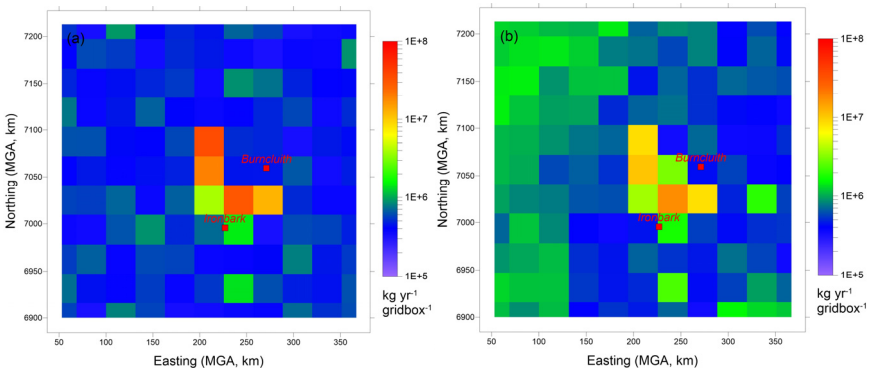

Figure 12. Emission rates of CH_4 (kg yr^{-1} $gridcell^{-1}$) estimated by the inversion: (a) with a non-informative uniform prior (Case 1); and (b) with a uniform Gaussian prior (Case 2). There are 11 × 11 sources, and the grid cell size is 31 × 31 km^2.

7.1.2 Uniform Gaussian prior (Case 2)

Next, a more realistic prior PDF is specified with a Gaussian distribution having an identical mean of 45.4 g s^{-1} and σ_p = 10% of the mean, for each source. The mean is the same as that is used in one of the synthetic runs.

The inferred emissions for this case shown in Figure 12~~Figure 12~~b are qualitatively similar to Figure 12~~Figure 12~~a; however, in the former the high emission sources are relatively less pronounced, with emissions from other source locations generally being larger. The total annual emission from the Surat Basin obtained using this inversion is 143.1 × 10^6 kg yr^{-1}.

7.1.3 Gaussian prior usingwith the bottom-up inventory emissions (Case 3)

In this case, as in the synthetic case corresponding to Figure 9c, the bottom-up inventory emissions shown in (Figure 9Figure 9a) are used intaken as the mean values of a Gaussian prior for each source. A small prior uncertainty is also guided by the synthetic case results presented earlier. As every source prior now has a more realistic specification of the mean value compared Case 2, the the uncertainty in the prior needs to be relatively is chosen to be small er than that specified in Case 2. A small prior uncertainty is also guided by the synthetic case results presented earlier.

The inferred emission rates in Figure 13Figure 13a obtained for Case 3 with σ_p = 1% of the mean (Case 3a) appear very similar to the inventory emission rates (Figure 9Figure 9a). The fact that even the intense emission on the eastern boundary of the domain present in the inventory is mostly reproduced despite this area being not sampled preferentiallyrelatively sufficiently by the two network locations means that the chosen prior with a very small uncertainty is somewhat too inflexible thatwhich forces the inversion towards a result that is very similar to the prior itself, thus in essence likely overriding the information inherent in the concentration observations.

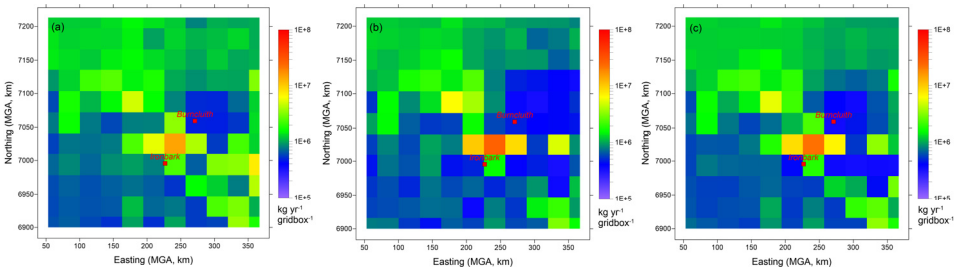

Figure 13. Emission rates of CH_4 (kg yr^{-1} $gridcell^{-1}$) estimated by the inversion with a Gaussian prior involving mean values equal to the bottom-up emissions (Figure 9Figure 9a) and the standard deviation equal to (a) 1% (Case 3a), (b) 5% (Case 3b) and (c) 3% (Case 3c) of the mean values. There are 11 × 11 sources, and the grid cell size is 31 × 31 km^2.

Figure 13Figure 13b is the sameobtained using the same inverse model setup as Figure 13Figure 13a, except that the prior is relaxed somewhat by increasing σ_p to 5% of the mean (Case 3b). This leads to the source areas in the centre of the Surat Basin and those between Ironbark and Burncluth becoming more conspicuous. In contrast, the source areas near the eastern boundary of the domain nearly fade, with the concentration observations applying greater influence in areas where the source-receptor relationship, shown in Figure 8Figure 8, is stronger. Clearly, the inversion is sensitive to σ_p, however, it is apparent that a σ_p between= 1% andto 5% of the mean would yields a reasonable trade-off between the benefit of the inversion approaching the prior in areas where the chances of the two monitoring stations detecting methane signal is small and simultaneously making

sure that the selected prior would not unduly overrule the information supplied by the concentration measurements. Consequently, another inversion was performed for σ_p = 3% of the mean (Case 3c). The inferred emissions from this run presented in Figure 13~~Figure 13~~c in essence stand between those~~the inferred emissions~~ for σ_p = 1% and ~~those for~~ 5% of the mean. This Case 3c inversion is our best estimate, which gives an annual total CH_4 emission of 165.8 × 10^6 kg yr^{-1}. The fine tuning of the prior uncertainty is also~~also has~~ guided ~~some trial and error component driven~~ by the need that the inferred emissions are able to describe the measured concentrations when used in a forward model simulation (see the validation Section 7.2).

~~As noticed in the synthetic inversion case, and in Figure 13a and Figure 13b, a large prior uncertainty biases the inversion towards emission rates that have high probability, which may indicate that the number of monitoring stations is insufficient for the uncertainty in the prior to be relaxed.~~

Figure 14~~Figure 14~~a presents the difference between the inferred methane emissions given in Figure 13~~Figure 13~~c and the bottom-up inventory emissions in Figure 9~~Figure 9~~a. The largest difference is found for the grid box between Ironbark and Burncluith, with the inferred emissions (22.9 × 10^6 kg yr^{-1}) being larger by approximately a factor of three than the latter (7.3 × 10^6 kg yr^{-1}). The total inventory emission for this source grid is controlled by CSG Processing (51%); feedlots, poultry and piggeries combined (32%); and CSG Production (6%) sectors.

The calculated posterior uncertainty (standard deviation) relative to the inferred mean emissions (%) corresponding to Figure 13~~Figure 13~~c (Case 3c, σ_p = 3% of the prior mean) is presented in Figure 14~~Figure 14~~b. Most of these values are ~~very~~ similar to the relative uncertainty in the prior (i.e. σ_p = 3% of the prior mean). Interestingly, the farthest grid point due east of Ironbark ~~(11, 4)~~, which corresponds to a relatively strong coal mine source in the bottom-up inventory (Figure 3~~Figure 3~~d), has a disproportionally large uncertainty (~ 25%), probably due to limited sampling.

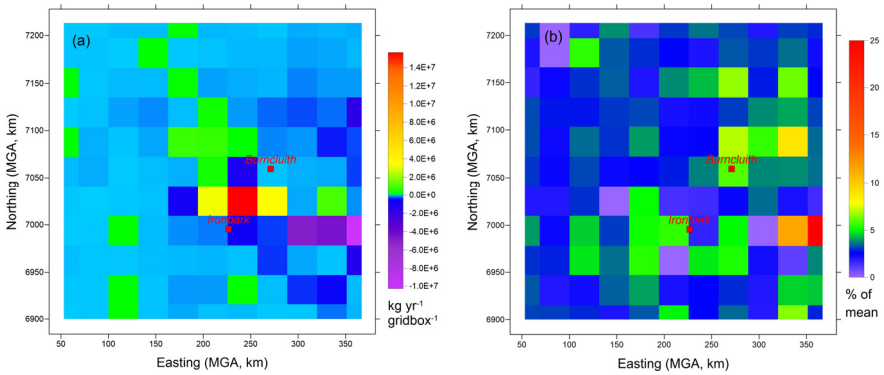

Figure 14. (a) Difference between the Case 3c inferred methane emissions (Figure 13~~Figure 13~~c) and the bottom-up inventory emissions in Figure 9a (kg yr^{-1} gridbox^{-1}), and (b) posterior uncertainty (standard deviation) relative to the Case 3c inferred mean emissions (%) ~~presented in Figure 13c (Case 3c)~~. There are 11 × 11 sources, and the grid cell size is 31 × 31 km^2.

7.2 Validation of the inferred emissions ~~estimates~~

To examine to what extent the inferred emissions represent the methane concentration measurements compared to the bottom-up emissions, we conducted three separate forward transport model runs using the inferred emissions from the above inversion~~inverse modelling~~ Cases 1, 2, and 3 ~~(i.e. Figure 12a, Figure 12b and Figure 13, respectively)~~.

The q-q plots for ~~of the observed data against the modelled CH_4 computed using the~~the Case 1 inferred emissions (Figure 15~~Figure 15~~a, d) show that there is an overestimation of methane at both monitoring stations for the higher-end concentrations, but the simulated CH_4 at Ironbark is much better reproduced than when using the bottom-up emissions (grey lines). For Burncluith, the overestimation is almost as large in magnitude as the underestimation obtained when the inventory emissions are used.

The Case 2 inferred emissions obtained with a better ~~involving a proper, but still crude,~~ prior lead to a significant improvement in the methane simulation, especially at Burncluith (Figure 15~~Figure 15~~b, e).

As apparent from Figure 15~~Figure 15~~c, f, the use of the bottom-up inventory as the prior in Case 3c with 3% prior uncertainty relative to the mean yields emission estimates that further improve the simulation of methane, especially at Ironbark. Comparatively, the use of 1% prior uncertainty leads to a better performance at Ironbark but worse at Burncluith. With 5% prior uncertainty, the performance is other way round. With the exception of about 4 outlying data points at the higher-end of the concentration distribution, the Case 3c inversion with 3% prior uncertainty (corresponding to Figure 13~~Figure 13~~c) leads

to the best overall model reproduction of the measured CH_4 from the two monitoring sites. The underprediction seen when the inventory emissions are used (grey curves in Figure 15~~Figure 15~~) is nearly eliminated.

Table 1~~Table 1~~ presents performance statistics for the three Case 3 inversions and for the bottom-up emissions as to how well they describe the methane concentration measurements at the two sites when used in the forward modelling. The observed (O) and modelled (M) concentrations are paired in time for these statistics, which are: r = correlation coefficient, IOA = index of agreement, a = slope and b = intercept of the linear best fit line (with observations along the x-axis), FB = fractional bias, and RMSE = root mean square error. FB = $2(\bar{O} - \bar{M})/(\bar{O} + \bar{M})$, which varies between -2 (overestimation) and +2 (underestimation); and IOA = $1 - [\overline{(M-O)^2}/(\overline{|M-\bar{O}| + |O-\bar{O}|})^2]$, where 0 = no agreement and 1 = perfect agreement. The IOA, unlike r, is sensitive to differences between the observed and model means as well as to certain changes in proportionality.

Compared to the case with the bottom-up emissions, the inferred emissions improve the prediction of methane concentration at Ironbark, except for a slight decrease in correlation. At Burncluith, the improvement is limited to the slope. Note that these statistics are dominated by lower-end concentrations which are much more numerous than the higher-end concentrations. The q-q plots in Figure 15~~Figure 15~~ on the other hand tend to emphasise more model performance for a relatively small number of higher-end concentrations.

Some deterioration in the model performance when the inferred emissions are used could be caused by the 11 × 11 source distribution representing the emissions in the domain being rather coarse (compared to 69 × 69 used for the bottom-up emissions). Considering the performance statistics in Table 1~~Table 1~~ and the q-q plots in Figure 15~~Figure 15~~c and f, the Case 3c inversion is our best estimate of emissions.

Table 1: Performance statistics for the emissions from the Case 3 inversions and for the bottom-up emissions as to how well they describe the methane concentration measurements at the two sites when used in ~~the~~ forward modelling (r = correlation coefficient, IOA = index of agreement, a = slope, b = intercept, FB = fractional bias, RMSE = root mean square error).

Emissions	Ironbark (N = 6432)						Burncluith (N = 4149)					
	r	IOA	a	b (ppb)	FB	RMSE (ppb)	r	IOA	a	b (ppb)	FB	RMSE (ppb)
Case 3a ($\sigma_p = 1\%\ q_p$)	0.53	0.68	0.36	1153	0.61×10^{-3}	25.5	0.69	0.82	0.71	527	-0.45×10^{-3}	11.1
Case 3b ($\sigma_p = 5\%\ q_p$	0.49	0.66	0.55	863	-1.98×10^{-3}	32.0	0.58	0.71	0.87	244	-1.26×10^{-3}	16.8
Case 3c ($\sigma_p = 3\%\ q_p$	0.51	0.68	0.48	954	-0.72×10^{-3}	28.4	0.63	0.76	0.79	381	-0.86×10^{-3}	14.0
Bottom-up inventory emissions	0.57	0.59	0.25	1360	3.36×10^{-3}	25.4	0.74	0.84	0.61	707	0.35×10^{-3}	9.4

725

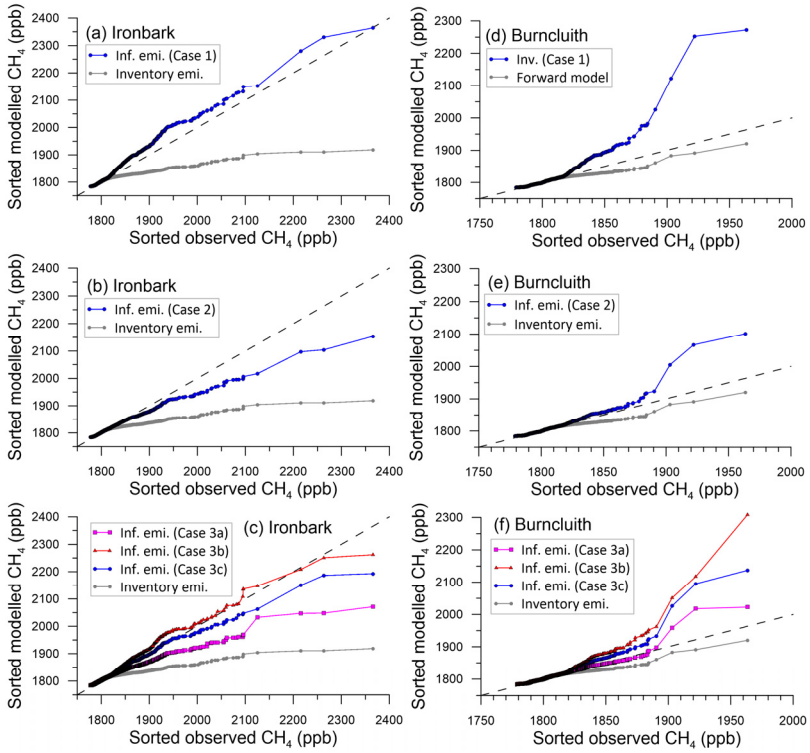

730 **Figure 15. Q-q plots showing the sorted hourly observed versus the sorted modelled CH_4 at the Ironbark and Burncluith monitoring stations. The forward modelled concentrations utilise emission estimates from the ~~(a)~~ Case 1, ~~inversion, (b)~~ Case 2 ~~inversion~~, and ~~(c)~~ Case 3 inversions ~~(i.e. with 1, 3, and 5% uncertainty in the prior relative to the mean)~~. The forward model concentrations ~~from Figure 6~~ ~~obtained~~predicted using the bottom-up emissions are also shown ~~(as~~ grey line~~s~~). The d~~D~~ashed 1:1 line represents perfect agreement.**

735 **7.3 Emissions from the CSG area**

Given the focus on CSG activity related emissions in the Surat Basin, we compare the aggregate bottom-up and inferred emissions from the CSG areas, many of which are concentrated near and between the two monitoring stations. The subdomain that includes all the CSG sources in the study area is shown Figure 16~~Figure 16~~, which is an area of about 18260 km^2, 15% of the study domain, and covers 19 of the 121 source grids considered. The CSG subdomain also contains emissions from other 740 sectors (see Figure 3~~Figure 3~~).

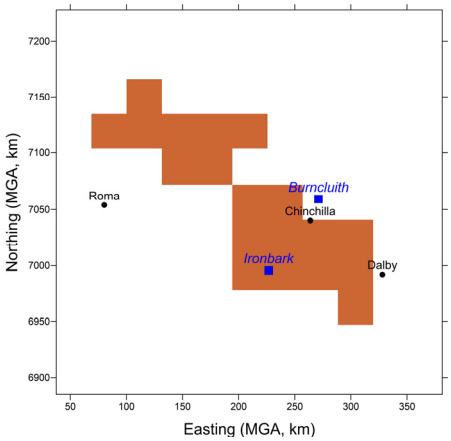

Figure 16. ~~A~~ S~~s~~ubdomain of the study area that covers~~corresponds to~~ all the CSG source areas (shaded grid cells) included in the bottom-up emission inventory. It covers 19 of the 121 source grids (each with a source footprint of 31 × 31 km^2) considered in the inverse modelling.

The total bottom-up inventory emissions from the CSG sub-domain is 47.7 × 10^6 kg yr^{-1} (cf. 173.2 × 10^6 kg yr^{-1} for the study domain) whereas that obtained using the inversion (Case 3c, Figure 13~~Figure 13~~c) is 63.6 × 10^6 kg yr^{-1} (cf. 165.8 × 10^6 kg yr^{-1} for the study domain) which is 33% larger than the former. The total bottom-up emission for this subdomain is dominated by CSG (34.7%, of which 30.6% is due to CSG Processing), followed by grazing cattle (29.9%), feedlots (23.5%) and coal mines (7.7%), which together account for 95.8% of the emissions from this area. Since the inverse methodology does not differentiate between source sectors, emissions from individual sectors cannot be inferred. Considering that the grazing cattle emissions are diffuse sources and thus not likely responsible for peaks in the measurements that dominate the inverse estimates, and since feedlots are scattered throughout the domain (Figure 3~~Figure 3~~c) including the non-CSG areas from where there is no general inference of higher emissions, it is plausible that the increase in the inferred emissions would mainly correspond to CSG as the source sector.

A considerable portion of the CSG emissions is in the area between the two monitoring stations. The inferred emissions in this area are much greater than the corresponding bottom-up inventory emissions. However, t~~T~~his area also has significant coal mining emissions nearby (Figure 3~~Figure 3~~d) and it~~. It~~ is possible that the methane emissions from a combination of these two source sectors are much larger than the inventory emissions.

Conversely, the total bottom-up inventory emissions from the rest of the study domain (i.e. the non-CSG subdomain)~~area~~ is 125.5×10^6 kg yr^{-1}~~.~~, whereas that obtained using the inversion from ~~(~~Case 3c~~)~~ is 102.2×10^6 kg yr^{-1} which is 18.5% lower than the former. The total bottom-up emission for the non-CSG~~is~~ area is dominated by grazing cattle (62.7%), followed by feedlots (24.8%) and coal mines (8.6%), which together account for 96.1% of the emissions from this area. It is possible that the emission factor of 84 kg CH_4 $animal^{-1}$ yr^{-1} for Australian grazing cattle (Harper et al., 1991) used in the bottom-up inventory (see the Supplement S6) is an overestimate (cf. 51 kg CH_4 $animal^{-1}$ yr^{-1} for beef cattle (pasture) used by the Australian National Inventory Report (NIR, 2017) or 63 kg CH_4 $animal^{-1}$ yr^{-1} for non-dairy cattle for the Oceania (IPCC, 2019)), and that would be consistent with ~~the~~a lower top-down methane emission from the non-CSG area compared to the inventory. This also means that the CSG component of the top-down emissions in CSG sub-domain could be higher to compensate for the lower grazing cattle emissions if a lower emission factor for grazing cattle is used.

Apart from the uncertainties associated with the bottom-up emissions, potential methane emissions from some sources, namely wetlands (the amount of which in the area is very limited; https://wetlandinfo.des.qld.gov.au), land clearing, termites, material handling and fuel usage related to mining activities, ground-water wells, and biomass burning are not part of the bottom-up emissions. In contrast, all CH_4 sources are implicitly represented in the inversions, apart from the biomass burning events which have been filtered out using the CO filter. It is difficult to pinpoint which source sectors might be underrepresented in the bottom-up inventory without some kind of source discrimination, for instance, through the use of tracers such as the CH_4 isotopes.

7.4 Temporal variation of the inferred emissions

~~In the previous inverse calculations, all filtered methane measurements obtained during July 2015–December 2016 were combined in a single Bayesian calculation to derive a time invariant top-down emission distribution.~~ Here we apply the inverse model with the Case 3c settings (as used for Figure 13~~Figure 13~~c with 3% prior uncertainty relative to the mean) to 3-monthly measurement blocks within the measurement~~above~~ period (July 2015–December 2016) in order to examine potential temporal variation of the inferred emissions, bearing in mind that~~. Obviously,~~ for a 3-monthly simulation the amount of concentration data supplied to the Bayesian inversion is much less than that for the full simulation. Figure 17~~Figure 17~~a presents the 3-monthly variation of the inferred emissions as kg CH_4 yr^{-1} (bar plots), along with the time invariant~~(constant)~~ bottom-up inventory emissions (red line) and ~~the (constant)~~ inferred emissions from Case 3c (blue line). The 3-monthly emission rates are within 165–180 kg yr^{-1} and are generally larger than the time invariant inferred emissions obtained using the ~~when the full~~ measurements from the full period~~duration is considered~~. We believe that t~~T~~his is at least partly because as the amount of information supplied to the inversion~~e model~~ reduces, the inferred emissions are not modulated to the same extent as that for the full period, and thus they tend to move closer to the bottom-up inventory which is used as a prior ~~with a tight uncertainty~~. ~~(Time-varying inventory emissions, if available, would act as a better prior, together with additional measurement sites).~~

Another related reason could be the narrowing of the amount of source area represented by the source-receptor relationship because of seasonal winds falling in relatively narrow directional sectors compared to the broader wind rose for the full period.

Figure 17~~Figure 17~~b is the same as Figure 17~~Figure 17~~a but for the CSG subdomain. The 3-monthly inferred emissions lie between the bottom-up inventory value and the time invariant inferred value ~~obtained when the measurements from the full period are used~~. Again, as in Figure 17~~Figure 17~~a, 3-monthly inferred emissions push towards the inventory value ~~as the information supplied to the inverse model reduces~~.

Figure 17~~Figure 17~~c is the same as Figure 17~~Figure 17~~a but for the non-CSG subdomain (which is dominated by grazing cattle emissions (62.7%) as per the bottom-up inventory). In this plot, we also present a 3-monthly climatological average (1992 – current 2020) of rainfall at the Dalby airport (location 27.16°S, 151.26°E), located next to the town of Dalby, within the study domain. The rainfall data were obtained from the Australian Bureau of Meteorology (from http://www.bom.gov.au/climate/averages/tables/cw_041522.shtml). There is a good correlation (r = 0.79) between the 3-monthly inferred non-CSG methane emission and the rainfall, suggesting that the inferred emission variation could, to some extent, be attributed to the seasonality of rainfall which would influence areas such as pasture growth ~~and wetlands~~ and thus methane emissions from grazing~~, influenced by rainfall~~. This correlation for the 3-monthly inferred emissions for~~from~~ the full domain (Figure 17~~Figure 17~~a) is 0.71 and it is -0.06 for those from the CSG subdomain (Figure 17~~Figure 17~~b). It is reasonable to assume that~~Assuming that~~ the higher the rainfall the higher the grazing cattle ~~(and wetland)~~ emissions, and in that case these r values indicate that the seasonal variability in~~of~~ the inferred emissions within the full domain is, to a lesser degree, also influenced by such emissions~~grazing cattle~~. However,~~, but~~ the inferred emission seasonality within~~for~~ the CSG area does not correlate with rainfall,~~cannot be linked with grazing cattle seasonality~~ meaning that the emission seasonality is possibly dominated by the CSG sources.

Another potential contributor to the temporal variability in the inferred emissions in Figure 17~~Figure 17~~ is the seasonality of the winds ~~in the area~~ which influences the source-receptor relationships. ~~We have not explored this possibility here.~~

The uncertainties in the inferred seasonal emissions Figure 17~~Figure 17~~ is around 5% of the mean – a relatively small value largely the result of a tight prior.

To test how well the temporal variation of the inferred emissions represents reality, we conducted a forward TAPM run using these emissions , and the resulting q-q plots (red dots) are shown in Figure 18~~Figure 18~~. The methane data at Burncluith are best described by these 3-monthly varying emissions compared to any other emission setup, but at Ironbark, these emissions underestimate the ~~methane~~ data (the inversion setup corresponding to Figure 15~~Figure 15~~c best describes the Ironbark data). ~~Additional measured parameters (e.g. tracers), as well as more monitoring stations and other additional data (e.g. about the prior), would be useful in further constraining the emissions.~~

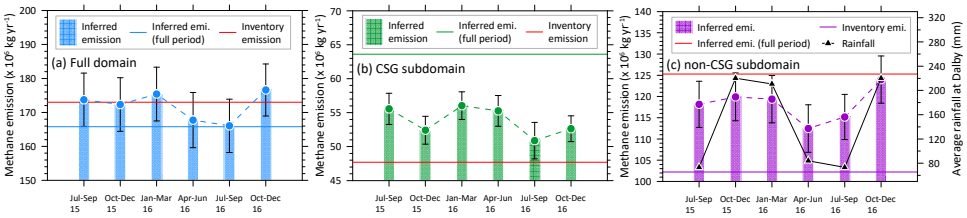

Figure 17. 3-monthly variation of the inferred emissions (bar plots), including one standard deviation uncertainty (~ 5% of the mean), for (a) the full study domain, (b) the CSG subdomain, and (c) the non- CSG subdomain. The respective time-invariant~~constant~~ bottom-up inventory emissions (red line) and the time invariant ~~the constant inverse~~/inferred emissions from the Case 3c inversion (Figure 13~~Figure 13~~c) are also shown. Note the emission units. In (c), a 3-montthly climatological average (1992 – current 2020) of rainfall at the Dalby airport located within the study domain is also shown.

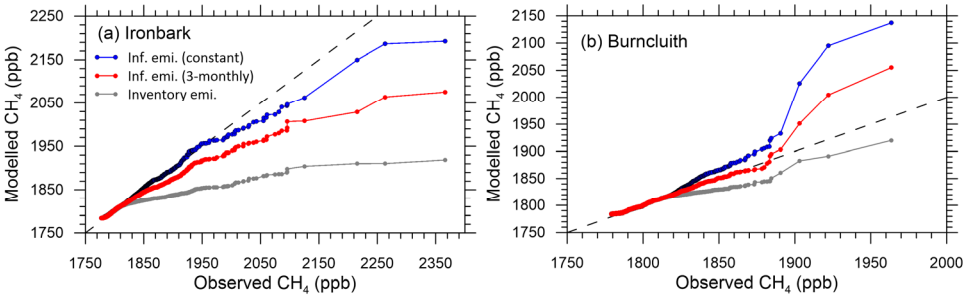

Figure 18. Q-q plots showing the sorted hourly observed versus the sorted modelled CH_4 at the two monitoring stations. The modelled concentrations~~values (blue dots)~~ are predicted using: the time-invariant inferred emissions from the Case 3c inversion (with 3% uncertainty in the prior relative to the mean) (blue dots); ~~the red dots are the~~produced from 3-monthly inferred emissions~~inversions~~ (red dots); and the~~ bottom-up inventory emissions (grey dots).~~forward model concentrations from Figure 6 predicted using the bottom-up emissions are shown as grey lines.~~ The d~~D~~ashed 1:1 line represents perfect agreement.

Given the rapid rise in the CSG production in the Surat Basin, one may deduce that the 2016 CSG methane emissions were larger than the 2015 bottom-up emissions and, therefore, could potentially explain the top-down emissions in the CSG area being higher than the inventory emissions. Figure 19~~Figure 19~~ shows that compared to July–December 2015, the total CSG produced was higher by 32% during January–June 2016 and by 45% during July–December 2016, which correlates with an increase in the number of CSG production wells in the area. However, Figure 19~~Figure 19~~ also shows that there is a downward trend in the amount of flared/vented gas. Considering, based on the bottom-up inventory in Section 3, that venting (from processing) is the biggest contributor (88%) followed by flaring (8%) (from both processing and production) to the total CSG methane emissions, it is plausible that despite the increase in the CSG development in the area the CSG-related methane

emissions have not increased, and that they may have even gone down. The temporal variation of the inferred emissions in Figure 17~~Figure 17~~b for the CSG dominated area also does not indicate any consistent increase in emissions from 2015 to 2016. Thus, the 33% higher top-down emission estimate from the CSG area compared to the inventory estimate cannot be explained in terms of the growth in the CSG production from 2015 to 2016 and is possibly related to underestimated or missing emissions in the inventory. This also implies that the emissions from CSG may be more closely related to practices in the industry than to the amount of CSG produced.

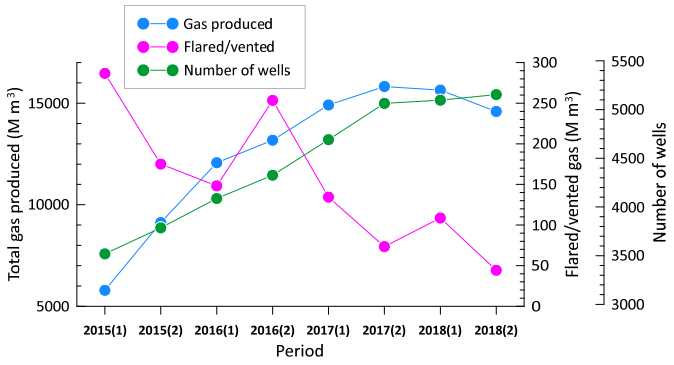

Figure 19. Six-monthly trends of the total CSG produced, amount of flared/vented gas, and number of wells in the Surat Basin (data from https://www.data.qld.gov.au/dataset/petroleum-gas-production-and-reserve-statistics[1]).

7.5 Sensitivity of inversion to background methane

Figure 4~~Figure 4~~ shows that there is a slight difference in the estimated background CH_4 levels between the two monitoring locations, with the Ironbark background methane larger by 1 ppb on average than Burncluith and the standard deviation of the background differences being 1.4 ppb, the latter is comparable to the background concentration uncertainty (= 3.5 ppb) considered in the inversion.

[1] This data file places the gas fields of Spring Gully and Peat within the Bowen Basin whereas in our bottom-inventory these are part of the Surat Basin. This is because of how the gas field zones and basin boundaries are defined. The gas fields included in our study are based on their geographic locations relative to the square study domain selected. Adding these two gas fields to the Surat Basin does not change the trends shown in Figure 19~~Figure 19~~.

We conducted an inversion~~inverse modelling~~ sensitivity test with the same model setup as that for Figure 13~~Figure 13~~c (Case 3c~~, with the bottom-up inventory as a Gaussian prior with σ_p = 3% q_p~~), except that instead of using the background times series that was averaged over the two sites we used the respective background time series for the two~~se~~ sites. The results were virtually the same compared to Figure 13~~Figure 13~~c, other than some insignificant changes in areas with low emissions. Table 2~~Table 2~~ gives the annual inferred emissions, which show no sensitivity.

Our background methane~~concentration~~ calculation methodology (Supplement S3) assumes that under very vigorous atmospheric mixing conditions in the daytime, the measured concentrations within study domain represent methane levels both within and outside the domain boundaries, so that the measured concentrations can be taken to represent the background under such conditions. Because the background concentration is calculated from the measurements within the source region under study, there is a possibility that the real background is potentially lower than what we have used. To examine this, another inversion sensitivity test was conducted by using an alternate methane background times series (with all other settings the same as the final Case 3c inversion) and this is described in detail in the Supplement S5. Essentially, t~~T~~he alternate background was constructed using the original averaged background from the two sites and the marine baseline methane measurements from the Cape Grim Baseline Air Pollution Station (https://capegrim.csiro.au), located on the north-west tip of Tasmania (40.7ºS, 144.7ºE). The marine baseline methane represents concentration levels without the direct influence of the continental sources. The alternate background falls between the average Surat background as used in the paper and the Cape Grim baseline and is, on average, lower than the original Surat background by 2.8 ppb. (On average, the Cape Grim marine baseline was 8.4 ppb lower than the original Surat background used).

The inversion results in Table 2~~Table 2~~ show that compared to the inferred emissions obtained using the original background methane the alternate background gives total emissions that are 6.8% higher, while the increase is smaller at 3.9% in the CSG subdomain and larger at 8.5% in the non-CSG region. The overall increase is expected because the increase in the measured concentrations by 2.8 ppb as a result of the use of the alternate background needs to be accounted for by the inversion by enhancing the amount of inferred emissions. We also find that the amount of increase in the inferred emissions with the alternate background is almost uniformly spread through the study domain relative to the total emission, and that there are no significant spatial distributional shifts in the inferred emissions with the two background choices. ~~This means that if these emissions are used in a forward model simulation, they would lift the modelled concentrations throughout the region by a very similar amount (probably by 2.8 ppb).~~

There are possibly other and better ways of calculating the background methane concentration, such as having methane measurements at many locations around the perimeter of the study domain (which is often subject to operational and budget constraints) or modelling methane at much larger scale, preferably global, with data assimilation, which could then provide concentration boundary conditions needed for the regional modelling.

Formatted: Font: 10 pt, Not Bold

Formatted: Font: 10 pt, Not Bold

Table 2: Inferred emissions ($\times 10^6$ kg yr^{-1}) obtained using: the methane background averaged over the two sites (as used in the paper, Case 3c), the individual methane background from the two sites, and the alternate methane background calculated using the Cape Grim baseline methane data (see Supplement S5). The values in the parentheses are % change over the inferred emissions using the averaged background. The bottom-up inventory emissions are also included for comparison.

SelectedMethane background	Total	CSG subdomain	Non-CSG subdomain
Average background (as used in this paper)	165.8	63.6	102.2
Separate backgrounds from the two sites	164.8 (-0.6%)	62.7 (-1.4%)	102.1 (-0.1%)
Alternate background (see Supplement S5)	177.0 (+6.8%)	66.1 (+3.9%)	110.9 (+8.5%)
Bottom-up inventory emissions	173.2 (+4.5%)	47.7 (-25%)	125.5 (+22.8)

8 Conclusions

This paper presented quantification of methane emissions from the CSG producing Surat Basin, an area of 350 × 350 km^2 in Queensland, Australia. The 2015 bottom-up methane emission inventory served as a very useful prior in our regional inversetop-down methodology based on a Bayesian inference approach that utilised hourly-mean CH_4 concentrations monitored at the Ironbark and Burncluith stations for 1.5 years, hourly source-receptor relationship, and an MCMC technique for posterior PDF sampling.

The largest contribution to the emissions in the bottom-up methane inventory wasis from grazing cattle (~50%), cattle feedlots (~25%), and CSG processing (~8%), with the aggregate emissions in the study area being approximately 173.2 × 10^6 kg CH_4 yr^{-1}. Although the forward transport modelling with the bottom-up emissions yielded a credible simulation of the suitably filtered observed methane concentrations, about 15% of the higher-end concentration observations were underestimated.

The top-down Bayesian inverse approach demonstrated that even when we do not specify an informative prior, the source signal inherent in the methane observations from only two sites constrains the total emission well. But, in contrast to the inventory emissions, the inferred emissions are more intensely located in the centre of the study region and less in regions that are farther. The importance of specifying a suitable prior in the Bayesian inference was made apparent by the synthetic inversion, demonstrating with the use of the bottom-up inventory with a narrow uncertainty as being a good choiceproving very valuable for that purpose when only two monitoring locations available. For inversion with the real methane measurementsParticularly, a Gaussian prior having mean values taken the same as the bottom-up emissions with an uncertainty

equal to 3% of the mean yielded the best emission distribution, as evident from its performance in faithfully reproducing the measured methane concentration time series. This inverse setup yielded a domain-wide emission of 165.8 × 10^6 kg CH_4 yr^{-1} which is very slightly less than the one obtained from the bottom-up inventory. However, within a subdomain covering all the CSG source areas, the inferred emission 63.6 × 10^6 kg CH_4 $yr^{-1}$is 33% larger than that deduced from the bottom-up inventory. The dominant localised inventory emissions in this area are from CSG, followed by feedlots. Since feedlots are scattered throughout the domain including the non-CSG areas from where there is no indication~~inference~~ of higher emissions, it is plausible that the increase in the inferred emissions would mainly correspond to CSG as the source sector.

Despite the amount of concentration data going into the seasonal inversion being relatively limited, the ~~We also~~ inferred seasonal variation of methane emissions from~~within~~ the non-CSG~~full study domain, and CSG and non-CSG~~ subdomain correlated well with climatological seasonal rainfall in the areas~~,~~ suggesting a possible link with the seasonality of agricultural emissions. This correlation was almost zero for the CSG subdomain, possibly due to the CSG sources dominating the seasonality.

There was some sensitivity to the background methane concentration observed in the inversion, and we believe that further approaches to the background calculation are necessary for regions like the Surat Basin.

The source-receptor relationship showed that having only two monitoring stations is inadequate for sampling distant source areas within the large study domain, especially areas in the south-east and north-west corners (the network design for the two monitoring stations mainly focused on the central CSG regions). Lengthening the measurement period to sample these areas better would not have helped because the wind climatology of the area is not likely to change considerably. When source areas are not sampled well, one may impose stricter priors that are more credible than the inferred emissions, or alternatively increase the number of stations. The former strategy is probably reflected in our use of a small uncertainty in the prior (i.e. 3% of the mean) for the best inversion case. A smaller prior uncertainty pushes the inversion more towards the prior itself with distant source areas not sampled sufficiently by the network sites looking like the prior distribution. ~~A larger prior uncertainty results in the inversion moving towards higher emissions for sources that are close to the monitoring stations.~~

The inverse methodology could not distinguish between different source categories, mainly because the concentration of methane alone was monitored and not tracers specific to methane source types. To do source discrimination and attribution, monitoring of tracer species such as methane isotopes ($^{13}CH_4$, CH_3D and $^{14}CH_4$), or other hydrocarbons in cases where they are associated with the source gas, would prove useful when suitable sampling systems or instrumentation for field deployment become available.

The methods developed in this study could be used to improve the monitoring and management of greenhouse gas and other air emissions from the onshore gas industry, including that in the Surat Basin. They provide independent information to industry and communities living in gas development regions on one of the main environmental impacts potentially arising from onshore gas developments. Improved quantification of methane emissions on the regional scale is an important step in

emissions reductions from the onshore gas sector and possibly other industries. The present top-down method is particularly suited to distributed emissions with potentially unknown locations across a large geological gas reservoir and gas production infrastructure. If monitoring is deployed before gas exploration and production begins then a baseline would be established from which emissions from the industry might be detected. Ongoing top-down quantification, with monitoring stations located close to where emissions appear and with source-specific information from tracers could provide the information necessary to validate emissions from the gas industry to support greenhouse gas inventories.

Data availability

The data and model output included in this paper can be made available by contacting the corresponding author (Ashok Luhar: ashok.luhar@csiro.au).

Author contributions

AKL performed the model development and application, analysed model output and data, and wrote the paper with contributions and comments from the co-authors. DME conducted the field study design, in-situ monitoring and data analysis, and GISERA project management. ZML conducted the in-situ monitoring, data collection, and data analysis. JN contributed to data processing. DS assisted with the monitoring sites, instrumentation and data collection. LS developed the bottom-up inventory. CO provided general information on methane sources.

Competing interests

The authors declare that they have no conflict of interest.

Acknowledgments

This work was partially supported by CSIRO's Gas Industry Social and Environmental Research Alliance (GISERA) (https://gisera.csiro.au) and Active Integrated Matter (AIM) Future Science Platform (FSP) (https://research.csiro.au/aim). Mark Kitchen and Steve Zegelin provided valuable instrumental and technical support. Staff of GASLAB at CSIRO Oceans and Atmosphere, Aspendale, provided the atmospheric composition measurement support and calibration standards required for this work. The landowners of the Burncluith and Ironbark sites provided essential support of the monitoring. The authors thank Peter Rayner, Martin Cope and Dimitri Lafleur for their helpful comments on this work, and Natalie Shaw for her assistance with the preparation of the bottom-up inventory for the Surat Basin. Damian Barrett advised on this work, and Stuart Day furnished insights into local source monitoring. Useful comments by the two anonymous referees and Bryce Kelly are

much appreciated. NCEP Reanalysis data provided by the NOAA/OAR/ESRL PSL, Boulder, Colorado, USA, from their Web site at https://psl.noaa.gov.

References

Alvarez, R. A., Zavala-Araiza, D., Lyon, D. R., Allen, D. T., Barkley, Z. R., Brandt, A. R., et al.: Assessment of methane emissions from the U.S. oil and gas supply chain, Science, 361(6398), 186–188, https://doi.org/10.1126/science.aar7204, 2018.

Brandt, A. R., Heath, G. A., Kort, E. A., O'Sullivan, F., Pétron, G., Jordaan, S.M., et al.: Methane leaks from North American natural gas systems, Science, 343(6172), 733–735, https://doi.org/10.1126/science.1247045, 2014.

Cheng, M.-D., Hopke, P. K., and Zeng, Y.: A receptor-oriented methodology for determining source regions of particulate sulfate at Dorset, Ontario, Journal of Geophysical Research, 98(D9), 16,839–16,849, https://doi.org/10.1029/92JD02622, 1993.

Cui, Y. Y., Brioude, J., Angevine, W.M., Peischl, J., McKeen, S. A., Kim, S.-W., et al.: Top-down estimate of methane emissions in California using a mesoscale inverse modeling technique: The San Joaquin Valley, Journal of Geophysical Research, 122(6), 3686–3699, https://doi.org/10.1002/2016JD026398, 2017.

Day, S., Dell'Amico, M., Etheridge, D., Ong, C., Rodger, A., Sherman, B., and Barrett, D.: Characterisation of regional fluxes of methane in the Surat Basin, Queensland. Phase 1: A review and analysis of literature on methane detection and flux determination. CSIRO Australia report, 2013.

Day, S., Ong, C., Rodger, A., Etheridge, D., Hibberd, M., van Gorsel, E., et al.: Characterisation of regional fluxes of methane in the Surat Basin, Queensland: Phase 2: A pilot study of methodology to detect and quantify methane sources, CSIRO Australia report EP15369, 2015.

DNRM: Queensland's Petroleum and Coal Seam Gas 2015–16, Department of Natural Resources and Mines, Queensland Government, Australia, 8 pp., http://www.australiaminerals.gov.au/__data/assets/pdf_file/0003/47622/Queenslands-petroleum-and-coal-seam-gas-2017.pdf, 2017.

Etheridge, D., Loh, Z., Schroder, I., Berko, H., Kuske, T., Allison, C., et al.: Metadata report: Arcturus atmospheric greenhouse gas monitoring. Record 2014/37, Geoscience Australia, Canberra, 2014.

Etheridge, D. M., Day, S., Hibberd, M. F., Luhar, A., Spencer, D. A., Loh, Z. M., et al.: Characterisation of regional fluxes of methane in the Surat Basin, Queensland: The continuous monitoring results – installation, commissioning and operation of two field stations and preliminary data, Milestone 3.1 GISERA Greenhouse Gas Research – Phase 3, CSIRO Australia report, 2016.

Etiope, G, Ciotoli, G, Schwietzke, S and Schoell, M.: Gridded maps of geological methane emissions and their isotopic signature, Earth Syst Sci Data, 11, 1–22, doi: 10.5194/essd-11-1-2019, 2019.

Etiope, G. and Schwietzke, S.: Global geological methane emissions: an update of top-down and bottom-up estimates, Elem Sci Anth, 7(1), p. 47, http://doi.org/10.1525/elementa.383, 2019.

Feitz, A., Schroder, I., Phillips, F., Coates, T., Neghandhi, K., Day, S., et al.: The Ginninderra CH_4 and CO_2 release experiment: An evaluation of gas detection and quantification techniques, International Journal of Greenhouse Gas Control, 70, 202–224, https://doi.org/10.1016/j.ijggc.2017.11.018, 2018.

Harper, L. A, Denmead, O. T., Freney, J. R, and Byers, F. M.: Direct measurements of methane emissions from grazing and feedlot cattle, Journal of Animal Science, 77, 1392–1401, https://doi.org/10.2527/1999.7761392x, 1999.

Henne, S., Brunner, D., Oney, B., Leuenberger, M., Eugster, W., Bamberger, I., et al.: Validation of the Swiss methane emission inventory by atmospheric observations and inverse modelling, Atmospheric Chemistry and Physics, 16(6), 3683–3710, https://doi.org/10.5194/acp-16-3683-2016, 2016.

Hmiel, B., Petrenko, V. V., Dyonisius, M. N. et al.: Preindustrial $^{14}CH_4$ indicates greater anthropogenic fossil CH_4 emissions, Nature 578, 409–412, https://doi.org/10.1038/s41586-020-1991-8, 2020.

Hourdin, F. and Talagrand, O.: Eulerian backtracking of atmospheric tracers. I: Adjoint derivation and parametrization of subgrid-scale transport, Quarterly Journal of the Royal Meteorological Society, 132(615), 567–583, https://doi.org/10.1256/qj.03.198.A, 2006.

Hurley, P.: TAPM V4. Part 1: Technical Description. CSIRO Marine and Atmospheric Research Paper No. 25, Australia, p. 59. Available at: http://www.cmar.csiro.au/research/tapm/docs/tapm_v4_technical_paper_part1.pdf, 2008.

Hurley, P. J. and Luhar, A. K.: Modelling the meteorology at the Cabauw tower for 2005, Boundary-Layer Meteorology, 132(1), 43–57, https://doi.org/10.1007/s10546-009-9384-4, 2009.

Hurley, P. J., Physick, W. L., and Luhar, A. K.: TAPM: a practical approach to prognostic meteorological and air pollution modelling, Environmental Modelling and Software, 20(6), 737–752, https://doi.org/10.1016/j.envsoft.2004.04.006, 2005.

IPCC: Climate Change 2014: Synthesis Report. Contribution of Working Groups I, II and III to the Fifth Assessment Report of the Intergovernmental Panel on Climate Change [Core Writing Team, R.K. Pachauri and L.A. Meyer (eds.)]. IPCC, Geneva, Switzerland, 151 pp. http://www.ipcc.ch/pdf/assessment-report/ar5/syr/SYR_AR5_FINAL_full.pdf, 2014.

IPCC: 2019 Refinement to the 2006 IPCC Guidelines for National Greenhouse Gas Inventories (Calvo Buendia, E., Tanabe, K., Kranjc, A., Baasansuren, J., Fukuda, M., Ngarize, S., Osako, A., Pyrozhenko, Y., Shermanau, P. and Federici, S. (eds.)), Volume 4: Agriculture, Forestry and Other Land Use: Chapter 10: Emissions from Livestock and Manure Management, Published: IPCC, Switzerland, 2019.

Iverach, C. P., Cendon, D. I., Hankin, S. I., Lowry, D., Fisher, R. E., France, J. L., Nisbet, E.G, Baker, A., and Kelly, B. F. J.: Assessing connectivity between an overlying aquifer and a coal seam gas resource using methane isotopes, dissolved organic carbon and tritium, Scientific Reports, 5, 15996, https://doi.org/10.1038/srep15996, 2015.

Jaynes, E. T.: Probability theory: The logic of science, Cambridge University Press, Cambridge, UK, 753 pp., 2003.

Jeong, S., Zhao, C. Andrews, A. E., Bianco, L., Wilczak, J. M., and Fischer, M. L.: Seasonal variation of CH_4 emissions from central California, Journal of Geophysical Research, 117, D11306, https://doi.org/10.1029/2011JD016896, 2012.

Kalnay, E., Kanamitsu, M., Kistler, R., Collins, W., Deaven, D., et al.: The NCEP/NCAR 40-year reanalysis project, Bull. Amer. Meteor. Soc., 77, 437–472, https://doi.org/10.1175/1520-0477(1996)077<0437:TNYRP>2.0.CO;2, 1996.

Katestone: Surat Basin Methane Inventory 2015 – Summary Report. Prepared by Katestone Environmental Pty Ltd, Brisbane, Queensland, for CSIRO, document no. D15193-18, 2018.

Luhar, A. K. and Hurley, P.: Evaluation of TAPM, a prognostic meteorological and air pollution model, using urban and rural point source data, Atmospheric Environment, 37(20), 2795–2810, https://doi.org/10.1016/S1352-2310(03)00204-8, 2003.

Luhar, A. K., Mitchell, R. M., Meyer, C. P., Qin, Y., Campbell, S., Gras, J. L., and Parry, D.: Biomass burning emissions over northern Australia constrained by aerosol measurements: II–Model validation, and impacts on air quality and radiative forcing, Atmospheric Environment, 42(7), 1647–1664, https://doi.org/10.1016/j.atmosenv.2007.12.040, 2008.

Luhar, A. K., and Hurley, P. J.: Application of a coupled prognostic model to turbulence and dispersion in light-wind stable conditions, with an analytical correction to vertically resolve concentrations near the surface, Atmospheric Environment, 51, 56–66, https://doi.org/10.1016/j.atmosenv.2012.01.046, 2012.

Luhar, A. K., Etheridge, D. M., Leuning, R., Loh, Z. M., Jenkins, C. R., and Yee, E.: Locating and quantifying greenhouse gas emissions at a geological CO_2 storage site using atmospheric modeling and measurements, Journal of Geophysical Research: Atmospheres, 119(18), 10959–10979, https://doi.org/10.1002/2014JD021880, 2014.

Luhar, A. K., Thatcher, M., and Hurley, P. J.: Evaluating a building-averaged urban surface scheme in an operational mesoscale model for flow and dispersion, Atmos. Environ., 88, 47–58, http://dx.doi.org/10.1016/j.atmosenv.2014.01.059, 2014.

Luhar, A. K., Emmerson, K. M., Reisen, F., Williamson, G. J., and Cope, M. E.: Modelling smoke distribution in the vicinity of a large and prolonged fire from an open-cut coal mine. Atmos Environ., 229, 117471, https://doi.org/10.1016/j.atmosenv.2020.117471, 2020.

Marchuk, G. I.: Adjoint equations and analysis of complex systems. Dordrecht, Netherlands: Springer Science. pp. 466, 1995.

Matthaios, V. N., Triantafyllou, A. G., and Koutrakis, P.: PM_{10} episodes in Greece: Local sources versus long-range transport—observations and model simulations. Journal of the Air and Waste Management Association, 67(1), 105–126, https://doi.org/10.1080/10962247.2016.1231146, 2017.

Meinshausen, M., Vogel, E., Nauels, A., Lorbacher, K., Meinshausen, N., Etheridge, D. M., Fraser, P. J., Montzka, S. A., Rayner, P. J., Trudinger, C. M., Krummel, P. B., Beyerle, U., Canadell, J. G., Daniel, J. S., Enting, I. G., Law, R. M., Lunder, C. R., O'Doherty, S., Prinn, R. G., Reimann, S., Rubino, M., Velders, G. J. M., Vollmer, M. K., Wang, R. H. J., and Weiss, R.: Historical greenhouse gas concentrations for climate modelling (CMIP6), Geosci. Model Dev., 10, 2057–2116, https://doi.org/10.5194/gmd-10-2057-2017, 2017.

Miller, S. M., Michalak, A. M., and Levi, P. J.: Atmospheric inverse modeling with known physical bounds: an example from trace gas emissions, Geoscientific Model Development, 7(1), 303–315, https://doi.org/10.5194/gmd-7-303-2014, 2014.

NIR: National Inventory Report 2015 Volume 1, Commonwealth of Australia, https://www.industry.gov.au/sites/default/files/2020-07/national-inventory-report-2015-volume-1.pdf, 2017.

Pudykiewicz, J. A.: Application of adjoint tracer transport equations for evaluating source parameters, Atmospheric Environment, 32(17), 3039–3050, https://doi.org/10.1016/S1352-2310(97)00480-9, 1998.

Rao, K. S.: Source estimation methods for atmospheric dispersion, Atmospheric Environment, 41(33), 6964–6973, https://doi.org/10.1016/j.atmosenv.2007.04.064, 2007.

Rubino, M., Etheridge, D. M., Thornton, D. P., Howden, R., Allison, C. E., Francey, R. J., Langenfelds, R. L., Steele, L. P., Trudinger, C. M., Spencer, D. A., Curran, M. A. J., van Ommen, T. D., and Smith, A. M.: Revised records of atmospheric trace gases CO_2, CH_4, N_2O, and $\delta^{13}C$-CO_2 over the last 2000 years from Law Dome, Antarctica, Earth Syst. Sci. Data, 11, 473–492, https://doi.org/10.5194/essd-11-473-2019, 2019.

Saunois, M., Stavert, A. R., Poulter, B., Bousquet, P., Canadell, J. G., Jackson, R. B., et al.: The global methane budget 2000–2017, Earth System Science Data, 12, 1561–1623, https://doi.org/10.5194/essd-12-1561-2020, 2020.

Schneising, O., Burrows, J. P., Dickerson, R. R., Buchwitz, M., Reuter, M., and Bovensmann, H.: Remote sensing of fugitive methane emissions from oil and gas production in North American tight geologic formations, Earth's Future, *2*, 548–558, https://doi.org/10.1002/2014EF000265, 2014.

Singh, S. K., Sharan, M., and Issartel, J.-P.: Inverse modelling methods for identifying unknown releases in emergency scenarios: an overview, Int. J. Environment and Pollution, 57(1/2), 68–91, https://doi.org/10.1504/IJEP.2015.072121, 2015.

Tarantola, A.: Inverse problem theory and methods for model parameter estimation. Society for Industrial and Applied Mathematics, Philadelphia, 342 p., 2005.

Towler, B., Firouzi, M., Underschultz, J., Rifkin, W., Garnett, A., Schultz, H., et al.: An overview of the coal seam gas developments in Queensland, Journal of Natural Gas Science and Engineering, 31, 249–271, https://doi.org/10.1016/j.jngse.2016.02.040, 2016.

Venkatram, A., Brode, R., Cimorelli, A., Lee, R., Paine, R., Perry, S., et al.: A complex terrain dispersion model for regulatory applications, Atmospheric Environment, 35, 4211–4221, https://doi.org/10.1016/S1352-2310(01)00186-8, 2001.

Wang, Y. P., and S. T. Bentley, S. T.: Development of a spatially explicit inventory of methane emissions from Australia and its verification using atmospheric concentration data, Atmospheric Environment, 36, 4965–4975, https://doi.org/10.1016/S1352-2310(02)00589-7, 2002.

WMO: WMO Greenhouse Gas Bulletin, No. 14, 22 November 2018, https://library.wmo.int/doc_num.php?explnum_id=5455, ISSN 2078-0796, 2018.

Yee, E., Lien, F.-S., Keats, A., and D'Amours, R.: Bayesian inversion of concentration data: Source reconstruction in the adjoint representation of atmospheric diffusion, Journal of Wind Engineering and Industrial Aerodynamics, 96(10-11), 1805–1816, https://doi.org/10.1016/j.jweia.2008.02.024, 2008.

Yee, E. and Flesch, T. K.: Inference of emission rates from multiple sources using Bayesian probability theory, Journal of Environmental Monitoring, 12, 622–634, https://doi.org/10.1039/B916954G, 2010.

Yee, E.: Inverse dispersion for an unknown number of sources: Model selection and uncertainty analysis, ISRN Applied Mathematics, Article ID 465320, 20 pp., 2012.